OBSERVATION AND INTERPRETATION OF TECTONIC STRAIN RELEASE MECHANISMS

Thesis by

Max Wyss

In Partial Fulfillment of the Requirements

For the Degree of

Doctor of Philosophy

California Institute of Technology

Pasadena, California

1970

(Submitted March 31, 1970)

ACKNOWLEDGMENTS

The work presented in this thesis would not have been possible without the continuous and generous support given to me by the entire staff of the Seismological Laboratory. In particular, I wish to thank Dr. J. N. Brune whose continuous interest, criticism, and suggestions played a most important role in the development of this work. Some of Dr. Brune's thoughts and his help were crucial in the work presented in chapters II, III, and IV. I wish to thank Dr. S. W. Smith who had continuous interest in my work and whose suggestions and guidance led to the results presented in chapter I. I also wish to thank Dr. C. R. Allen whose extremely valuable guidance in all questions regarding tectonic processes is strongly reflected in the presentation of chapter I and III. The cooperation with Dr. C. H. Scholz on some of this work provided a great stimulus. Beneficial discussions with Dr. C. B. Archambeau and Dr. D. P. McKenzie are gratefully acknowledged.

I also wish to thank Mrs. Barbara Sloan who typed the manuscript and Mr. Laszlo Lenches who drafted the figures.

This study was supported by the following grants: National Science Foundation Grant GA 1087, National Science Foundation Grant GP 2806, National Science Foundation Grant GA 12868, National Science Foundation Grant GA 11332, and by the Advanced Research Projects Agency of the Department of Defense and was monitored for the Air Force Office of Scientific Research under contract F44620-69-C-0067.

Abstract

In four chapters various aspects of earthquake source are studied.

Chapter I

Surface displacements that followed the Parkfield, 1966, earthquakes were measured for two years with six small-scale geodetic networks straddling the fault trace. The logarithmic rate and the periodic nature of the creep displacement recorded on a strain meter made it possible to predict creep episodes on the San Andreas fault. Some individual earthquakes were related directly to surface displacement, while in general, slow creep and aftershock activity were found to occur independently. The Parkfield earthquake is interpreted as a buried dislocation.

Chapter II

The source parameters of earthquakes between magnitude 1 and 6 were studied using field observations, fault plane solutions, and surface wave and S-wave spectral analysis. The seismic moment, M_o, was found to be related to local magnitude, M_L, by $\log M_o = 1.7 M_L + 15.1$. The source length vs magnitude relation for the San Andreas system was found to be: $M_L = 1.9 \log L - 6.7$. The surface wave envelope parameter AR gives the moment according

to log M_o = log AR_{300} + 30.1, and the stress drop, τ, was found to be related to the magnitude by τ = 0.54 M - 2.58. The relation between surface wave magnitude M_S and M_L is proposed to be M_S = 1.7 M_L - 4.1. It is proposed to estimate the relative stress level (and possibly the strength) of a source-region by the amplitude ratio of high-frequency to low-frequency waves. An apparent stress map for Southern California is presented.

Chapter III

Seismic triggering and seismic shaking are proposed as two closely related mechanisms of strain release which explain observations of the character of the P wave generated by the Alaskan earthquake of 1964, and distant fault slippage observed after the Borrego Mountain, California earthquake of 1968. The Alaska, 1964, earthquake is shown to be adequately described as a series of individual rupture events. The first of these events had a body wave magnitude of 6.6 and is considered to have initiated or triggered the whole sequence. The propagation velocity of the disturbance is estimated to be 3.5 km/sec. On the basis of circumstantial evidence it is proposed that the Borrego Mountain, 1968, earthquake caused release of tectonic strain along three active faults at distances of 45 to 75 km from the epicenter. It is suggested that this mechanism of strain release is best

described as "seismic shaking."

Chapter IV

The changes of apparent stress with depth are studied in the South American deep seismic zone. For shallow earthquakes the apparent stress is 20 bars on the average, the same as for earthquakes in the Aleutians and on Oceanic Ridges. At depths between 50 and 150 km the apparent stresses are relatively high, approximately 380 bars, and around 600 km depth they are again near 20 bars. The seismic efficiency is estimated to be 0.1. This suggests that the true stress is obtained by multiplying the apparent stress by ten. The variation of apparent stress with depth is explained in terms of the hypothesis of ocean floor consumption.

TABLE OF CONTENTS

Page

Page

Chapter III

Seismic Triggering and Seismic Shaking As
Mechanisms for Tectonic Strain Release

Page

Chapter IV

Seismic Moment, Stress, and Source Dimensions
as a Function of Depth in a Deep Seismic Zone, and
Comparison with Earthquakes on Oceanic Rises

Page

Prologue

This thesis is written in four chapters. Each chapter is a study of different types and aspects of tectonic strain release. The results of each chapter are used in one or several of the other chapters. Observations of tectonic displacements along faults in the field are combined with the analysis of seismic records in order to derive earthquake source parameters. These parameters include seismic energy, seismic moment, fault dimensions, average displacement, stress drop, apparent shear stress, and seismic efficiency.

Reid (1910) put forward the hypothesis that shallow earthquakes are caused by elastic rebound when displacements suddenly become possible on a fault in a tectonically strained region. Gutenberg and Richter (1936) noted that the complex first motion patterns and large S to P-wave ratios suggest that deep earthquakes as well must be associated with shear failure rather than with explosive or implosive sources. A large number of recent first motion studies and a study on the long period P-wave pulse by Randall (1968) have established that shear failure is the predominant mechanism for earthquakes. Orowan (1960) pointed out that in the earth below a few kilometers depth friction on a dry fault surface

inhibits displacements across it. To overcome this problem he suggested that faulting might be initiated by creep instability. Raleigh and Paterson (1965) proposed on the basis of laboratory experiments, that dehydration of hydrous minerals at increased temperatures may lead to sudden failure and cause earthquakes. Griggs and Baker (1969) based a mechanism of shear melting on laboratory observations by Bridgman (1937).

A vast amount of theoretical work has been done describing the static and dynamic displacement and strain fields resulting from a displacement or stress discontinuity on a plane embedded in an elastic solid. In Kasahara and Stevens (1969) a summary of this work is given. Until very recently all calculations of the dynamic displacement field were based on models specifying displacements on a fault area. Burridge (1969) calculated the near field terms of the dynamic field for the more realistic source model prescribing stresses on the fault plane. Brune (1970) gave the far field terms as well for the same source and allowed for a partial stress drop. It is shown in this study that this last quality of Brune's source model is essential for the description of small earthquakes. Until recently only few workers considered the possibility of partial stress drop in earthquakes (e.g. Orowan, 1960; Brace and Byerlee, 1966). King and Knopoff (1968a) found that the stress drop for large

earthquakes is a function of magnitude. It is here shown that this relation also holds for small earthquakes and that no assumptions, other than that the source can be modeled as a shear failure, are necessary to derive this result. On the basis of the above mentioned theoretical models the source parameters of an earthquake can be derived from analysis of seismic waves. However, the relevance of these theoretical studies was so ill-established that Evison (1963) rejected the elastic rebound hypothesis, suggesting that all earthquakes were due to phase changes and that surface faulting was only a form of earthquake damage at the earth's surface. Aki (1966) and Brune and Allen (1967a) have only recently shown for two examples that fault parameters obtained from seismic data analysis based on dislocation theory agreed with the field observations. In this work such a check is provided for seven more earthquakes. All of the 393 other studied shocks could also be interpreted satisfactorily as the result of shear failure along a plane.

An important aspect of this work is the relation of tectonic processes to the hypothesis of ocean floor spreading (Hess, 1962; Dietz, 1961). Geodetic displacement measurements across active faults and the determination of slip rates from seismic analysis with the method of Brune (1968) are direct observations

of the relative movement of tectonic plates (McKenzie and Parker, 1967; Morgan, 1968; Le Pichon, 1968). It is demonstrated here that besides earthquakes, creep and displacements induced by seismic shaking can release tectonic strain. The determination of slip vectors and stress axes for large numbers of earthquakes have played a fundamental role in the development of the idea of ocean floor spreading and plate tectonics (e.g. Sykes, 1968; Isacks et al, 1968). Some regional studies of the magnitude of shear stresses are presented in this work. They provide a better understanding of the mechanism of ocean floor consumption. When more data will be available these studies will also furnish clues to the interaction of tectonic plates. The identification of weak and strong parts of plate boundaries is important to the estimate of earthquake hazard.

Much of the seismic signal analysis presented here is relevant to the problem of discriminating between underground nuclear tests and earthquakes. Particularly important in this context is the discovery that small earthquakes have, in general, an order of magnitude larger source dimensions than previously suggested by Press (1967).

Symbols

A_L	Love wave excitation function
$A = LW$	Fault area, L = length, W = width (depth).
$A(i_h)$	Radiation pattern
$D \equiv \overline{u}$	Average dislocation
E	Elastic strain energy
E_S	Seismically radiated energy
M	Seismic magnitude, M_L = local magnitude, M_S = surface wave magnitude
$M_o = \mu A \overline{u}$	Seismic moment
Q	Attenuation factor
R	Epicentral distance
$T = \frac{1}{\nu} = \frac{2\pi}{\omega}$	Period of seismic wave
a	Amplitude of seismic wave
c	Surface wave phase velocity
h	Hypocentral depth
i	Angle of incidence of seismic ray
m	Body wave magnitude
r	Earthquake source radius
$\tilde{u}$	Displacement spectral density of seismic waves
β	Shear wave velocity
δ	Dip of fault plane
ε	Strain drop

$\bar{\varepsilon}$	Average shear strain
η	Seismic efficiency
θ	Fault plane azimuth minus station azimuth
λ	Slip angle
μ	Shear modulus
ρ	Density
$\bar{\sigma} = \frac{\sigma_1 + \sigma_2}{2}$	Average shear stress
τ	Stress drop
$\omega = 2\pi\nu$	Frequency

Chapter I

DISPLACEMENT ON THE SAN ANDREAS FAULT SUBSEQUENT TO THE 1966 PARKFIELD EARTHQUAKE

ABSTRACT

Immediately following the 1966 Parkfield earthquake a continuing program of fault displacement measurements was started, and several types of instruments were installed in the fault zone to monitor ground motion. In the year subsequent to the earthquake a maximum of at least 20 cm of displacement occurred on a 30 km section of the San Andreas fault; this far exceeded the surficial displacement at the time of the earthquake. The rate of displacement decreased logarithmically during this period in a manner similar to that of the decrease in aftershock activity. After the initial high rate of activity it could be seen that most of the displacement was occurring in 4-6 day epochs of rapid creep which was often preceded by local aftershocks. The periods of rapid creep occurred with a regularity that made it possible to predict them. It is shown that on a large scale, creep and aftershocks are independent. Both processes were a response to the Parkfield earthquake, which is modeled as a buried earthquake with a dislocation of 30 cm between 4 and 10 km depth.

INTRODUCTION

The Parkfield-Cholame region is at the northernmost extremity of the segment of the San Andreas fault that was associated with the great earthquake of 1857. This area has been subjected to earthquakes of about Magnitude 6 accompanied by surface faulting four times during this century. The most recent of these events occurred on June 27, 1966 and is the subject of this chapter. An index map illustrating the extent of surface faulting in historic times and the currently active areas of the San Andreas fault is shown in Figure 1.

Because of the special geodetic control in the area, the presence of a net of strong-motion seismographs, and the large number of independent and detailed field investigations undertaken in the region immediately after the main shock, more is known about the fault motion associated with this earthquake than with any previous event of comparable size. We will present detailed measurements of fault motion as a function of position along the surface trace, the time history of creep during the year subsequent to the earthquake, and instrumental observations of fault movement that accompanied local aftershocks. During the time span covered by our measurements, the Department of Water Resources remeasured relative positions of points located 6 km on either side of the fault (Hofmann, 1968). In elastic rebound theory, displacements

of points far from a vertical fault surface will reflect dislocations at depth. In the present case, the coverage was just enough to allow us to model the dislocation as a function of depth.

Brune (1968) devised a method to estimate the slip rate over a given fault zone from the sum of the seismic moments of earthquakes that occurred there. This method was applied to the Parkfield aftershock sequence. The moments were estimated from the magnitudes, using a relation derived in the second chapter. The slip due to earthquakes was then summed as a function of position along the fault and compared to the surface displacement measured during the two years considered. It was found that creep occurred mostly where earthquakes did not occur.

In the discussion that follows it will be important to keep in mind that the area under study is a transition region between the now quiet branch of the San Andreas in the Carizzo Plains and the active areas to the north (see Figure I). Creep has been documented on the San Andreas, Calaveras, and Hayward faults some 130 km to the north (Tocher, 1960; Cluff and Steinbrugge, 1966; Radbruch and Lennert, 1966). Furthermore, Wallace and Brown (1968) have shown that considerable creep has occurred during the past half century as far south as Cholame, but that within a few kilometers south of Cholame all creep activity ceases. That the area under study is characterized by continuing moderate seismic activity, surface faulting, and high creep rates is no doubt related

to its transitional nature.

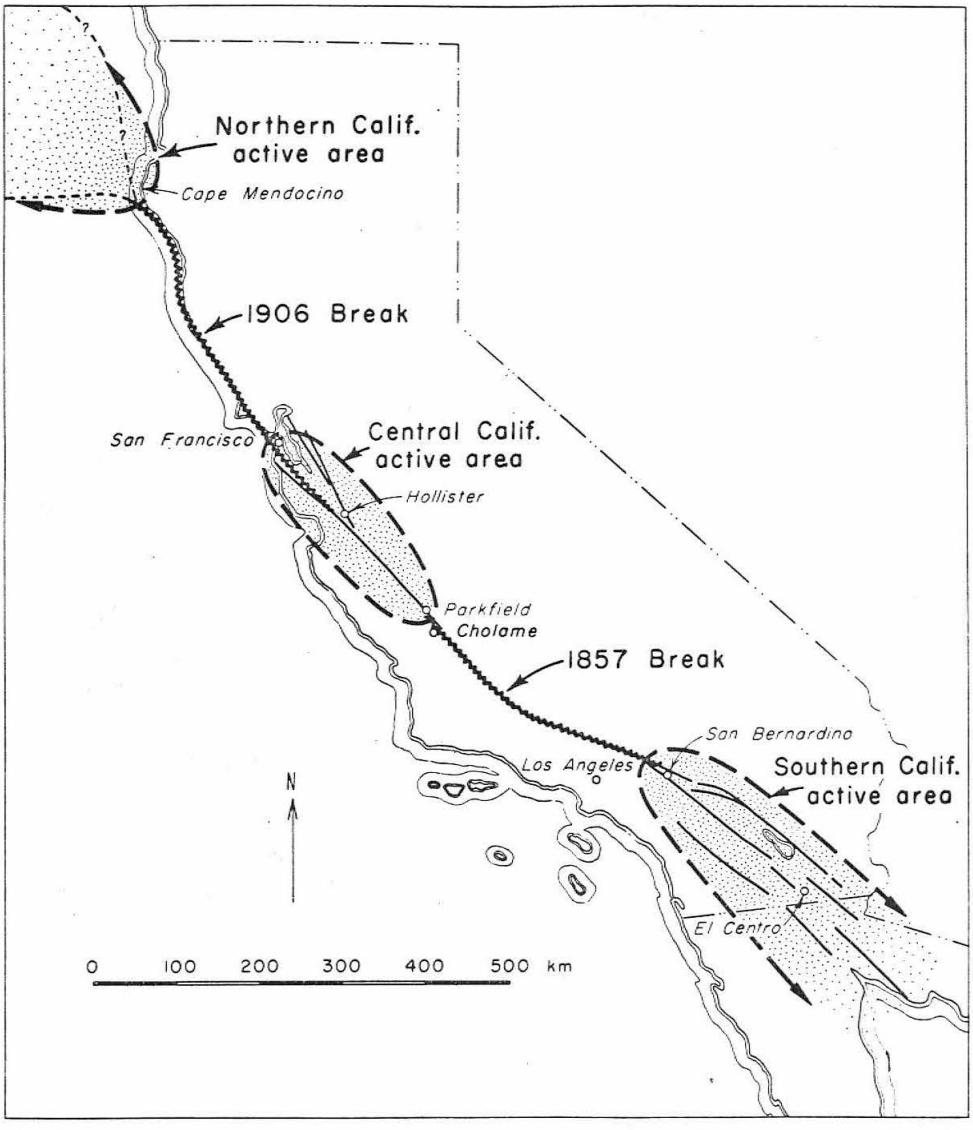

Fig. 1 Map of California showing the San Andreas fault with seismic active areas and locations of historic surface breakage, from Allen (1968). The region under investigation lies between Parkfield and Cholame.

MEASUREMENTS

Prior to the Parkfield earthquake of 27 June 1966 indications of surficial displacement along the San Andreas fault scarp in the Cholame Valley were noticed by Allen and Smith (1966). Fresh en-echelon cracks on the Taylor Ranch 1.7 km southeast of Parkfield were inspected on 16 June by the Second U. S. - Japan Conference on Research Related to Earthquake Prediction. On 18-19 June, a site near the center of the subsequent activity was occupied with a portable seismograph. A 24 hour record showed no identifiable micro-earthquakes ($M \gtrsim 1$) within 24 km (Brune and Allen, 1967b). Because the field evidence for fault motion was quite strong, and despite the lack of micro-earthquakes, a small-scale geodetic survey across the fault southeast of Parkfield was planned. This work was to start on 28 June 1966, and the field equipment was packed and ready for departure when the earthquake of 27 June occurred. Although it was suspected that the main shock had released most of the tectonic strain in the Cholame Valley, three small-scale geodetic networks, Taylor Ranch, Carr Ranch, and Highway 46 (Figure 2), were established across the fresh fault trace on 29 and 30 June and 1 July, respectively. Since during the first week of July the theodolite measurements at the Taylor Ranch revealed a continuing displacement of about 10 mm/day, three more stations, Parkfield, Peacock, and Cemetery were established on

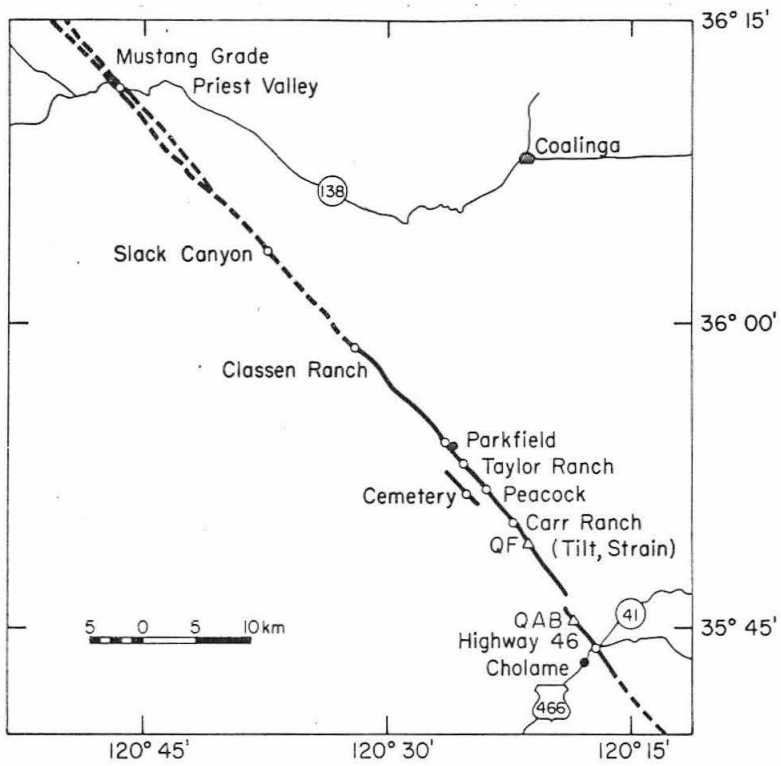

FIG. 2 Map of the Parkfield region showing the surface break associated with the 1966 earthquake as solid line. Where no rupture occurred the most recent trace of the San Andreas fault is marked by a dotted line. The locations of small-scale geodetic stations are indicated by open circles, those of quadrilaterals established by the USGS as open triangles.

Smith and Wyss (1968)

7 July. In addition, for a special study of fault motion, a tiltmeter and a strain meter were installed at Carr Ranch on 4 July. After U. S. Geological Survey personnel had mapped the extent of the fresh fault trace, a seventh station, Classen, was established on 26 August. As a result of the measurements at this locality, which indicated that the maximum rate of displacement was migrating to the north, two more stations, Mustang Grade and Slack Canyon, were established on 5 May and 7 June 1967, respectively. The locations of these

stations are shown in Figure 2 along with the most recent trace of the San Andreas fault, and their coordinates are given in Table 1.

Inasmuch as the earthquake occurred at night (2126 PDT), nothing is known of the surface faulting, if any, that accompanied the main shock itself; indeed, it may have been nil. All that is positively

TABLE 1

COORDINATES OF GEODETIC STATIONS

Station	Latitude	Longitude
Highway 46	35° 44.02	120° 17.30
Carr Ranch	35° 50.15′	120° 21.90′
Peacock	35° 51.80′	120° 23.90′
Taylor Ranch	35° 53.18	120° 25.42
Parkfield	35° 54.20	120° 26.57
Classen	35° 57.87	120° 31.93
Slack Canyon	36° 03.75	120° 37.54
Mustang Grade	36° 11.60	120° 46.20

known is that by 0700 PDT the following morning, the displacement of the white line at the Highway 46 locality was 4.5 cm. During the morning, displacements of the same order of magnitude were observed at several localities as far north as Taylor Ranch. By evening, the displacement at Highway 46 had increased to 6.4 cm and was 7.5 cm by the following noon (Allen and Smith, 1966).

During the month following the Parkfield earthquake the relative displacement was measured geodetically at intervals of about three days. To the end of 1966 it was measured every ten

days and thereafter about every thirty days. A continuous record of the quartz strain meter installed across the fault was obtained for the period of 9 July to 18 September 1966. In February, 1967 a less sensitive strain meter was installed in the place of the old one and operated continuously up to the present time.

Strain meter: As soon as it became apparent that significant fault displacement was continuing to occur subsequent to the main shock of 27 June, instrumentation was installed across the fault to record this motion. By 4 July 1966 a tiltmeter and strain meter were operating at the Carr Ranch south of Parkfield. These instruments are described in detail by Smith and Wyss (1968). The thickness of the alluvium at the site where the strain measurements were made is estimated at several hundred meters (Dickenson, 1966). Despite the fact that the fault trace is exposed in alluvium here, the currently active section is very localized, marked by a narrow band of en-echelon cracks, the width of this band being about 5 meters. Furthermore, the observations of residents in the area clearly indicate that cracking occurred within a few meters of the present zone both in 1922 and 1934. For these reasons it was possible to completely span the fault zone with an instrument of 8 meter length. Subsequent comparison with geodetic measurements within 1/2 km of this site substantiated the fact that

all of the deformation in the rift belt was actually taking place across this narrow zone (Figure 4).

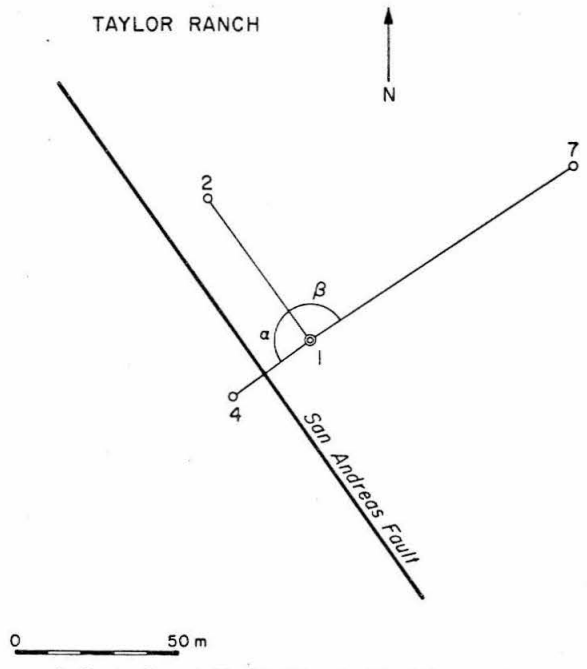

FIG. 3 Map of the geodetic station at Taylor Ranch. The Theodolite station is point number 1, and the reference points are 2, 4 and 7.

Smith and Wyss (1968)

Geodetic Measurements: Figure 3 shows the geodetic station at Taylor Ranch which is typical of the small-scale network used here. The only point occupied with the theodolite was point number 1. A reference point, number 2, was chosen such that the direction 1-2 was approximately parallel to the fault. This arrangement minimizes changes of the reference direction due to relative displacement of point 2 with respect to point 1. On the opposite

side of the fault trace a point, number 4, was chosen such that the angle α was close to 90°. In this way, to a first approximation, only displacement parallel to the fault was measured. Where it was possible, an angle β, close to -90°, was measured in order to detect displacement of points on the observers side of the most recent fault trace. This provided a check on the experimental errors and also revealed some interesting information on deformation of the fault zone.

At all stations the theodolite point is marked by a 1 meter long, 2.5 cm iron bar driven into the ground. The points to be observed are marked by nails in oak trees or telephone poles. For a time scale of a year or so this technique seems well suited for rapid installation of small-scale networks. It should be emphasized that the time required for installation was a critical factor in the first few days following the earthquake. The distances over which the displacement across the fault were measured vary from 20 to 100 meters. Using a Wild T-2 theodolite, the accuracy achieved was ± 8 seconds of arc, which for the scale of this survey on the average corresponds to ± 1.5 mm. Displacements given in this chapter are only for the component parallel to the fault.

DISCUSSION

During the months following the main shock, the strain meter data indicate that steady creep took place along the surface trace of the fault. The creep rate at the Carr Ranch varied from .01 to 3.0 mm/day and was, in general, confirmed by geodetic observations. Figure 5 demonstrates the fact that although the average rate of creep was 0.9 mm/day for three months, most of the displacement occurred during short periods at high creep rates. Some periods of accelerated creep were preceded by aftershocks in the immediate vicinity of the Carr Ranch, and some aftershocks were accompanied by sudden right lateral fault displacement of a few millimeters (Smith and Wyss, 1968).

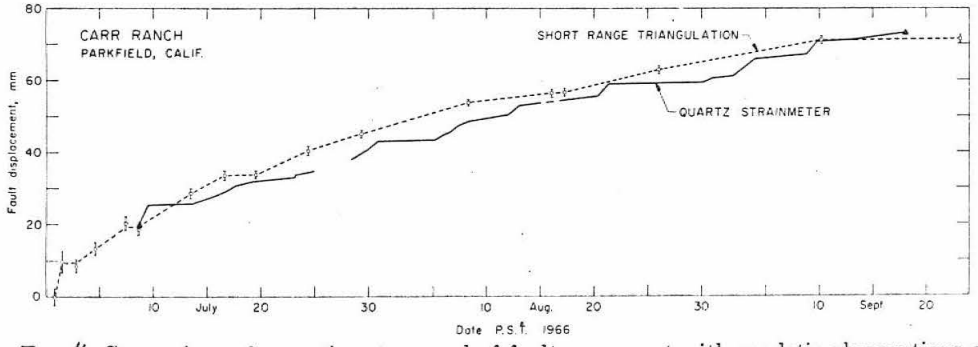

FIG. 4 Comparison of a continuous record of fault movement with geodetic observations at the same site.

Smith and Wyss (1968)

The geodetic observations discussed below confirm the fact that the surface displacements associated with these aftershocks ($M < 3.5$)

are confined to a region within a few km of the epicenter.

The temporary strain meter became unusable following the first heavy rains of the winter. In February, 1967, a less sensitive device was installed across the fault at the same location. The quartz tube was replaced with a taut Invar wire suspended within a 6" tube. A cantilevered block pivoting on a Teflon bushing provided a constant tension of 20 lbs. on the wire. A dial gauge micrometer in contact with this block makes possible manual readings of fault displacement to ± .0002 inch. A linear-motion potentiometer is installed in place of the micrometer for periods during which continuous recording is required.

Figure 5 shows the fault displacement detected by this instrument. The large displacements occurring during the several days following each individual local earthquake are much clearer in this record than they are in Figure 4, where the rate of aftershocks was higher. The predominant mechanism for surface fault displacement here is one of accelerated creep associated with local shocks.

A summary of geodetic measurements is given in Figure 6 where the displacement parallel to the fault as observed at the different stations is plotted versus time. Since the measurements were not started simultaneously at all stations, and since the absolute displacement is known only for the Highway 46 locality, the starting values for the other stations shown in Figure 6 are somewhat arbitrary.

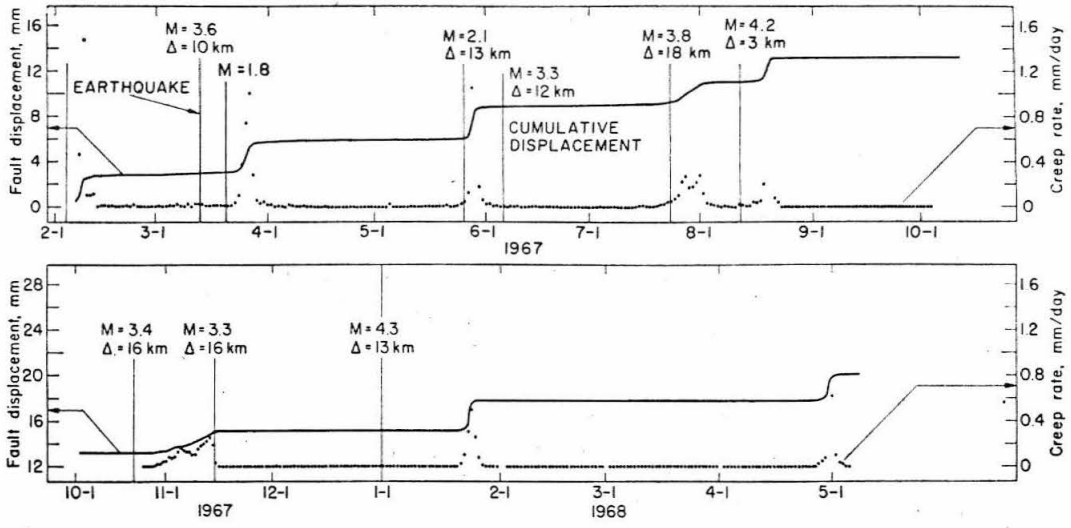

Fig. 5 Creep rate and cumulative creep measured with the Invar wire creepmeter at Carr Ranch during 1967 and 1968. Earthquakes and their distance from the creepmeter and magnitude are noted. Note the episodic nature of creep.

Smith and Wyss (1969)

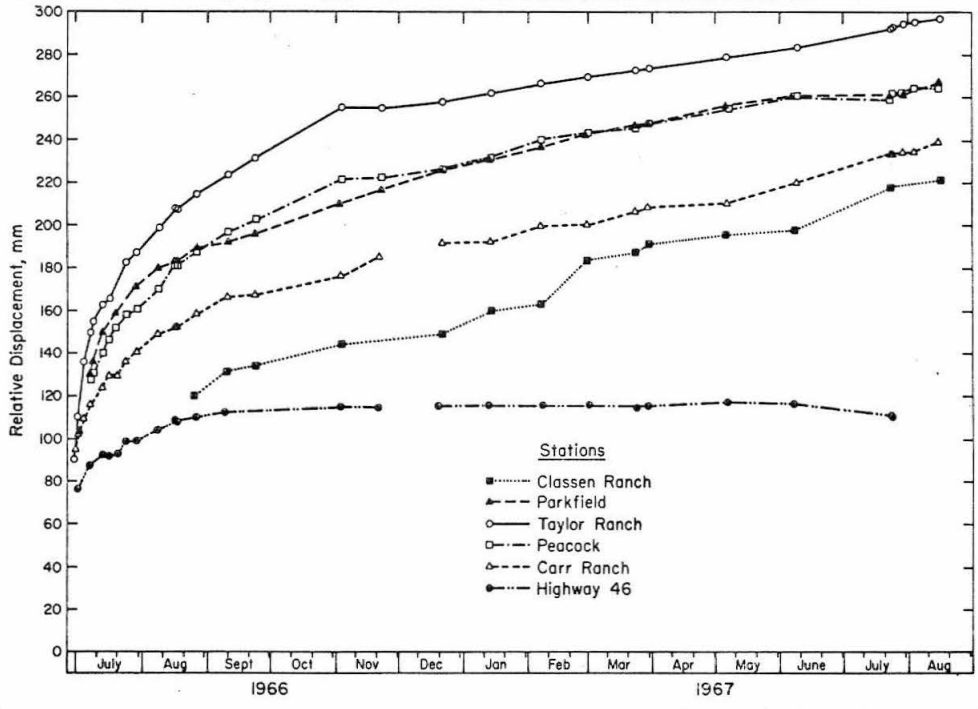

FIG. 6 Cumulative displacement across the fault trace measured geodetically at six stations in the Cholame Valley region. The locations of the stations along the fault are shown in Figure 2.

Smith and Wyss (1968)

The starting values for the earliest measured stations at Carr Ranch and Taylor Ranch were taken so that the observed initial rate of displacement would extrapolate back to zero-displacement at the time of the earthquake. The starting value at Peacock was assumed by linear interpolation between the displacements at Carr Ranch and Taylor Ranch on 7 July. The similarity of the displacement curves obtained at Peacock and Parkfield together with the displacement distribution along the fault (Figure 12), suggest that the displacement is distributed symmetrically with respect to the center of the fault which appears to be located close to the station Taylor Ranch. The starting values of Parkfield and Classen Ranch were determined assuming the aforementioned symmetry. The zero point of the scale in Figure 6 was chosen such that the first geodetic measurement at Highway 46 was equal to the offset of the white line on the highway at the time of the first measurement. All these assumptions do not influence significantly any of the curves and conclusions discussed here. The flooding that occurred in December, 1966, in the Cholame Valley disturbed the stations Carr Ranch and Highway 46. The creep for the period of 22 November to 21 December was approximated by interpolation of the rates of displacement before and after the flood and added to the accumulated displacement.

The maximum rate of displacement decreased logarithmically from 10 mm/day two days after the main event to 0.17 mm/day one year thereafter. During the whole period of measurements the largest amount of total relative displacement was observed at Taylor Ranch. Comparison of these data with the quadrilateral measurements carried out by E. F. Roth (Brown et al, 1967) shows that for a period of one month after the earthquake, displacements at his location QAB were larger than those at Taylor Ranch. Roth obtained displacement values by measuring the length of the sides and diagonals of quadrilaterals. These had the dimensions of 7 to 60 meters and straddled the fracture zone. They were measured repeatedly up to 15 August 1966. The results of two of the 9 quadrilaterals were taken from Brown et al (1967) and included in Figure 12.

The frequently repeated geodetic measurements at the various localities resulted in curves with a very similar overall shape (Figure 6 and 9). The large creep rate decreased roughly logarithmically. A more detailed examination of the curves, however, shows that during the time where some stations accumulated a centimeter or more of displacement, others did not move at all except for a few instances. It is evident therefore that the fault moved in segments smaller or equal to the distance between stations which is of the order of 5 km.

Periods of several months during which the rate of displacement at one or the other station was comparatively large with respect to the other stations, were followed by periods with a comparatively low displacement rate. The Parkfield station for example, shows a higher rate of displacement than any other station from 7 July to 28 July, 1966. This period must have been preceded by one of low displacement rate, since on 7 July no surface evidence of ground movement could be detected at this locality. From 28 July to 23 November 1966 the fault section including Taylor Ranch and Peacock was the most active one. After 3 November, the rate of displacement at the Parkfield station was again the largest, until after 25 December when the largest activity was recorded at Classen Ranch. This development suggested that perhaps the fault was migrating to the north. In the period of measurement of 6 June to 15 August 1967, the central portion of the fault was the most active one again. Taylor Ranch showed an increased rate of displacement, and several shocks with magnitudes of about 3.5 occurred.

The stations Mustang Grade and Slack Canyon were established in order to determine the northernmost extent of creep in this region. It was hard to find a well developed fault trace close to and north of Classen Ranch. Numerous landslides obscure the fault trace and, in addition, the region is not easily accessible for theodolite measurements. For these reasons the stations were

established 12 and 30 km, respectively, north of Classen Ranch.

By July, 1967, Slack Canyon showed no displacement and Mustang Grade showed 1 cm of right lateral movement. By January, 1968, both stations had displacements of about 1.5 cm. These rates of displacement are much smaller than the ones observed near Parkfield. The two regions probably creep independently.

In order to verify the assumption that displacements were occurring parallel to the fault, and to check the observational accuracy of our surveying technique, several alternate points at different angles were measured at both the Parkfield and Peacock localities. In Figure 7 it can be seen that the agreement between different measurements is quite good. Since the angular measurements are converted to displacement parallel to the fault by dividing by the sine of the angle across the fault, significant displacement normal to the fault would have produced divergent results in Figure 7.

The solid circles in Figure 7 represent the values of displacement derived from angles corresponding to the angle β at Taylor Ranch (Figure 3). The reference direction was parallel to the fault and the observed point at right angles to it, not across, but away from the fault trace. This angle β was originally measured only as a means for checking the internal consistency of the method

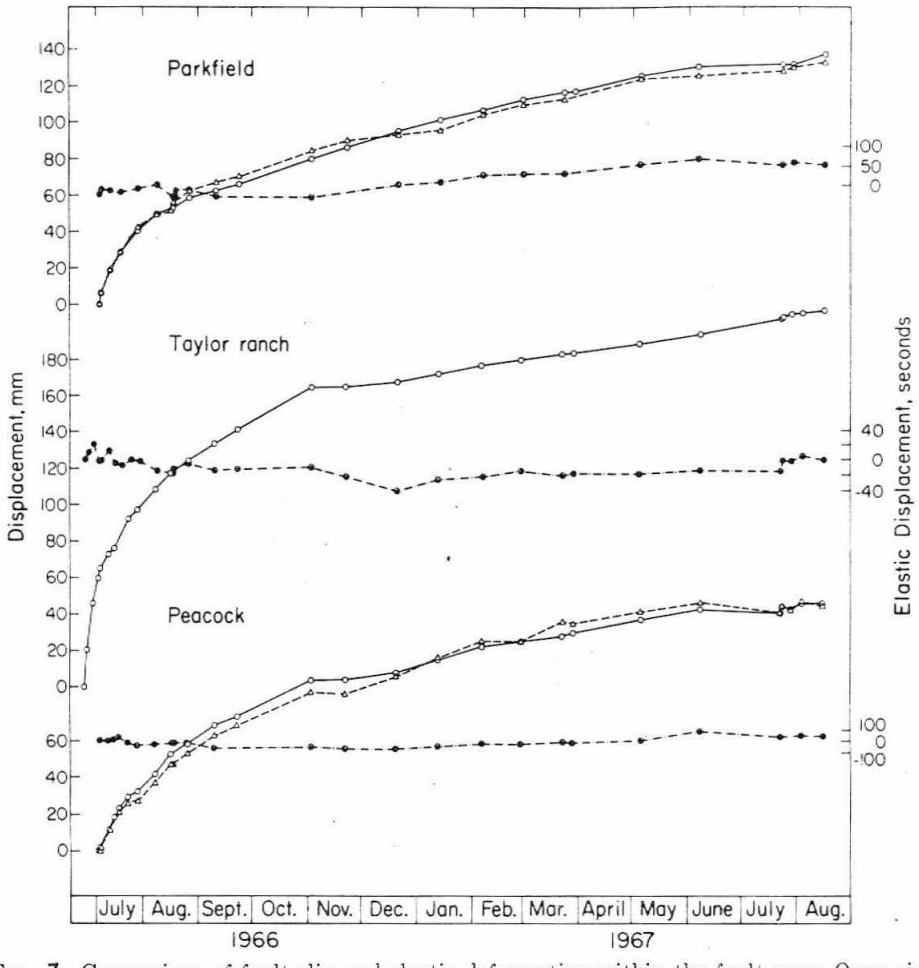

FIG. 7 Comparison of fault slip and elastic deformation within the fault zone. Open circles and triangles represent deformation of geodetic lines crossing the fault whereas solid circles are obtained from lines lying entirely on one side of the fault. These measurements correspond with the angles α and β respectively as shown in Figure 3.

Smith and Wyss (1968)

used for determining fault displacements. Since the points are all on one side of the fault, and there are no surface cracks between them, the relative displacements should remain zero at all times unless the region is being deformed elastically. It was soon noted that the angle β did not remain constant, but occasionally increased for a period of time and later rebounded to approximately its original value. This behavior was very suggestive of the occurrence of recoverable elastic strain in the fault zone. This measurement also showed that at Peacock, Taylor Ranch, and Parkfield, the slip and creep displacements are confined to a zone narrower than 20 m; which is consistent with the field observations. The scale for these angles is given in seconds of arc on the right side in Figure 7 and is arranged such that the corresponding displacements can be read from the millimeter scale on the left. Positive values correspond to right lateral displacement. The elastic deformation can best be seen in the Taylor Ranch data, an enlarged version of which is shown in Figure 8. The curve representing elastic strain in the fault zone shows two significant increases during the month of July, 1966. The displacement of geodetic marker number 7 shown in Figure 3 during these build-ups is 10 mm and 6 mm respectively, and corresponds to a strain of about 10^{-4}. Each of these build-ups is followed by a strain relaxation of about equal magnitude. In the first example shown

in Figure 8, the relaxation occurred sometime between 4 July and 7 July, when the geodetic measurements were repeated. During this time two aftershocks occurred within a few kilometers of the Taylor Ranch. The locations for these shocks was obtained from McEvilly et al (1967) and the pertinent data are as follows:

5 July 1966, 6 km north of Taylor Ranch, depth 3.6 km, M = 3.1

7 July 1966, 3 km north of Taylor Ranch, depth 4.6 km, M = 3.0.

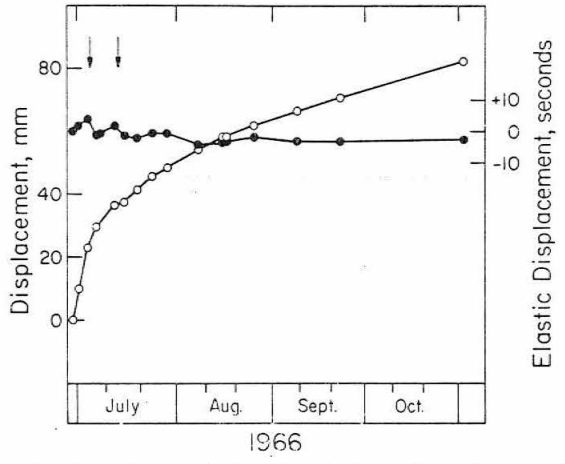

FIG. 8 Possible strain relaxation at Taylor Ranch shown by a decrease in elastic strain (solid circles) and an increase in fault displacement (open circles) accompanying two nearby earthquakes (arrows).

Smith and Wyss (1968)

Although we do not know exactly at what time during this interval the displacement of the geodetic reference points took place, it does seem reasonable to associate the observed strain relaxation with the occurrence of these aftershocks. During the same time as the relaxation, a slip of about 12 mm took place on the fault trace as can be seen on the lower curve in Figure 8. Another possible

strain build-up can be seen in mid-July with the subsequent relaxation taking place some time between 13 and 16 July. We note that an aftershock of magnitude 2.8 occurred about 1.5 km from this site on 14 July. This same aftershock was probably responsible for the strain relaxation that occurred at the Peacock locality (Figure 7) between 16 and 17 July 1967.

The Logarithmic Time Dependence of the Creep

The same data as in Figure 6, but extended to two years after the main event, are plotted with a logarithmic time scale in Figure 9. The ordinate for the data at each station is arranged so that the stations from north to south in the fault area are shown from top to bottom in the diagram. The time scale was arbitrarily fixed so that the origin time of the main shock is at t = 1. The clearest features to be observed, is that for long periods of time the data fall on straight lines. The creep decays logarithmically in time. This pattern is most regular at Taylor Ranch, the station closest to the center of the break. Some steps in the straight lines and some changes of slope are associated with aftershocks. This is in agreement with the correlations in Figure 5. One question remains: Do the earthquakes in general trigger the creep episodes, as is the case for one example given by Smith and Wyss (1968), or could sometimes

the creep displacements trigger local earthquakes?

If one inspects Figure 5 carefully, one may get a hint pointing to the second possibility. Some of the earthquakes occurred at times when the creep rate had already started to accelerate. This is best seen by considering the dotted line in Figure 5.

Next we consider the data accumulated by the strain meter (Figures 4 and 5) plotted against a logarithmic time axis in Figures 10 and 11. The earlier data (Figure 10) are not very clear, presumably, because the aftershock activity was still very high. If we concentrate on Figure 11, a most interesting observation emerges. The beginning and the end points of each creep episode describe straight parallel lines. The parallelism suggests that each creep episode releases a critical amount of strain, and the straightness suggests that such strain is being accumulated and released at a logarithmic rate in time. This may be understood in the following way. Strain is supplied from depth

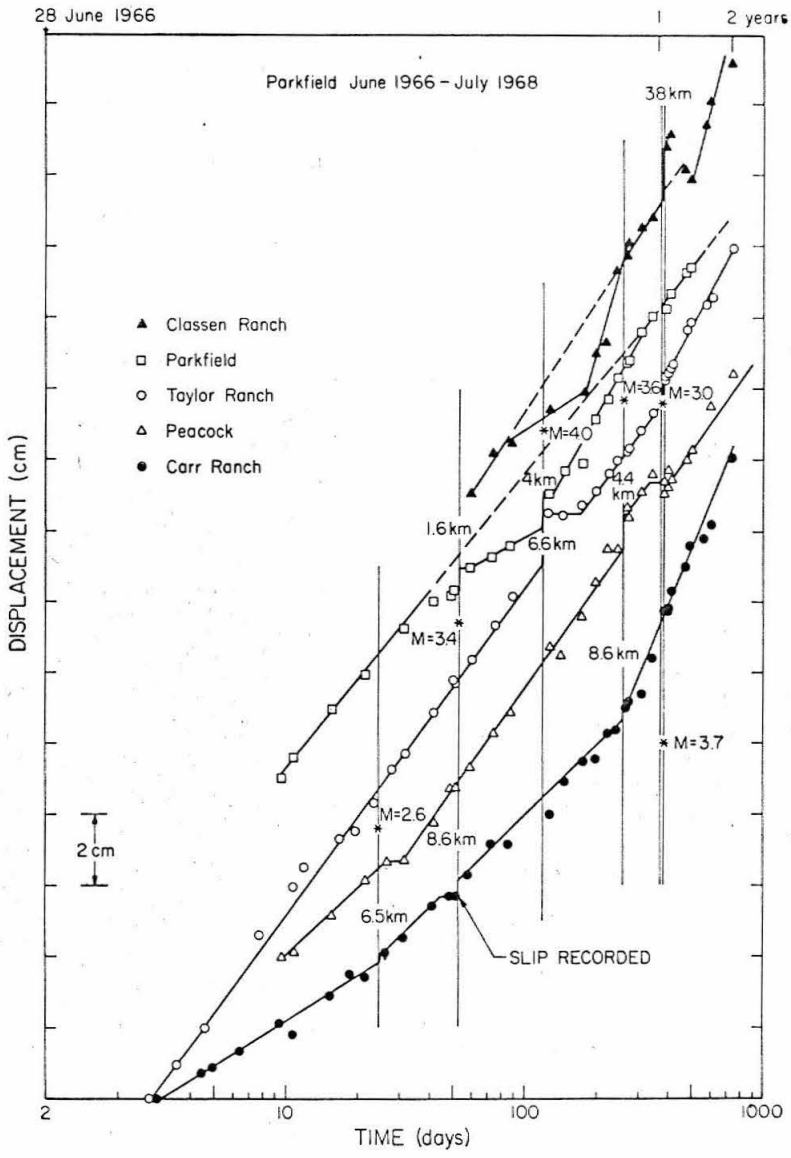

Fig. 9 Cumulative slip across the fault following the Parkfield earthquake measured with five small-scale geodetic networks and plotted semilogarithmically against time. The ordinate intercepts are arranged arbitrarily so that stations from north to south are from top to bottom in the figure. The mainshock was at $t = 1$. The occurrence of several aftershocks which seem to have affected the creep are indicated by vertical lines with asterisks to indicate the relative position of the epicenters with respect to the theodolite stations and with the distances noted to associated measured slips.

Scholz, Wyss and Smith (1969)

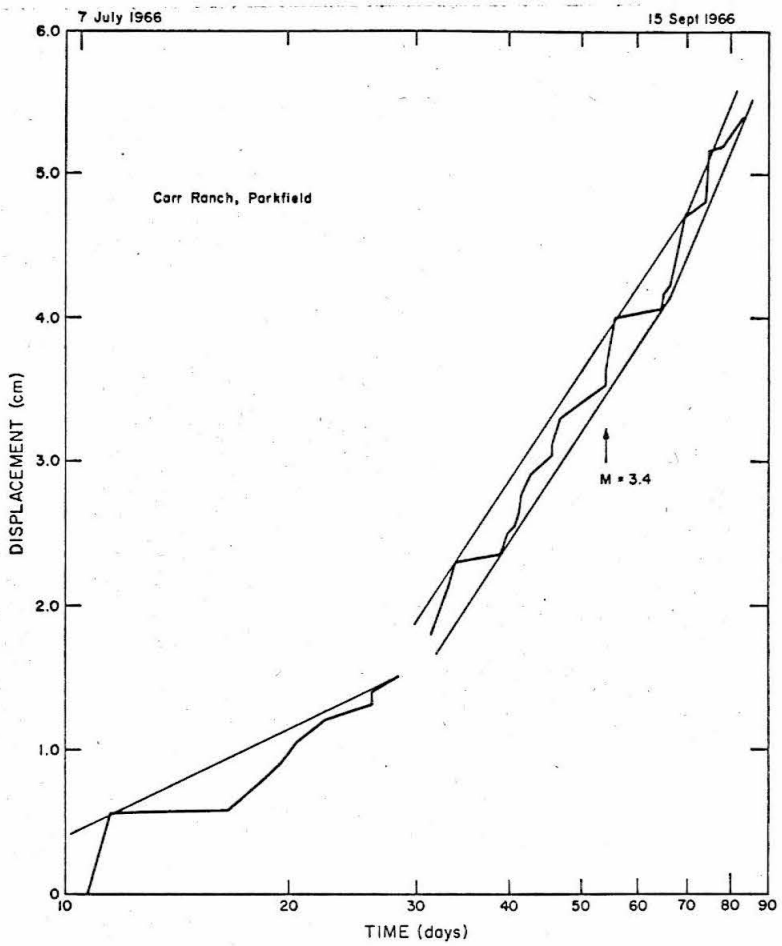

Fig. 10 Same as Figure 11 at an earlier time when a quartz tube straddled the fault.

Scholz, Wyss, and Smith (1969)

at a logarithmic rate. When the accumulated stress exceeds the static frictional strength of the fault zone, creep slowly starts. During this process the strength of the fault zone locally decreases to the dynamic frictional strength. If the fault surface is not altered between creep events, each time the same stress drop will

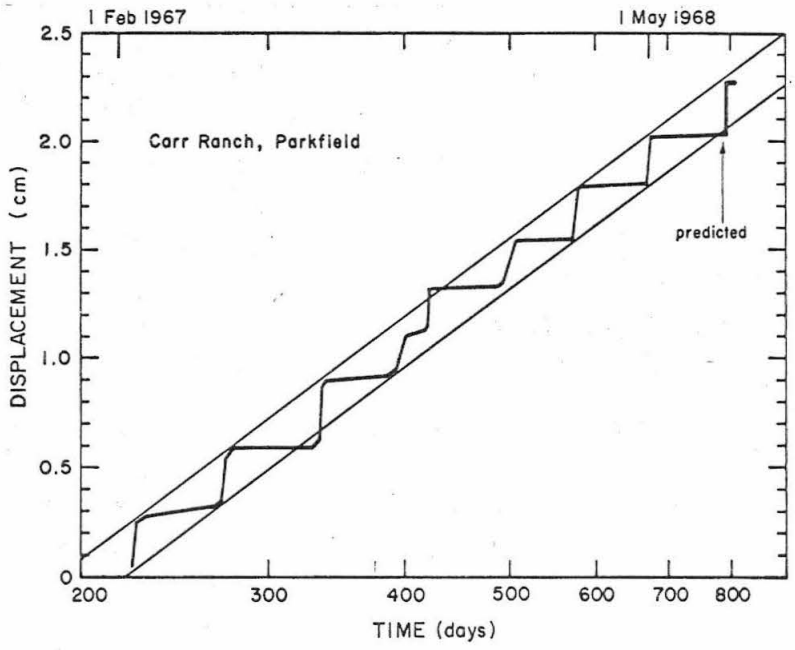

Fig. 11 The cumulative creep from Figure 5 is plotted semilogarithmically. The beginning and end of creep episodes define two straight parallel lines. The mainshock was at day 1.

Scholz, Wyss, and Smith (1969)

occur. This stress drop corresponds to the difference between static and dynamic frictional strength. During the majority of creep events, a constant displacement of 0.2 cm is accumulated.

Earlier, it was observed that one creep episode could extend over portions of the fault smaller or equal to 5 km. This value is close to the depth of the creep zone as will be derived later. Therefore, it is estimated that the creep events relieve stresses of the order of 0.1 bar. This suggests that the difference between dynamic and static friction is of the order of 0.1 bar.

In this light it would seem that an earthquake could only trigger a creep period at times when the locality is stressed almost to the strength of the fault zone. In Figure 11 this condition is fulfilled each time when the displacement-time curve approaches the lower straight line. The starting and stopping of the accelerated creep episodes occur with an amazing regularity. In all cases except for the one irregular double period, the actual beginning and end points are within 0.05 cm of the straight lines. This regularity makes it possible to predict the occurrence of creep episodes with a high confidence. On this basis, the episode of August 22, 1968, was predicted (three months in advance) to occur on August 15. This was the first successful prediction of motion on the San Andreas fault.

The changes of slope of the limiting lines in Figure 10 and 11 need explanation. Comparison of the strain meter data with the small-scale geodetic data at the same locality indicate that after January, 1967 (200 days after the Parkfield 1966

earthquake) the strain meter was no longer straddling the entire fault zone. For this reason the slope in Figure 11 is smaller than the prevailing slope in Figure 10. The changes in slope during the earlier period of measurements, however, are also reflected in the geodetic measurements. Several changes in the slope of displacement versus log t plots can be seen in Figure 9, most notably at Carr Ranch. These changes cannot be explained by the occurrence of local shocks. This phenomenon represents a change of the decay constant, which is probably due to a change in stress. This may be a result of an original variation of stress concentration along the length of the fault following the main shock, resulting in some sections of the fault 'leading' others in creep. For almost a year after the main shock surface displacement was accumulating faster at the center of the fault, Taylor Ranch, then toward the southern end, at Carr Ranch (see Figure 9). The strain between these two points due to the difference in creep rates reached 10^{-5} in about 130 days. After this time the rate of creep at Carr Ranch increased in such a way as to catch up with the more northerly points. It is very likely that neighboring portions of the fault influence one another in this way, although an explanation for the suddenness of the transitions is lacking.

Change of Displacement Along the Fault

Many previous field investigations of active faults have revealed that total measured offsets take on a wide range of values over the length of a surface break. In this study only the creep displacement which occurred subsequent to the initial displacement, which presumably accompanied the main shocks, is studied. The cumulative creep represents, in this case, a better picture of the total fault displacement occurring at depth than can be obtained from initial surface offset.

A way to estimate the slip that occurred during the earthquake is to calculate the seismic moment as defined in the dislocation theory of faulting, and divide it by the fault area (see Aki, 1966; Maruyama, 1963; Haskell, 1963; or Burridge and Knopoff, 1964). In this calculation we need only assume that the fault slip occurred during a time short compared with the period of the seismic waves that we analyze. Using the relation between seismic moment and the area of the envelope of the surface waves which is established for shocks in the Parkfield area in the second chapter, we obtain a moment of 1.9×10^{25} dyne-cm for the main shock. Aki (1967) obtained a value of 1×10^{25} dyne-cm for the same earthquake. The sum of the moments of the shocks that occurred in the Parkfield region between the 27 June 1966 and 1 January 1968, with moments

of at least 1 x 10^{22} dyne-cm, is ΣM_o = 2.1 x 10^{25} dyne-cm. From this value we compute the average cumulative displacement corresponding to all these shocks using

$$\Sigma\overline{U} = \frac{\Sigma M_o}{A_o \mu}$$

where $\overline{U}$ is the average displacement of one shock, A_o = 44 km x 14 km, the total fault area along which the shocks are distributed and μ = 3 x 10^{11} dyne/cm^2 is the rigidity, and obtain $\Sigma\overline{U}$ = 11.4 cm. The average displacement over the same area for the main shock alone corresponding to a moment of 1.9 x 10^{25} dyne-cm is 10.3 cm. Comparing these two displacement values we conclude that the surface displacements which continued during the year subsequent to the main shock cannot be attributed to aftershock activity alone. The observed average cumulative displacement for the period of 30 June 1966 to 15 August 1967 is about 13.5 cm. The displacement, that occurred between the 22 and 30 June 1966 is estimated to be the same as the offset of the white line at Highway 46 that occurred during this time which was 7.5 mm. The total average displacement observed geodetically then amounts to 21 cm. A summary of the displacements determined in different ways is given in Table 2. From these results there appears to be an excess of average displacement of about 10 cm along the fault which is not reflected

in radiated seismic energy. In this model we are lead to conclude therefore, that a substantial amount of displacement, about 10 cm, was produced by creep, which could have occurred over the entire fault surface down to depths of at least 14 km. This model, however, is too crude and will be refined using the data on the displacement history at points 6 km perpendicular away from the fault.

TABLE 2

Average displacement of the main shock determined from seismic moment	10.3 cm
Average cumulative displacement corresponding to the sum of the seismic moment of the entire earthquake sequence	11.4 cm
Total cumulative surface displacement observed within 100 m of the fault trace 27 July–15 August 1967	21 cm
Displacement for points 5 km distance from the fault plane by geodimeter observation between October 1965 and July 1966	20 cm

Smith and Wyss (1968)

In Figure 12 the total fault motion subsequent to 30 June 1967 is plotted as a function of position along the fault. The family of curves represents the accumulated displacements at different times during the year following the earthquake.

For the construction of Figure 12 a number of assumptions were necessary. First it was assumed that on 30 June the displacement all along the fault was zero. Of course this assumption is not true. On Highway 46 at Taylor Ranch and on a locality on the Parkfield road, cracks had been observed on 30 June, whereas other localities on the Parkfield road, which later showed cracks, had none at that time. The information is not detailed enough that we could complete Figure 12 for the time between 27 and 30 June. Second, the measurements were not started simultaneously. At the Peacock and Parkfield localities they were started on 7 June, at QAB (USGS) on 8 June, and at Classen Ranch on 15 August. For Peacock and QF an initial value was obtained by linear interpolation between

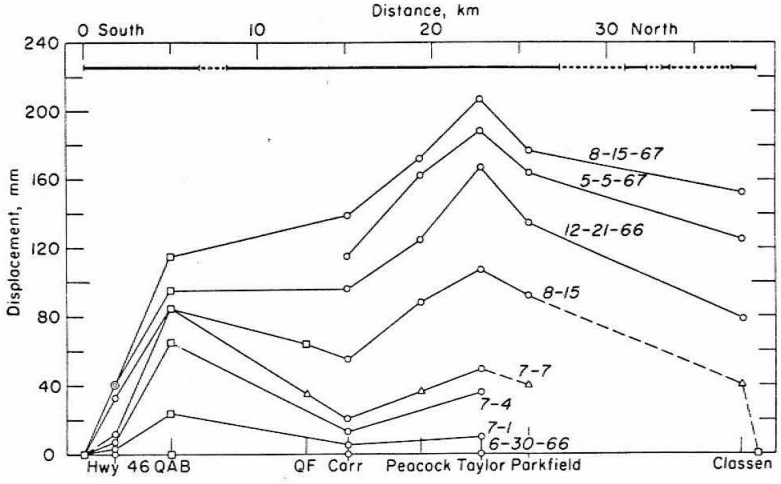

FIG. 12 Cumulative displacement along the fault trace, time is the parameter. Circles mark geodetic measurements, squares mark values taken from Brown *et al* (1967). Triangles mark the assumed starting values for stations which were established after 30 June 1966. The straight line on top symbolizes the fault trace, being solid where surface breakage was observed and dotted where such was absent at the time of the geologic mapping.

Smith and Wyss (1968)

the displacements of neighboring stations. The initial value for the Parkfield station was obtained by assuming symmetry of the pattern with respect to the point of maximum displacement, Taylor Ranch. The value of 15 August for Classen Ranch was estimated by extrapolating the displacement versus time curve obtained at this station back to the 30th of June. All these assumed values are marked by triangles in Figure 12.

The extremities of the region of surface cracking as mapped by R. D. Brown and J. G. Vedder were assumed to be points of zero-displacement. The mapping was completed on 15 July 1966 (Brown et al, 1967). It is quite likely that subsequently the region of cracking extended beyond these points.

Figure 12 shows that in December, 1966, about half a year after the Parkfield earthquake, the fault displacement as a function of position along the fault has reached a pattern which remained stable until August, 1967. In this pattern, by August, 1967, about 80% of the length of the surface break shows an offset of 120 mm or more. The decrease from this value to zero at the ends of the fault takes place in 10% of fault length (4 to 5 km) at the north and south ends. The Taylor Ranch station, located approximately in the middle of the fault trace, displays a conspicuous maximum. Before December, 1966 the pattern was different. Small values at the Carr Ranch dominate the picture. For about

a month after the earthquakes, the displacements at QAB (USGS) close to the south end were larger than the maximum at Taylor Ranch. Since there was no coverage between Carr Ranch and QAB, the straight lines connecting the displacement values of these two stations are questionable. The fault trace crosses from the east side of the valley to the west side 8 km north of Highway 46. No surface rupture could be detected along this 1.5 km long bend in the fault trace (dotted fault trace in Figure 12). For an interval of time up to a week after the earthquake, one could assume zero-displacement on this portion. This would explain the early small displacements at Carr Ranch, and would suggest that the two branches of the fault were separate breaks. A connection between the two breaks seems to have stablished itself between 7 July and 21 December 1966.

Now the correlation between creep and aftershocks will be tested by comparing the surface displacements with the displacements inferred from aftershocks. We make this comparison in the following way.

The sum of the moments of all earthquakes that occur in a given time on a particular fault plane can be divided by the product of the area of this plane with the appropriate shear modulus. The result is the cumulative displacement per unit fault length corresponding to the seismic activity during the time considered

(Brune, 1968). The most comprehensive study on hypocenters of the Parkfield sequence was made by Eaton (1968). This study included only events that occurred between July and 15 September 1966; the corresponding magnitudes are not yet available. The list of shocks compiled by McEvilly et al (1967) gives the magnitudes but it is less complete. Shocks up to 12 January 1967, are included in that list. For events after this date up to the present writing, the Pasadena Local Bulletin was used.

The hypocenters of all the earthquakes included in these three sources were projected onto the fault plane of the Parkfield 1966 break. Then the moment of each shock was obtained. The fault plane was broken down into segments 2 km long and 10 km-deep. The moment of all shocks located in each segment were summed and divided by the product of the segment area (20 km^2) and shear modulus (3×10^{11} dynes/cm^2). The average displacements caused by seismic events on fault segments obtained in this way are compared with the geodetically measured displacements in Figure 13.

The moments of the larger earthquakes are obtained in the second chapter. The moments of smaller shocks were obtained by the moment-magnitude relation given for Parkfield earthquakes in that same chapter. The displacement corresponding to the numerous shocks for which no magnitudes were available was estimated as follows: by using magnitudes given by McEvilly et al (1967) and the moment-magnitude

relation of the next chapter, the average moment of a Parkfield shock ($2 \leq M \leq 3.5$) was determined. This value was then multiplied by the number of shocks with unknown magnitude per segment.

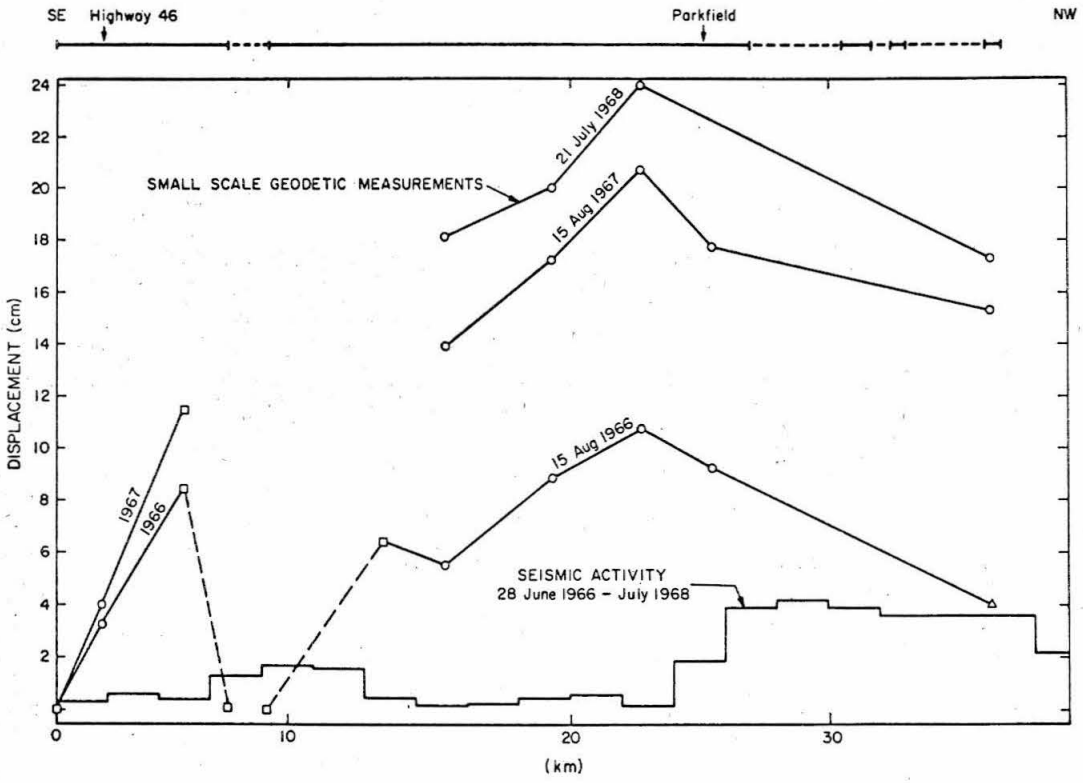

Fig. 13 Displacements across the San Andreas fault following the Parkfield earthquake as a function of position along the fault. Actual displacements measured with small-scale geodetic networks are compared with the displacements inferred from aftershock activity using the moment displacement relation. Note the anticorrelation.

Scholz, Wyss, and Smith (1969)

This procedure is believed to be a fair estimate since (1) the magnitudes of all the large and important shocks are assigned and (2) the number of shocks per segment was between 20 and 100, which

justifies statistical treatment.

Earthquakes of $M_L \geq 3.5$ are expected to have fault dimensions larger than 2 km. The fault dimensions of such shocks were estimated from the magnitude-fault length relation found in the second chapter. Then the moments were distributed among a corresponding number of neighboring segments. A shock of magnitude 5, for example, is estimated to have fault dimensions of about 14 km; therefore, its contribution to displacement was distributed among seven 2 km segments centered around the epicenter.

In Figure 13 the displacements are plotted as a function of position along the fault. The fault trace as mapped by Brown and Vedder (1967) is indicated as a solid line on the top of the figure. For reference, the locations of highway 46 and the town of Parkfield are indicated. The displacements obtained by small-scale geodetic measurements are relative to 30 June 1966; on this date the displacement all along the fault was assumed to be zero. The displacements as calculated from the seismic activity were obtained from the contributions of all shocks that occurred between 27 June 1966 and November 1968, except for the contribution of the main shock.

Comparing the displacements obtained in the two different ways, we observe two things. First, the displacement obtained from small-scale geodetic measurements are approximately an order of

magnitude larger than the ones inferred from seismic activity. Second, regions of large surface displacements correspond to regions of low seismic activity, and conversely. The seismic activity clusters around the ends of the main fault segment where the surface displacements decrease and go to zero. It is concluded that creep and aftershocks were, in general, independent processes both relieving stress concentrations produced by the Parkfield main shock.

Displacement Variation Perpendicular to the Fault Trace and Mechanism of the Parkfield Main Shock

As little as 10 hours after the mainshock, when slip by creep was taking place at a very rapid rate, Allen and Smith (1966) found that only a 4.5 cm displacement had taken place across the white line on Highway 46. Observations elsewhere on the fault also indicated that the amount of slip produced during and shortly after the mainshock was small in comparison to that eventually produced by creep. Extrapolation back in time on the creep curves that were presented above led to the conclusion that possibly no slip had occurred at the surface during the main shock. Even disregarding this extrapolation, the large-amplitude surface waves (Wu, 1968) and accelerations (Aki, 1968) both indicate, when compared with measured surface displacement, that slip during the main shock must have been much greater at depth than at the surface. This conclusion is also supported by the geodetic

measurements of Hofmann (1967), which showed that almost 20 cm displacement had taken place 6 to 8 km from the fault by July, 1966.

All the evidence thus points to a buried fault that underwent a considerable amount of slip at depth. Little or no slip occurred in the surface layer immediately during the earthquake, but creep was initiated which resulted in substantial slippage over the next few months. This suggests a causal relationship between the earthquake and the creep that followed it: the main shock did not propagate to the surface; consequently, the layer between the slipped region and the surface was highly stressed. The response of this layer was fault creep.

Hofmann (1968) remeasured the California Department of Water Resources geodetic network in the Parkfield area and found that points 6 km from the fault had moved 2.5 cm between July, 1966, immediately after the main shock, and May, 1967. It was during this period that extensive creep occurred on the fault. At the Taylor Ranch theodolite station, located near the center of Hofmann's network, 11.5 cm of displacement across the fault was recorded during the same time interval. These two measurements can be used in conjunction with elastic theory to estimate the depth of the creep zone. By fitting various models of fault slippage (Chinnery, 1961; Walsh, 1968) to the measured displacements (Figure 14)

the depth of the creep zone, and accordingly the top of the zone faulted during the main shock, was determined to be between 2 and 4 km.

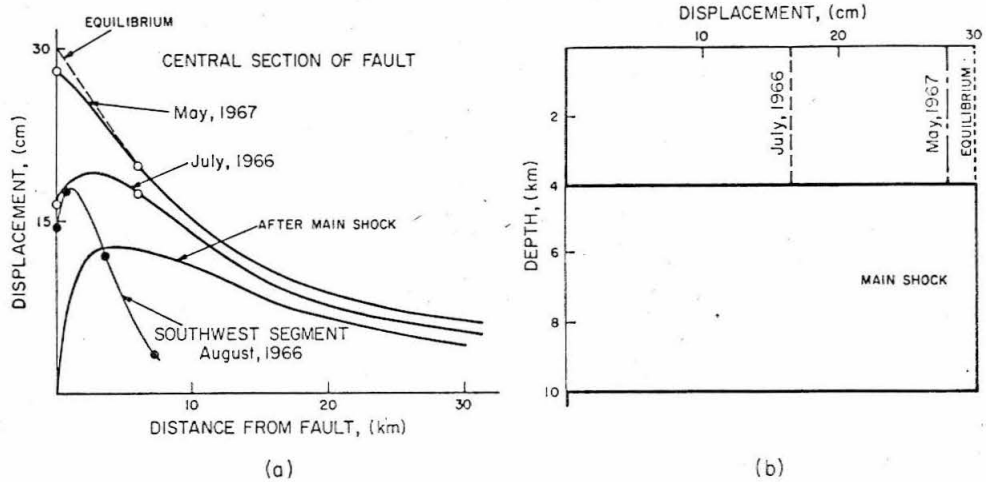

Fig. 14 Fault slip and displacements during and following the June 27, 1966, earthquake. The right-hand figure (*b*) shows the inferred variation of slip with depth in the central section of the fault due to the main shock and at several later dates after creep had occurred in the surface layer. In the left-hand diagram (*a*), calculated displacements are shown for the central section of the fault immediately after the main shock and at two later dates where they are fitted to creep at Taylor Ranch and *Hofmann*'s [1967, 1968] points (open circles). Displacements on a line across the southwest segment of the fault are also shown as solid circles [*Wallace and Roth*, 1967; *Meade*, 1966].

Scholz, Wyss, and Smith (1969)

Eaton (1968) found that aftershock activity decreased very rapidly below 10 km. No aftershocks were observed below 12 km. It is very likely, therefore, that the bottom of the zone that slipped during the main shock was at about 10 km. Taking as our model a dislocation 40 km long which slipped from 4 to 10 km depth,

we find from the seismic moment of 1.9 x 10^{25} dyne cm that a total slip of 30 cm occurred during the main shock. By early 1968, when creep activity had slackened to a very low rate, nearly all this displacement had been released at the surface by creep. At that stage, the geodetic displacements are consistent with a surface fault of 10 km depth which slipped 30 cm, and released 2.5 bar stress.

In Figure 14 we illustrate our model. The displacements from the main shock were calculated from Chinnery's (1961) model. We assumed that the upper creep zone behaved like Walsh's (1968) model 1, with $d/d_o = 1$. In the left-hand diagram the theoretical displacement curves are fitted to the data. The fit to the creep data and to Hofmann's (1967, 1968) measurements is extremely good. According to this result, a zone from 4 to 10 km slipped 30 cm during the main shock, followed by creep in the surface layer. The upper 4 km had slipped 16.5 cm by July, 1966, and by May, 1967, 28 cm, nearly all the stored slip, had been released by creep. The creep layer probably does not correspond to a geologic layer. In the Cholame Valley the alluvium is estimated at several hundred meters (Dickenson, 1966) and seismic refractions studies by Eaton (1968) indicate discontinuities at 1.4 and 6 km depth. It appears that the creep layer corresponds to the stable sliding layer expected from

laboratory results (Byerlee and Brace, 1968). And the zone characterized by earthquakes 4 to 10 km depth, is a region where displacement occurs by the mechanism of stick-slip observed by Byerlee and Brace (1968).

Although our synthesis of the mechanism of the main shock is certainly not uniquely determined, the strong self-consistency of the creep data, geodetic measurements, seismic moment, and aftershock distribution allow considerable confidence in the model. Perhaps more importantly, this model implies a generating mechanism for the creep and aftershocks that followed.

CONCLUSIONS

1) During the year subsequent to the 1966 Parkfield earthquake a maximum of at least 20 cm of total displacement occurred on a 30 km section of the San Andreas fault, which far exceeded the surficial displacement at the time of the earthquake itself. The rate of displacement decreased logarithmically during this period in a manner similar to the decrease in aftershock activity. After the initial high rate of activity, it could be seen that most of the displacement was occurring in 4 - 6 day epochs of rapid creep following local aftershocks.
2) The occurrence of the creep epochs is so regular that it can be predicted. The displacement accumulated each time is about constant and corresponds to approximately 0.1 bar stress drop.

3) Some epochs of creep appear to trigger local earthquakes, and some local earthquakes triggered creep epochs.

4) Changes in the rate of creep did not occur simultaneously along the length of the fault trace. Sections as close together as 5 km would often proceed with significantly different creep rates. The integrated history of creep, however, showed a smooth variation from a maximum near the center to near zero at either end of the surface break.

5) A comparison of surface displacements close to the fault trace with displacements at 6 km perpendicular to it, suggests that the Parkfield main shock consisted of a 30 cm dislocation confined to 4 to 10 km depth. The top 4 km responded to this event by creep.

6) During the two years following the main shock, only a minor portion of the accumulated surface displacement was contributed by aftershocks; most of it occurred as creep. The aftershocks mainly released stress at the ends of the faulted area.

7) After two years the displacements were consistent with a 30 cm dislocation over a fault ranging from 0 to 10 km depth. The stress drop was about 4 bars.

8) Several examples of an accumulation of about 10^{-4} strain were detected in the fault zone. Relaxation of this strain with the occurrence of nearby aftershocks could also be seen.

9) Surface cracking indicated that the fault had an en-echelon offset in the southern end of Cholame Valley. Displacement measurements during the first month after the main shock confirmed this, and showed that the relative motion across the surface trace died out near the end of one break and was taken up on the other branch further south.

Chapter II

SOURCE PARAMETERS OF SMALL EARTHQUAKES OBTAINED BY SEISMIC SIGNAL ANALYSIS AND FIELD OBSERVATIONS

Abstract

The source mechanism of earthquakes in the California-Nevada region was studied using surface wave analyses, surface displacement observations in the source region, magnitude determinations, accurate epicenter locations, long period portable seismographs, fault plane solutions, and S-wave analysis. Fourier analysis of surface waves from thirteen earthquakes in the Parkfield region have yielded the following relationship between seismic moment, M_o and Richter magnitude, M_L: $\log M_o = 1.4\ M_L + 17.0$, where $3 < M_L < 6$. The following relation between the surface wave envelope parameter AR and seismic moment was obtained: $\log M_o = \log AR_{300} + 20.1$. This relation was used to estimate the seismic moment of 259 additional earthquakes in the western United States. These data combined with S-wave analyses from fourteen earthquakes in the Borrego region yield the following

relationship between moment and local magnitude: $\log M_o = 1.7 M_L + 15.1$, where $1 < M_L < 6$. This relation together with the Gutenberg-Richter energy-magnitude formula suggests that the average stress multiplied by the seismic efficiency is about 7 bars for local earthquakes at Parkfield and in the Imperial Valley, about 30 bars for local earthquakes near Wheeler Ridge on the White Wolf fault, and over 100 bars for local earthquakes in the Arizona-Nevada and Laguna Salada (Baja California) regions. Field observations of displacement associated with eight Parkfield shocks, along with estimates of fault area, indicate that fault dimensions similar to the values found earlier for the Imperial earthquake are the rule rather than the exception for small earthquakes along the San Andreas fault. The revised curve for the moment versus magnitude further emphasizes that small earthquakes are not important in strain release and indicate that the zone of shear may be about 6 km in vertical extent for the Imperial Valley and even less for oceanic transform faults.

The stress drop τ is found to be related to the seismic moment by the following equation: $M_o = 10^{23} \tau^{2.86}$.

INTRODUCTION

Recent developments have greatly improved our understanding of the mechanism of shallow earthquakes in the California-Nevada region. Many of these earthquakes are strike slip and are related tectonically to the San Andreas fault system. In this study seismic moments of these earthquakes with local magnitudes between 1 and 6 have been obtained in three ways. For the larger earthquakes, spectral densities of the surface waves were obtained. For the smaller ones the S-waves were Fourier analyzed. The moments were computed by means of the theoretical results of Ben-Menahem and Harkrider (1964), Anderson and Harkrider (1968), and Brune (1970). To estimate the seismic moment for a large number of earthquakes without the time-consuming and costly process of digitizing and Fourier-analyzing waves, the parameter AR, as defined by Brune et al (1963), was used to estimate seismic moment for another 259 shocks from the western United States recorded at Pasadena.

For the eight Parkfield shocks for which spectral densities were determined by Fourier analyses, field observations allowed an estimate of the average relative displacement accompanying them. These observations were obtained in the course of the extensive study of the Parkfield 1966 earthquake sequence. In four cases

the relative displacements were recorded on strain meters straddling the surface fault trace; in three other cases repeated measurements of the displacement of the white line on Highway 46 near Cholame were used; in another case the displacement was determined by small-scale geodetic measurements. The details of these investigations are described in the first chapter. Accurate determinations of the epicenters of these eight shocks were also available. The distance from the epicenter to the locality where the surface displacement associated with a shock was observed can be considered a minimum value for the fault length of that particular event. Based on these field observations and the surface wave analyses, it has been possible to estimate roughly the fault offset, fault dimensions, stress drop, and average apparent stress.

Basic to the understanding of the mechanics of faulting is the dislocation theory of Maruyama (1963). Dislocations are related to stress drop by the results of Starr (1928), Knopoff (1958), and Keilis-Borok (1959). Aki (1966) combined these theoretical studies to interpret earthquake mechanism in a study of the Niigata earthquake and later in a study of the Parkfield earthquake (Aki, 1967). In the 1967 study Aki proposed a scaling law for seismic spectrum with a decrease in amplitude proportional to $1/\omega^2$

at frequencies higher than some characteristic frequency dependent on magnitude.

The amplitude spectrum of seismic body waves is characterized by constant amplitudes at long periods and decreasing amplitudes with decreasing periods (Figure 15). The frequency at which these two trends meet, ν_o, can be related to the source dimension on the basis of theoretical source models (e.g. Kasahara, 1957; Berckhemer and Jacob, 1968; Brune, 1970). The seismic waves represented in the flat part, point 1 of Figure 15, have wavelengths which are long compared to the source length. The seismic moment can be obtained from any spectral amplitude in this part. Most of the energy contained in the radiated waves is associated with the portion of the spectrum between point 2 and 3 in Figure 15. This and the next chapter is concerned with the ratio of spectral amplitudes in region 3 to that in region 1, Figure 15. Such a comparison yields a lower bound for the tectonic stresses causing earthquakes (Aki, 1968).

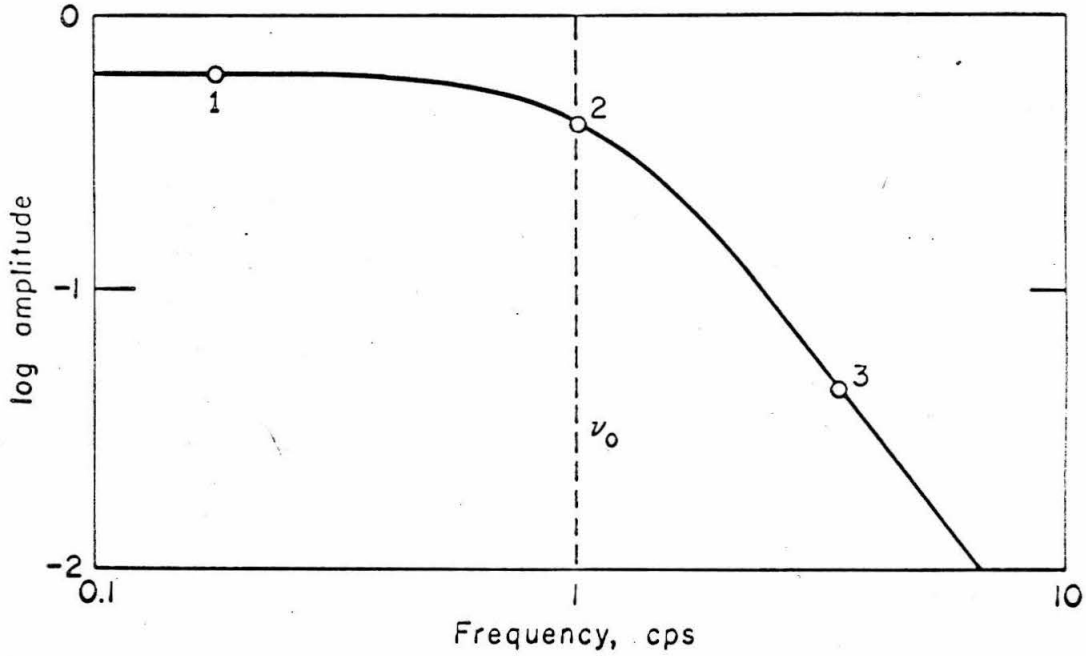

Figure 15. Theoretical seismic amplitude spectrum

The stress drop was found by Aki to be 125 bars for the Niigata earthquake and 4 bars for the Parkfield earthquake. Brune and Allen (1967a) found a stress drop of 1.1 bars for the Imperial earthquake of March 4, 1966. The fault length was about 35 km for the Parkfield earthquake and about 10 km for the Imperial earthquake. The results for the Parkfield and Imperial earthquakes indicated that previous suppositions about fault length versus magnitude and stress drop versus magnitude (Press, 1967) would have to be modified. They also indicated that a single scaling law, such as that proposed by Aki (1967), could not be valid for all regions of the earth. Tsuboi (1957) and Bath and Duda (1964) showed that Benioff's (1951a,b, 1955a) earlier assumption that earthquake volume was independent of magnitude was not valid. For large earthquakes ($M > 6$) Bath and Duda found that earthquake strain was approximately independent of magnitude in agreement with Tsuboi's hypotheses. Chinnery (1964) pointed out that the stress drops for most large earthquakes were about 100 bars and suggested that this indicated the limiting strength of the earth's crust was about 100 bars. The low stress drops found for the Parkfield and Imperial shocks suggested that the stress drop for these earthquakes was only a fraction of

the total stress, as in the stick-slip faulting mechanism of Brace and Byerlee (1966). Burridge and Knopoff (1964) gave equations relating the energy release to the ratio of the stress drop to the initial stress. Earlier, Orowan (1960) had shown that, if the final stress after rupture was equal to the frictional stress during rupture, studies of the energy of seismic wave radiation did not determine the prestress. King and Knopoff (1968a) correlated the product of fault length and the square of displacement versus magnitude and found that for earthquakes the fractional stress drop decreased with decreasing magnitude; i.e., for small magnitudes this stress drop was a small fraction of the prestress.

Burridge and Knopoff (1967) and King and Knopoff (1968b) used a model of earthquake strain release consisting of masses and springs in series. Many of the features of earthquake occurrence were explained by this model. The results for fault length, fault displacement, and stress drop found in the present study for earthquakes in the San Andreas fault system are in approximate agreement with the results from the Parkfield and Imperial earthquakes and with the fractional stress-drop curves suggested by King and Knopoff (1968a).

A STUDY OF PARKFIELD AFTERSHOCKS

Moment Versus Magnitude Curve, $3 < M < 6$

Seismic moment as a function of magnitude was first estimated by Brune (1968) in order to calculate rates of slip along major fault zones. The moments of a number of large earthquakes were estimated from field observations (Brune and Allen, 1967a). A theoretical curve based on the amplitudes of 100-sec mantle waves (Brune and King, 1967) was fitted through these data. For magnitudes less than 6 no reliable data were available for long-period waves, and as a first approximation it was assumed that the local earthquake magnitude corresponded to the surface wave magnitude. Seismic moments for only two earthquakes below magnitude 6 (Parkfield and Imperial) were available at that time. We here establish more accurately the portion of the moment-magnitude curve for $M_L < 6$. Surface waves from thirteen earthquakes in the magnitude range from 3.2 to 5.5 were Fourier-analyzed. All of them were located in the San Andreas fault region with the exception of one shock from the southern Gulf of California. The epicenters were obtained from Eaton et al (1970), McEvilly et al (1967), and Richter et al (1967). When the magnitude assigned by the latter two sources differed, the average was taken. For the surface wave analysis Press-Ewing seismograms from the Pasadena

station were used. In Table 3 the origin time, depth, and magnitude of these shocks are given. Considerations of the uncertainties in the magnitude determinations, instrumental corrections, local geologic conditions, etc., suggests that in this experiment an uncertainty of a factor of 2 in relating moment to magnitude might be expected. In the future this uncertainty can be further reduced by use of more stations close to the source. The present study has the advantage that the station used (Pasadena) is also the station originally used to define the various magnitude scales.

The equivalent double-couple seismic moment, as defined in the dislocation theory of faulting (Maruyama, 1963), was obtained from surface wave spectral density observed at Pasadena. The procedure is essentially that used by Aki (1966). The far-field displacement for a double-couple as given by Ben-Menahem and Harkrider (1964) was used to obtain moment from spectral density.

The fault plane solution for the Parkfield earthquakes was given by McEvilly et al (1967); that for the Gulf of California earthquake was given by Sykes (1968). Shocks 4 and 11 of Table 3 were assumed to have originated on the San Jacinto and Imperial faults, respectively, and the approximate direction of the fault plane for shock 3 was obtained from the CIT southern California array. The thirteen analyzed shocks are very close to vertical

strike-slip faults. All the shocks are shallow. For vertical strike-slip faults at a shallow depth, Ben-Menahem and Harkrider's expression for Love waves simplifies to:

$$M_o = (rC_L T)^{1/2} (\tilde{U}_\theta \omega / A_L \cos 2\theta) \qquad (1)$$

where r is the distance, C_L is the Love wave phase velocity, $\tilde{U}_\theta$ is the spectral density, θ is the azimuth from the strike of the fault to the station, A_L is the excitation function defined by Harkrider (1964), and $\omega = 2\pi/T$ is the angular frequency. For A_L the values for a tectonic model given by Anderson and Harkrider (1968) were used.

The surface waves of shock 8 recorded at Pasadena by 30-90 Press-Ewing instruments are shown in Figure 16. After resolving into transverse and longitudinal components, the Love waves were Fourier-analyzed. Three values for moment were obtained for each shock, using three spectral density values around the peak density ($T \approx 20$ sec). The average moments for these three determinations are given in Table 3 and are plotted as solid circles in Figure 17. Shocks 3 and 4 lie somewhat below the fitted line. Their hypocenters were deeper than the hypocenters of the other shocks, and it is not certain that their motion was strike-slip.

The double circled point at magnitude 6 (Figure 17) was

TABLE 3 Earthquake Characteristics for Parkfield and Other Areas Along the San Andreas Fault

No.	Region	Date	Time h	Time m	Time s	Depth h, km	Magnitude M	AR, mm²	Moment M_0, $\times 10^{22}$ dyne cm	Displacement $\bar{U}$, cm	Length, km	Fault Area, km²	Fault Dimensions, km	$\bar{\sigma} \cdot c$, bars	σ, bars
1	Gulf of California	May 22, 1966	07	42	42.9	0	5.5	11530	180.0	...	...			19.1	
2	Parkfield	June 29, 1966	19	53	29.5	5.1	4.9	5250	61.9	0.5	30	400	33 × 12	6.9	0.1
3	Brawley	Aug. 23, 1966	01	00	48	27	4.7	1070	8.7	...	...			24.6	
4	Brawley	May 23, 1963	09	06	04.7	25.4	4.6	694	9.5	...	...			16.0	
5	Parkfield	Aug. 12, 1967	18	57	40.4	3	4.2	215	3.4	0.2	3	56.7	16 × 3.4	11.2	0.1
6	Parkfield	Oct. 27, 1966	12	06	03.9	10.7	4.0	212	3.0	1.0	8	10.2	8 × 1.3	6.3	1.5
7	Parkfield	July 24, 1967	02	08	53.7	7	3.8	113	1.1	0.2	18	16.7	10 × 1.7	8.7	0.2
8	Parkfield	Aug. 3, 1966	12	39	05.8	2.9	3.7	86	1.0	1.0	3.5	6.7	3.5 × 2.0	6.8	1.0
9	Imperial	March 4, 1966	12	40	06.1	1.1	3.6	115	1.6	1.2	...	10	10 × 1	3.0	1.1
10	Parkfield	July 2, 1966	12	08	33.5	6.3	3.6	47	0.73	1.0	8	5	8.5 × 0.6	6.6	2
11	Hollister	April 28, 1961	14	05.9		...	3.5	37	0.45	...	...			7.6	...
12	Parkfield	Aug. 19, 1966	22	51	20.1	6.6	3.4	24	0.35	0.7	2.2	3.3	3.3 × 1	6.9	0.7
13	Parkfield	July 2, 1966	12	16	15.4	6.7	3.2	13	~0.25	0.3	...		0.5	4.8	~0.6
14	Parkfield	July 2, 1966	12	25	06.8	−1.2	3.1		<0.2	0.1	...		0.5	>4.3	~0.2

Wyss and Brune (1968)

obtained from the definition of surface wave magnitude M (Richter, 1958). According to the definition, a magnitude 6 earthquake produces a far field displacement of 100μ at a distance of 22° for surface waves of 20 sec period. From this amplitude the moment was calculated. This point thus represents the average of the numerous observations on which the surface wave magnitude was based. As pointed out by Richter (1958, p. 347), the scale was adjusted to agree with the local magnitude M_L for magnitude values of 6 to 7.

The logarithms of the moments of these thirteen earthquakes closely define the following moment-versus-magnitude relation:

$$\log M_o = 1.4\, M_L + 17.0 \qquad 3 < M_L < 6 \tag{2}$$

The slope of this line indicates that in the magnitude range $3 < M_L < 6$ the seismic efficiency η is not a rapidly varying function of magnitude. This follows from the energy-magnitude relation given by Gutenberg and Richter (1956)

$$\log E_S = a + bM \tag{3}$$

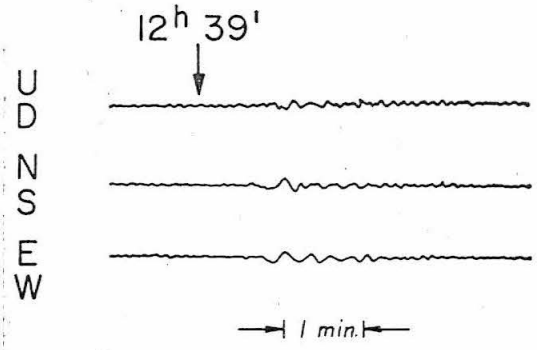

Fig. 16 Shock 8, $M = 3.7$, Parkfield, recorded by three component long-period Press-Ewing seismographs at Pasadena.

Wyss and Brune (1968)

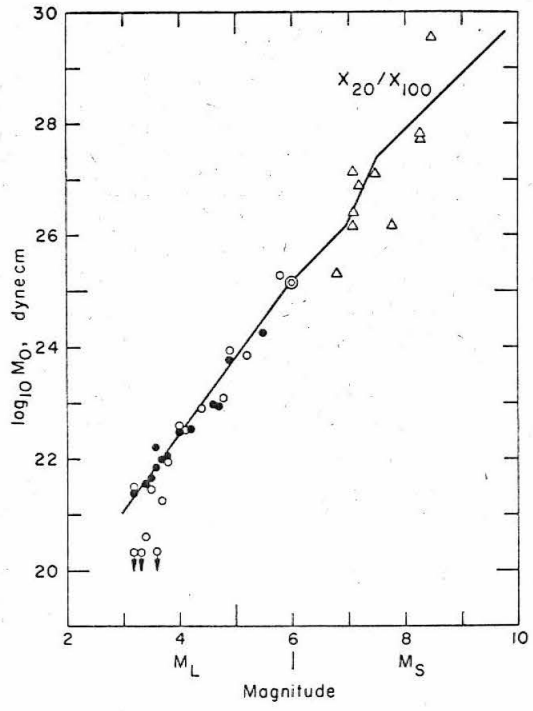

Fig. 17 Log of seismic moment as a function of magnitude for shocks along the San Andreas fault. After *Brune* [1967], modified for $M_L \leq 6$. The solid circles represent the shocks listed in Table Moments derived from the parameter AR are represented by open circles, and moments estimated from field evidence are represented by open triangles. The slope of the straight line below $M = 6$ is 1.4.

Wyss and Brune (1968)

and the relationship for work done during a dislocation

$$E = \bar{\sigma}A\bar{U} = \bar{\sigma}M_o/\mu \qquad (4)$$

In these equations E_S is the seismic energy, E is the elastic energy, M is the magnitude, $\bar{\sigma}$ is the average acting stress (average of the initial and the final stress), A is the fault plane area, $\bar{U}$ is the mean relative displacement on the fault plane associated with an earthquake, M_o is the seismic moment, and μ is the shear modulus. Let η be the seismic efficiency factor; then

$$E_S = \eta E \qquad (5)$$

Combining (3), (4), and (5) gives the magnitude as a function of moment.

$$M = \frac{1}{b} \left[\log M_o + \log (\bar{\sigma}\eta) - (\log \mu + a)\right] \qquad (6)$$

Thus b is the slope of the log moment versus magnitude curve if η is not a function of magnitude. The observed value of the slope of M_o versus magnitude is 1.4 and thus is close to the value of

$b = 1.5$ for the Gutenberg-Richter relation, suggesting that η is not critically dependent on magnitude in the small range of magnitudes considered here. Using the Gutenberg-Richter energy relation

$$\log E_S = 1.5M + 11.8 \qquad (7)$$

letting $\mu = 3 \times 10^{11}$, we can solve equation 6 for the product of the average stress and efficiency, $\overline{\sigma\eta}$. For the nine Parkfield shocks in Table 3 the result is

$$\overline{\sigma\eta} = 7.3 \pm 1.8 \text{ bar} \qquad (8)$$

The error is the mean deviation for the nine analyzed shocks. Equation 6 suggests that the deviations from a single moment versus magnitude relation can reflect, among other things, local differences in the average stress.

Data from Other Regions Based on AR

In a paper by Brune et al (1963) the parameter AR, the sum of the area of the envelopes of the surface waves on three component

long-period Press-Ewing instruments, was used as a measure of the long-period waves. AR is approximately proportional to spectral density and thus to seismic moment. If the relation of AR to moment is established, one can approximately convert AR (mm^2) into spectral density and thus into seismic moment. The relationship was established by determining AR for the thirteen analyzed shocks and plotting these values against seismic moment. The result is shown in Figure 18. This relation is valid for shocks not exceeding depths of about 20 km. As expected, the points fall closely along a straight line with a slope of 1. The conversion equation is

$$\log M_o = \log AR_{300} + 20.1 \qquad (9)$$

where AR_{300} is the sum of the surface wave envelope areas normalized to a source distance of 300 km.

This equation was used to obtain the seismic moments for seventy-seven shocks whose AR values at Pasadena were determined by Brune et al (1963) as well as for 182 additional shocks. The results are shown in Figure 19. Shocks from the San Andreas and San Jacinto faults and from the Imperial Valley and Gulf of California

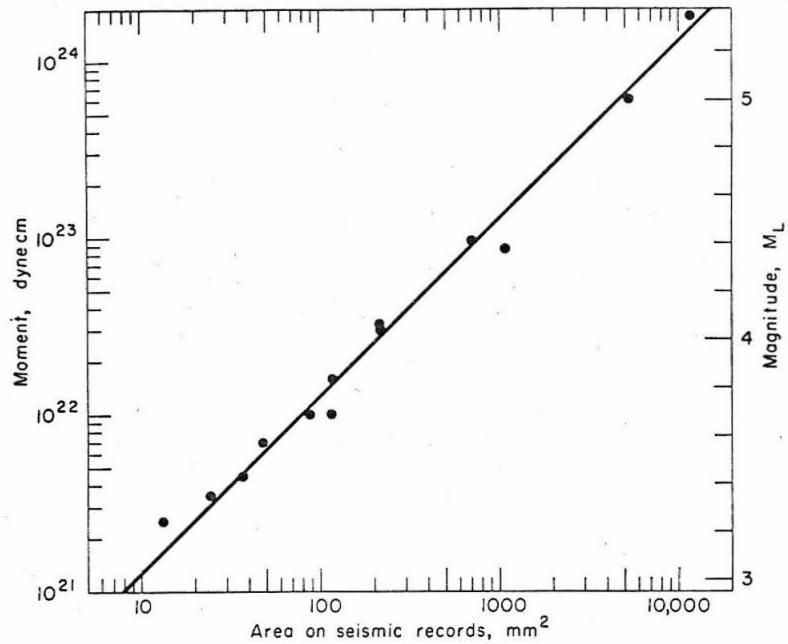

Fig. 18 Moment as a function of surface wave envelope area AR corrected to a distance of 300 km. The data points are derived from the shocks listed in Table 3 This curve can be used to approximately convert AR into moment.

Wyss and Brune (1968)

are shown as solid circles. Squares represent shocks from off the coast of California; open circles represent shocks from Nevada, Arizona, Utah, Baja California, and northern California. For these earthquakes the fault plane orientations are not known and the depth is uncertain. The scatter is considerable. As pointed out in Brune et al (1963), however, a grouping of shocks

for various regions can be observed. The Gulf of California shocks give moments that are somewhat smaller on the average than the San Andreas values, but, since they are not much different, the same symbol was used. The shocks from off the coast of northern California have higher M_o values than shocks of the same magnitude from the San Andreas. This difference may in part be due to a strong filtering of short-period body waves at the continental margin, which could make the body wave magnitude smaller. The Nevada-Arizona as well as the Baja California earthquakes fall below the San Andreas values. If it is assumed that these regional differences in surface wave excitation are due to regional differences in stress, we can solve for $\overline{\sigma\eta}$ by fitting a line with a slope of 1.4 through the data for each region. This yields a value of $\overline{\sigma\eta}$ of about 110 bars for the Laguna Salada (Baja California) and California Nevada earthquakes. The regional variations observed here could also be due to path effects, depth of source, and variations in faulting mechanism. However, the surface wave paths for all analyzed earthquakes are short ($\Delta \leq 1000$ km) and similar. All events were shallow, most of them not exceeding 16 km depth. The AR method of determining the seismic moment, adding Rayleigh and Love wave envelopes, averages out the

differences caused by different faulting mechanisms. Therefore, it is very likely that the regional variations in seismic moment are in part due to variations in tectonic stress. The relative low stresses along certain sections of the San Andreas fault may in part be caused by geologic and tectonic features that control the amount of stress the crust can withstand (Allen, 1968).

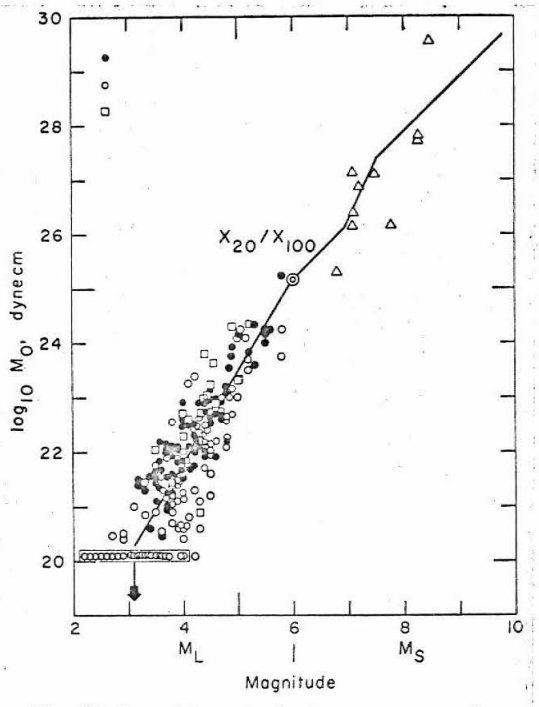

Fig. 19 Logarithm of seismic moment as a function of magnitude with data from the westernmost part of the United States. The slope of the straight line through the data is 1.7. Solid circles indicate San Andreas fault system; open circles, western United States; squares, region off the coast of California.

Wyss and Brune (1968)

The straight line that was fitted through all the available data for moment versus magnitude for the western United States

(Figure 19) gives the equation

$$\log M_o = 1.7\, M_L + 15.1 \qquad 3 < M_L < 6 \qquad (10)$$

Relationships between M_L and M_S

Since the surface wave magnitude M_S is based on the amplitude of 20 sec surface waves, we can get the relationship between surface wave magnitude M_S and local earthquake magnitude M_L from the straight lines shown in Figures 17 and 19. These relationships are

Western United States

$$M_S = 1.7\, M_L - 4.1 \qquad 3 < M_L < 6 \qquad (11a)$$

Parkfield

$$M_S = 1.4\, M_L - 2.2 \qquad 3 < M_L < 6 \qquad (11b)$$

and are valid for very shallow earthquakes. These equations are in qualitative agreement with the statements given by Richter (1958, p. 347). He indicates that, although the local earthquake magnitude and the surface wave magnitudes were originally constructed to be in agreement between magnitudes 6 and 7, later investigations

indicated that for lower magnitudes the surface wave magnitudes are smaller than the local magnitude, in agreement with equations 11.

Field Observations of Fault Displacement

For the nine shocks that occurred in the Parkfield region, fault slip was measured in the field. The approximate average slip is given in Table 3. The detailed nature of the field evidence for each shock is given below.

For shock 2 (M = 4.9) the offset of the white line on Highway 46 near Cholame (Figure 20) was measured repeatedly after the Parkfield earthquake of 20 June 1966. On 29 June it was measured at 14 h 00m, 17h, and 20h 00m GMT. In the 3-hour time interval, whose end preceded shock 2 by about 3 hours, no displacement was observed within the accuracy of measurement. In the 3 hour time interval that contained the earthquake and terminated about 7 min after the shock, 0.5 cm of displacement was observed (Figure 21). Three subsequent measurements showed no further displacement. From this evidence we may conclude that the offset of 0.5 cm that occurred between 12h 00m and 20h 00m GMT was associated with the earthquake that occurred at 19h 53m 29.5s GMT north of Parkfield. The location of the epicenter lies 30 km northwest along the San Andreas fault from the place where the

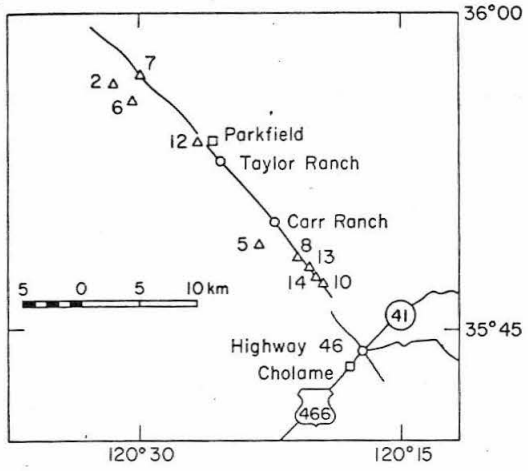

Fig. 20 Map of the Parkfield region. The surface break connected with the Parkfield earthquake of 1966 is shown as a solid line. Surface observations concerning fault slip were obtained at the Taylor ranch, the Carr ranch, and Highway 46. Epicenters of shocks for which surface displacement was observed are marked by triangles and numbered according to Table

Wyss and Brune (1968)

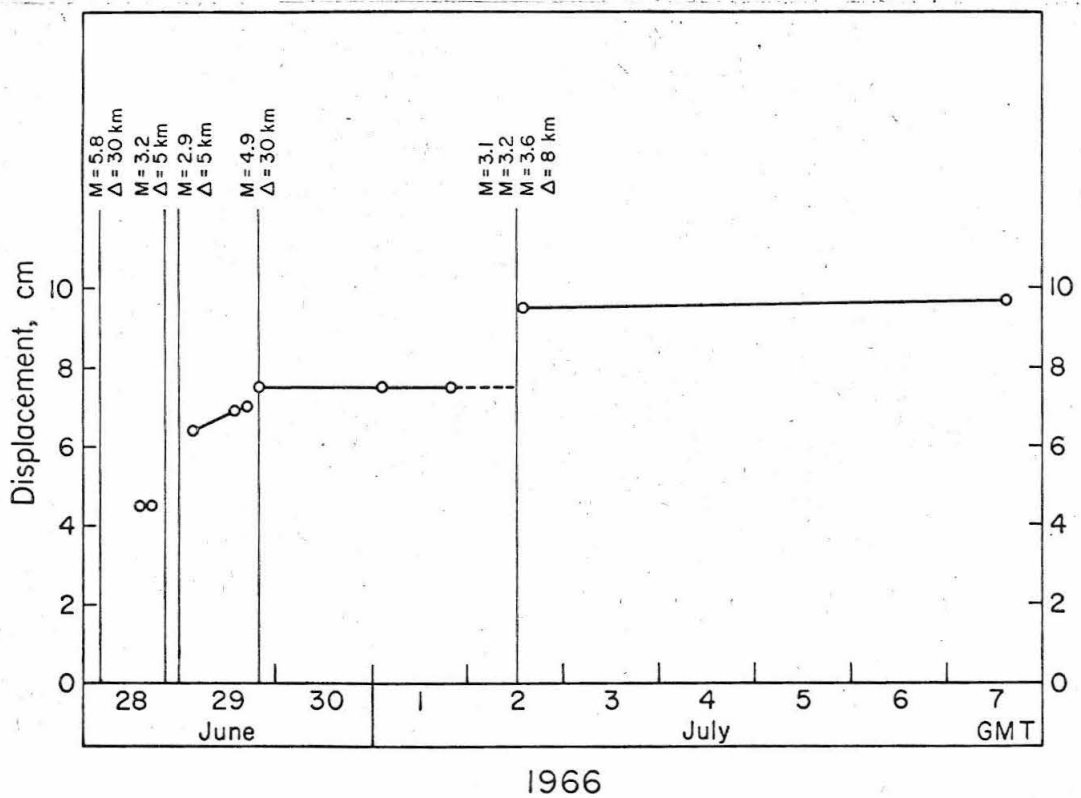

Fig. 21 Evidence for fault slip. The displacement of the white line at Highway 46 following the Parkfield earthquake on June 28, 1966, is compared with the occurrence of aftershocks. Shock 2 is believed to have caused a slip of 0.5 cm on June 29. Shocks 10, 13, and 14 are believed to have caused a slip of 1.5 cm on July 2.

Wyss and Brune (1968)

displacement was observed. Therefore it may be suggested that this shock had a fault length of at least 30 km.

For shocks 5 and 7 (M = 4.2 and 3.8, respectively) creep was measured subsequent to its occurrence by an Invar wire strain meter installed across the fault at the Carr Ranch (see Chapter I). It is assumed here that the creep periods following the two shocks (Figure 5) are causally related to them, and reflect approximately their dislocations. Despite what was said in the first chapter, it is felt that the assumption is justified, especially for shock 5. These two earthquakes are associated with the only two creep periods in Figure 11 that were irregular. In particular, the second period started at a time when, according to the displacement, log time curve, the locality was not loaded enough to overcome the frictional strength of the fault zone.

Surface displacements recorded by the quartz strain meter may have been related to shocks 8 and 12. The two creep periods in question did not have the standard displacement of 0.2 cm (see Chapter I), but 1.0 and 0.7 cm. This circumstance may be taken as suggesting that there was a causal relationship between the earthquakes and the displacements (Figure 22).

Shocks 10, 13, and 14 occurred in short sequence close to each other with epicenters 8 km north of Highway 46. The white line at Highway 46 showed no displacement for a 2-day period ending at

20h 00m on 1 July. The shocks 10, 13, and 14 occurred at 12h 09m, 12h 16m, and 12h 25m on 2 July. The first measurement afterward was taken at 14h 00m on 2 July and revelaed an added displacement of 1.5 cm (Figure 21).

Shock 6 seems to have been responsible for a displacement of about 1 cm at the Taylor Ranch. The cumulative displacement at this locality preceding the time of earthquake 6 followed a logarithmic curve given by the equation

$$U = 9.4 \log t - 4.5 \qquad (12)$$

where U is cumulative relative displacement in centimeters and t is time in days (Figure 23). The displacement of about 1 cm on 3 November 1966, was followed by a period of no displacement up to 22 November. After this date the displacement values continued to follow the same logarithmic curve as before. Shock 6 on 27 October was located at a distance of 8 km to the northwest of the Taylor ranch. In the same interval of time between geodetic measurements three shocks of magnitude 2 to 2.3 occurred (McEvilly et al, 1967).

It is concluded from the above evidence that as a first approximation it may be assumed that the surface displacements

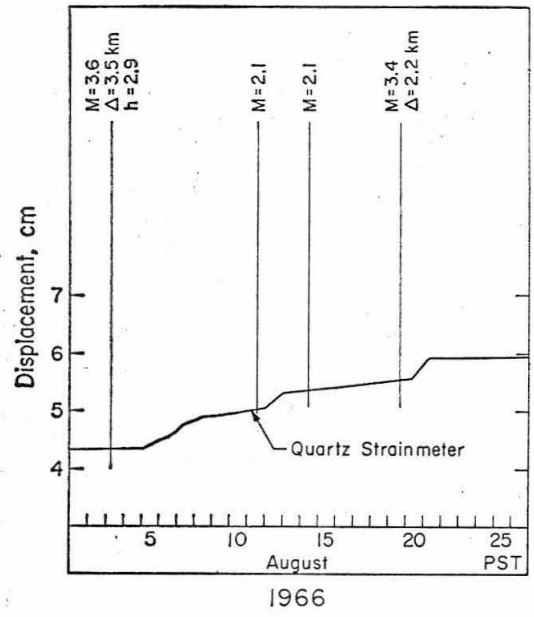

Fig. 22 Creep evidence obtained by the quartz strain meter at the Carr ranch [*Smith and Wyss*, 1968]. Shocks 8 and 12 are believed to be connected with 1.0- and 0.7-cm surface displacement on August 3 and August 19, respectively.

Wyss and Brune (1968)

(including creep) associated with each earthquake are representative of the displacements that occurred at depth during the respective earthquakes.

Source Dimensions

For the nine shocks that occurred in the Parkfield area field evidence for approximate relative displacement was listed above. For the same shocks the seismic moment was obtained from surface wave analysis and equation 1. The fault area was obtained from the

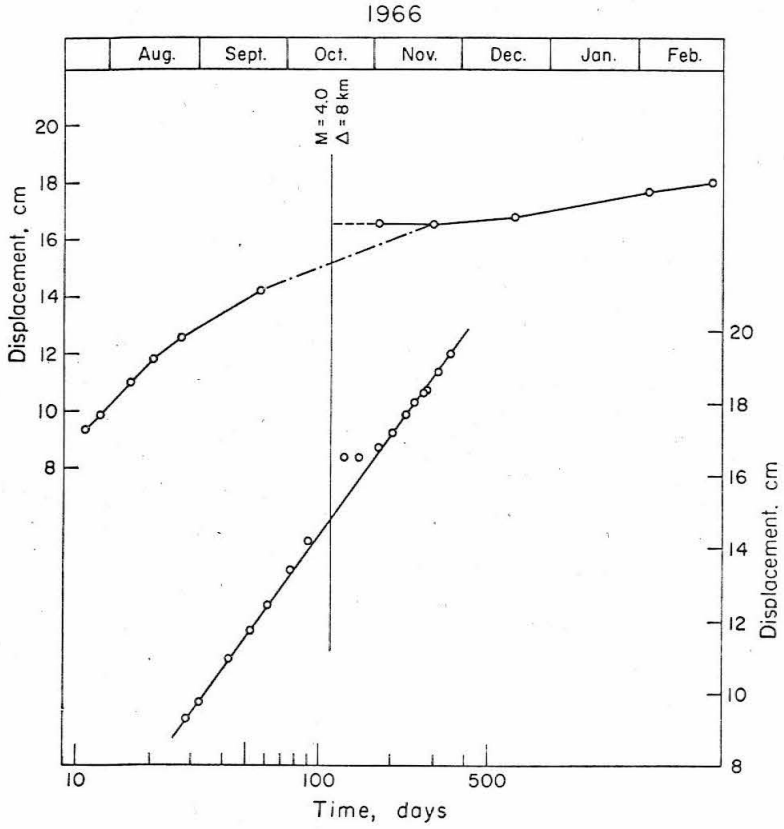

Fig. 23 Displacement evidence obtained by small-scale geodetic observations at the Taylor ranch [*Smith and Wyss*, 1968]. The upper curve represents displacement as a function of time; the lower one, the same displacement as a function of log time. The displacement connected with shock 6 is estimated to be about 1 cm.

Wyss and Brune (1968)

equation

$$M_o = \mu A \bar{U} \qquad (13)$$

The values are given in Table 3. A value of 3×10^{11} dynes/cm^2 was assumed for μ except for the very shallow shocks 9, 10, 12, 13, and 14, for which a value of 1.5×10^{11} dynes/cm^2 was assumed. Where the field evidence also yielded an estimate for the fault length and fault width, a check on the above estimate of area was provided.

The epicentral distances to the points where the respective displacements were observed are listed in Table 3 as fault length. Regarding this value as a minimal fault length, and the assigned depth as a minimal fault width for the cases of surface rupture, dimensions consistent with the fault area computed from the moment and surface offset are proposed and also given in Table 3. The locations of shocks 2, 5, 6, and 7 were obtained from McEvilly et al (1967); the locations of shocks 8, 10, 13, and 14, from Eaton et al (1970); the location for shock 12 was taken from the Pasadena Local Bulletin (Richter et al, 1967). During the months following the Parkfield earthquake, a number of portable seismic stations were operated in the area; hence, the epicenters for this period were determined very accurately. The source dimensions derived from surface wave analyses and measurements of ground displacement in the field are consistent with the fault lengths estimated from the epicentral distances to the sites of measurement. These results strongly suggest that the proposed source dimensions are approximately correct.

The fault lengths as proposed in Table 3 were compared with the magnitude versus length plot by Press (1967). The results are shown in Figure 24 as open triangles. These values are interesting

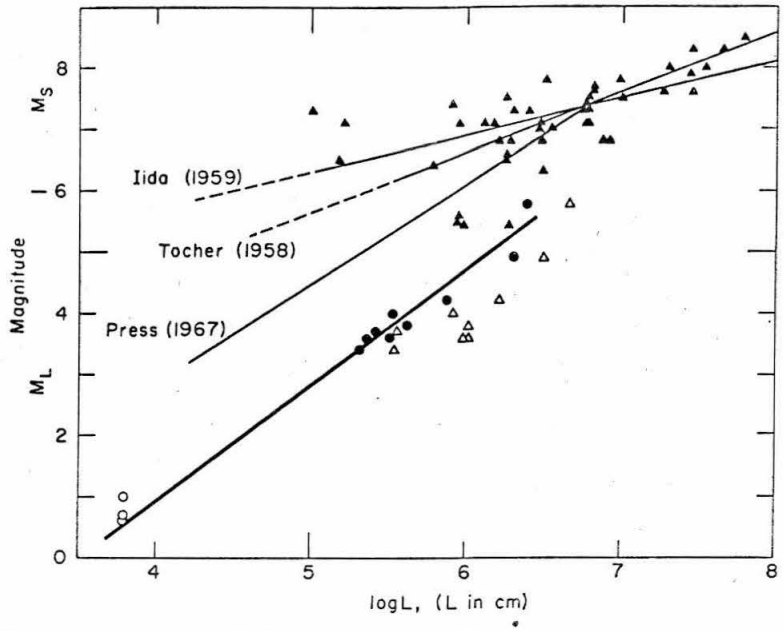

Fig. 24 Observations of fault length plotted as a function of magnitude. For each of nine earthquakes, including the Parkfield mainshock, two points are plotted. The open triangles represent fault lengths estimated from field evidence, and the solid circles represent $(A)^{1/2}$ determined from seismic wave analysis and field observations of fault offset. The values for micro-earthquake fault dimensions (open circles) are taken from *Smith et al.* [1967]. The solid triangles represent fault lengths taken from [*King and Knopoff*, 1968a].

Wyss and Brune (1968)

for the geologist since they approximate actual surface rupture length. They may also be compared with other data obtained by field evidence (solid triangles) taken from King and Knopoff (1968a).

If the square root of the fault plane area (solid circles) is plotted rather than the fault length, the following approximate relation is found:

$$M = 1.9 \log A^{1/2} - 6.7 \qquad (14)$$

Substituting equation 7 into equation 14, we obtain

$$E_S = 55 \times A^{1.43} = 55 \times L^{2.86} \qquad (15)$$

This relation indicates that seismic energy for the presented shocks between magnitude 3 and 6 is approximately proportional to the cube of the fault dimension. Later a more detailed analysis of earthquakes in the Borrego area will show that this relation does not hold for smaller events. The straight line fitted by Tocher (1958) through the field observations of surface rupture of large earthquakes suggested a second-power dependence of the elastic energy on fault length. Press's (1967) curve for shocks smaller than about magnitude 7 was constructed with a third-power dependence of elastic energy on source dimension. Our data are in accordance with the results of Smith et al (1967) for earthquakes of the magnitude range of about 1 (open circles in Figure 24).

From Figure 24 it is evident that all the Parkfield earthquakes have source dimensions at least an order of magnitude larger than predicted by Press's curve. Thus it appears that for small earthquakes along the San Andreas fault large source dimensions such as those found by Brune and Allen (1967a) for the Imperial earthquake are quite common. An increase of stress drop, average stress, or efficiency, keeping the source dimension constant, would increase the corresponding magnitude. Thus, Press's curve would

apply to earthquakes of greater stress drop, greater average stress, or better efficiency. For very large earthquakes, all these conditions probably apply. Regional variations in surface wave excitation mentioned earlier suggest that in some areas the stresses may be high enough to bring the values of source dimension into agreement with Press's curve.

Stress Drop

Stress drops for the Parkfield shocks were estimated using the following formula, which applies to an infinitely long vertical surface fault with strike-slip displacement (Knopoff, 1958):

$$\tau = \frac{1}{2} U_m \mu / W \qquad (16)$$

where $U_m = (4/3)\ \overline{U}$ is the maximum relative displacement and W is the fault width (depth). The values are given in Table 3. Since the field observations of displacement may not accurately reflect the average displacement, the values for the stress drops should be regarded only as order of magnitude determinations. The average stress drop is approximately 1 bar.

Comparison of Excitation of Surface Waves by Earthquakes and Underground Nuclear Explosions

The excitation of surface waves by earthquakes of $3 < M_L < 5$ along the San Andreas fault has been found in this study to be much greater than for NTS explosions of equivalent magnitude. These data are in agreement with the earlier results of Brune et al (1963). In the earlier study it was possible only to speculate that this was the result of larger source dimensions for eathquakes, but it is now evident that this is indeed the case. Field studies of the Parkfield earthquake and its aftershocks and of the Imperial earthquake have conclusively demonstrated that these earthquakes have much greater source dimensions than previously surmised by Press (1967) and have much greater source dimension than equivalent magnitude explosions. This conclusion is apparently valid for magnitudes at least as low as 3.0 and is thus very important in any consideration of extending the nuclear test ban treaty to underground explosions of low magnitude. It must be cautioned, however, that many earthquakes in the Laguna Salada and Nevada-Arizona regions apparently have much smaller source dimensions and indeed may have source dimensions of the same order as surmised by Press.

Calculated Rates of Slip Along Major Fault Zones

Brune (1968) calculated the rates of slip along major fault zones by summing the moments for earthquakes in these zones. Modification of the moment versus magnitude curve for $3 < M_L < 6$, according to equation 2, will reduce the calculated rates of slip for the zones in which local magnitudes M_L were used, i.e. in the California region where local magnitudes were used for magnitudes as low as 3.0. For other regions either the surface wave magnitude or the body wave magnitude was used, and thus it is not obvious that any correction is necessary. The correction will be most important on zones that did not have large earthquakes.

In the Imperial Valley of California, the calculated rate of slip is reduced from 3.2 to 2.2 cm/yr, and the depth of the shear zone necessary to balance the geodetically observed shear rate of 8 cm/yr, is reduced from about 8 to about 6 km. The calculated rate of slip for the Kern County, California, region is only slightly reduced, from 17 to 16 cm/yr, and the calculated rate of slip along the San Andreas fault since 1800 is reduced from 6.6 to 6.1 cm/yr.

Regional Variations of Stress

The AR method gives an approximate estimate for the moment, based on the excitation of long-period waves and the magnitude (short-period waves) probably gives an even less accurate estimate for the energy. The differences in the ratio of long- to short-period waves are so large for different earthquakes, however, that even approximate methods can give quite a good picture of differences in apparent stress. In Figures 25 and 26 the differences between seismograms are so strong that there can be no doubt that there must exist a large difference in source parameters, e.g., fault length, stress, or stress drop. It is also possible that such differences could, in many cases, be a function of hypocentral depth. Great depth will decrease the relative excitation of fundamental mode surface waves (Tasi, 1969) or stress may be a strong function of depth in all regions. This ambiguity can be resolved with data that allow an accurate correlation with depth. If we compare the average (from numerous earthquakes) apparent stress of one region with that of another, we are probably comparing apparent stresses for an average depth.

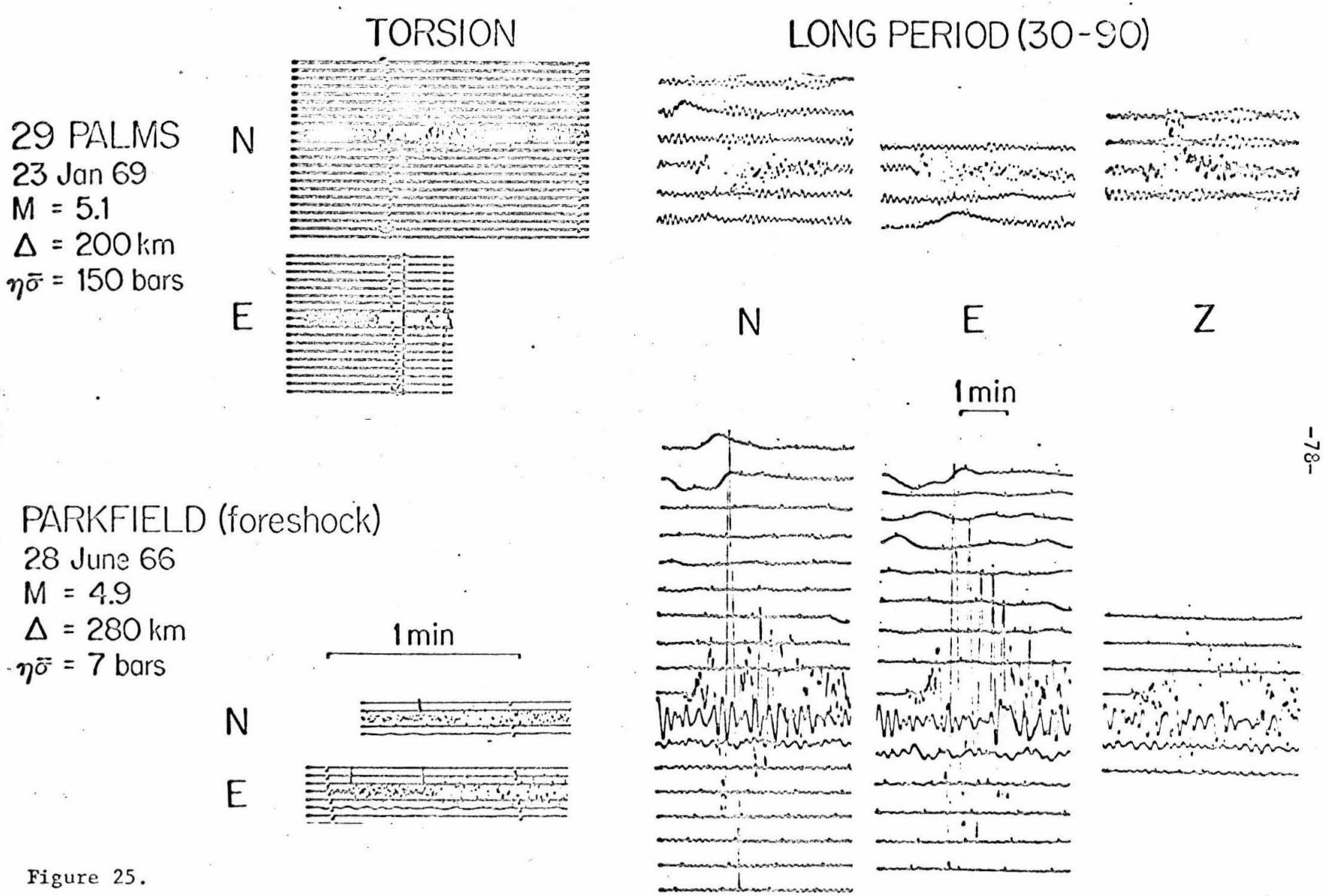
TORSION
LONG PERIOD (30-90)
29 PALMS
23 Jan 69
M = 5.1
Δ = 200 km
ησ̄ = 150 bars
N
E
N
E
Z
1 min
PARKFIELD (foreshock)
28 June 66
M = 4.9
Δ = 280 km
ησ̄ = 7 bars
1 min
N
E

Figure 25.

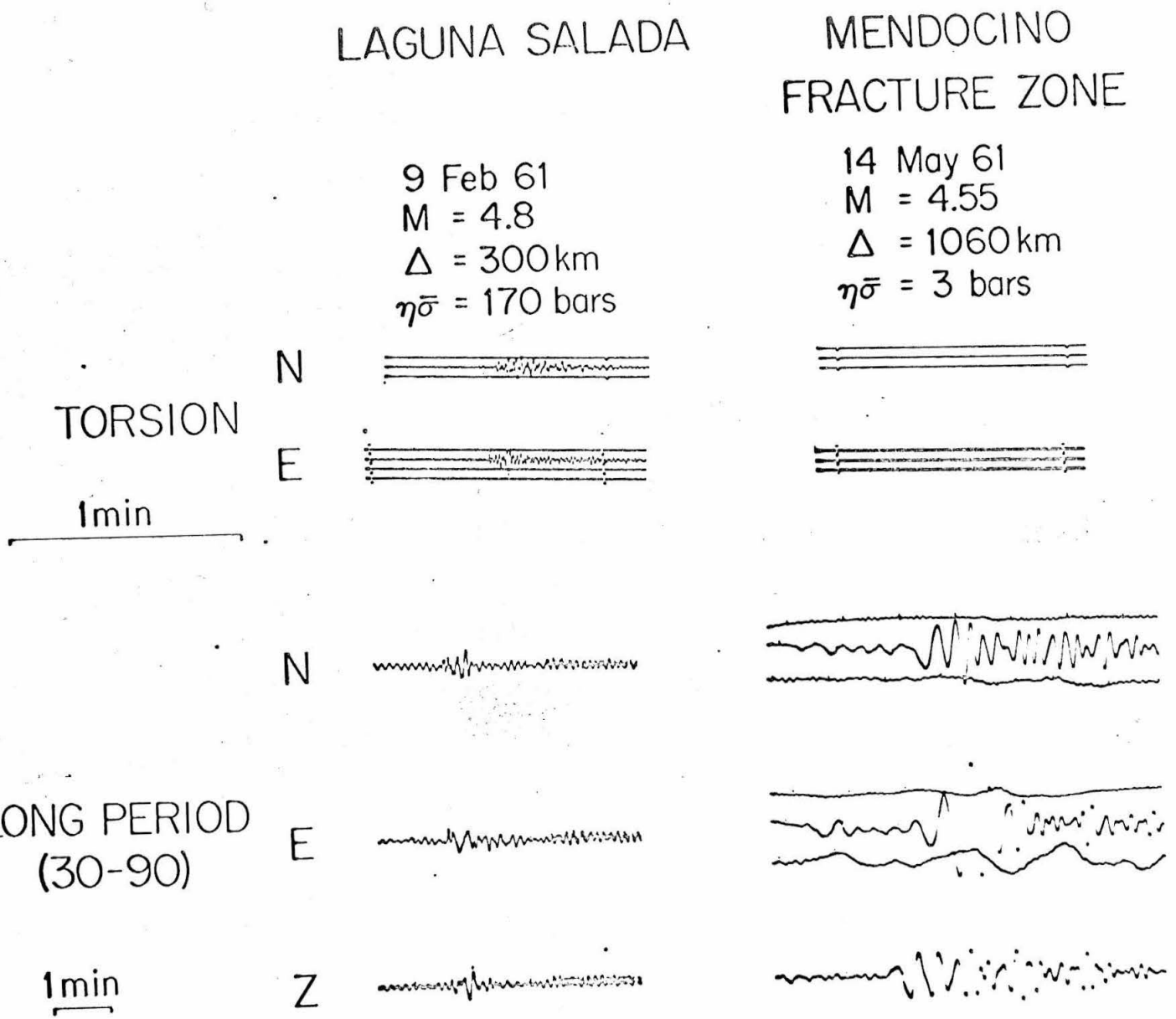
LAGUNA SALADA
MENDOCINO FRACTURE ZONE
9 Feb 61
M = 4.8
Δ = 300 km
ησ̄ = 170 bars
14 May 61
M = 4.55
Δ = 1060 km
ησ̄ = 3 bars
TORSION
N
E
1 min
N
LONG PERIOD (30-90)
E
1 min
Z

Figure 26.

Before regional variations in apparent stress are discussed, it is desirable to get a feeling for how much the depth might effect the results for apparent stress. First, we will ask the questions: Are there ever shallow shocks with relatively high apparent stresses, and are there ever deeper shocks with small apparent stresses in Southern California? Only shocks well within the CIT network were considered in this search. Table 4 gives eight earthquakes with hypocenters at depth greater than 10 km and apparent stresses smaller than 25 bars. Table 5 gives eight events with depth smaller than 6 km and apparent stresses larger than 35 bars (in most cases, larger than 100 bars). These tables support the hypothesis that there is a factor other than depth influencing the apparent stress. It is proposed that this additional factor is the stress in the source region.

The Parkfield and the Borrego Mountain aftershocks sequences provide the best data available to date for a comparison of two source regions. For both earthquake sequences accurate locations were obtained using portable seismographs. The inaccuracy of the depths assigned on the basis of field recordings is probably less than 2 km (Hamilton, 1970). In Figure 27 the apparent stresses for the larger earthquakes of the two sequences are plotted versus depth. Small and open symbols indicate events whose depths were based on the CIT network readings only. The large and full symbols mark

Table 4

"Deep" Local Earthquakes with Low Stresses

Region	d	m	y	M_L	Depth [km]	$\overline{\sigma\eta}$
Brawley	23	08	66	4.7	27.	24.6
Brawley	23	05	63	4.6	25.4	16.0
Torrance	08	05	63	2.7	17.1	7.1
Frazier Mt.	01	03	63	5.0	13.9	21.
Borrego Mt.	13	01	63	4.2	13.0	4.7
Trifuno Pass	21	06	63	3.7	13.1	8.1
29 Palms	18	07	63	3.9	11.6	19.
29 Palms	19	07	63	3.6	14.2	14.

In Table 4 and 5 the quality of hypocentre locations given in the Pasadena Bulletin is B with two exceptions. A comparison of six hypocentre locations by Pasadena with the more accurate ones by Hamilton (1970) indicates that Pasadena quality B locations give meaningful depths and differ by 2 km from the locations based on the field stations (Hamilton, 1970).

Table 5

Shallow Local Earthquakes with High Stresses

Region	d	m	y	M_L	Depth [km]	$\bar{\sigma}\eta$
San Gorgonio	14	02	65	3.5	-1.8	>380.
Rabbit Peak	07	01	66	4.0	-1.7	37.
29 Palms	22	08	63	4.4	5.8	152.
Catalina	25	09	63	3.8	-0.5	40.
Morrongo	10	12	63	3.7	3.4	676.
Warner Springs	22	05	64	3.8	5.5	120.
Woody	31	05	64	3.7	6.1	>676.
Kettleman Plains	18	11	64	4.0	5.0	107.

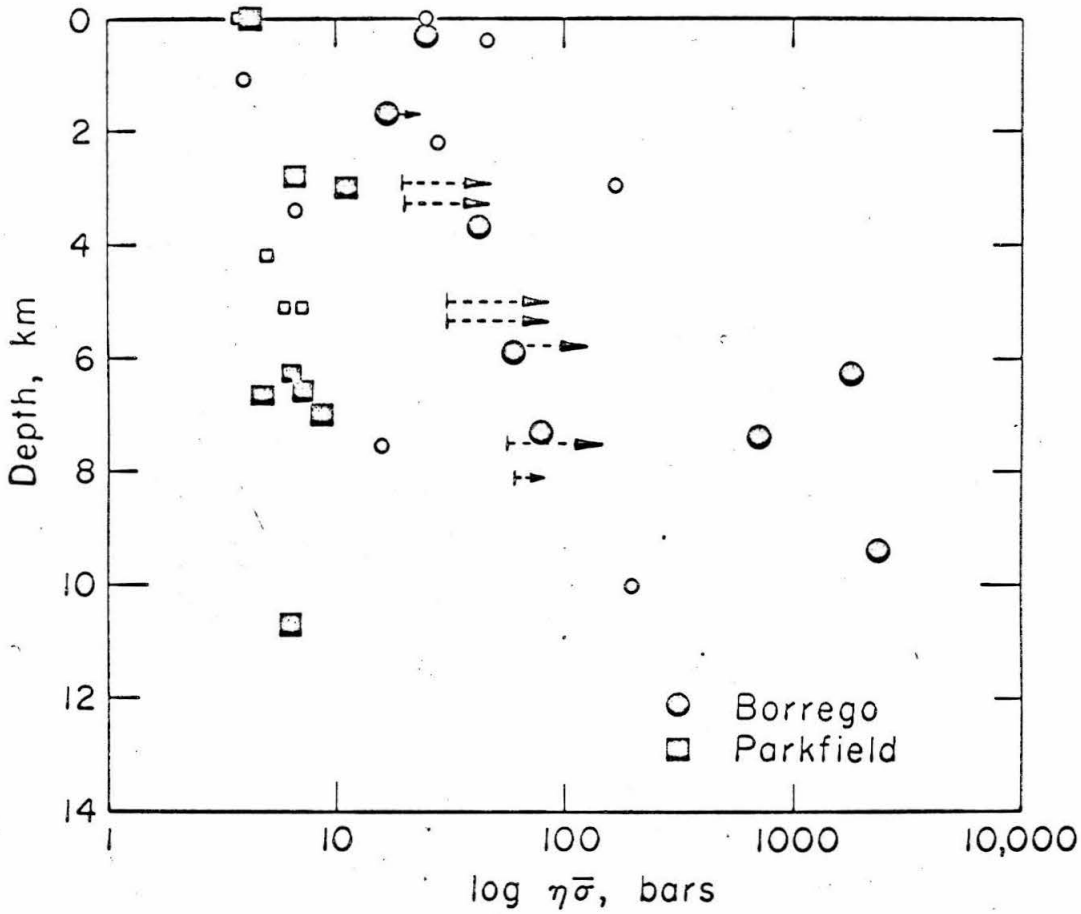

Figure 27. Comparison of apparent stresses as a function of depth in the Parkfield and the Borrego region.

events with depth assigned by the USGS, based on field arrays. Arrows indicate minimum estimates. From Figure 27 it becomes clear that (a) the apparent stress level in the Borrego region is consistently higher than in the Parkfield region, and (b) the dependence of apparent stress versus depth is different in the two regions. The Parkfield data indicate no dependence of apparent stress on depth; whereas, the Borrego data indicate an increase with depth.

The two largest values in Figure 27 are approximately equal to the hydrostatic pressure at their hypocentral depths. These two earthquakes are located more than 3 km from the surface fault trace. The third largest apparent stress value was derived from a shock 2 km distant from the surface fault trace. The fourth largest full circle value was obtained from an earthquake whose epicenter falls directly on the surface fault trace. This observation suggests that the strength of a developed fault zone is considerably lower than the strength of the surrounding bedrock. In Parkfield all the hypocenters lie on the fault surface (Eaton et al, 1970).

In Figure 28 the seismic signatures of two earthquakes from the two regions are compared. The Borrego event shows larger short-period, but smaller long-period waves in comparison with the almost equidistant Parkfield event.

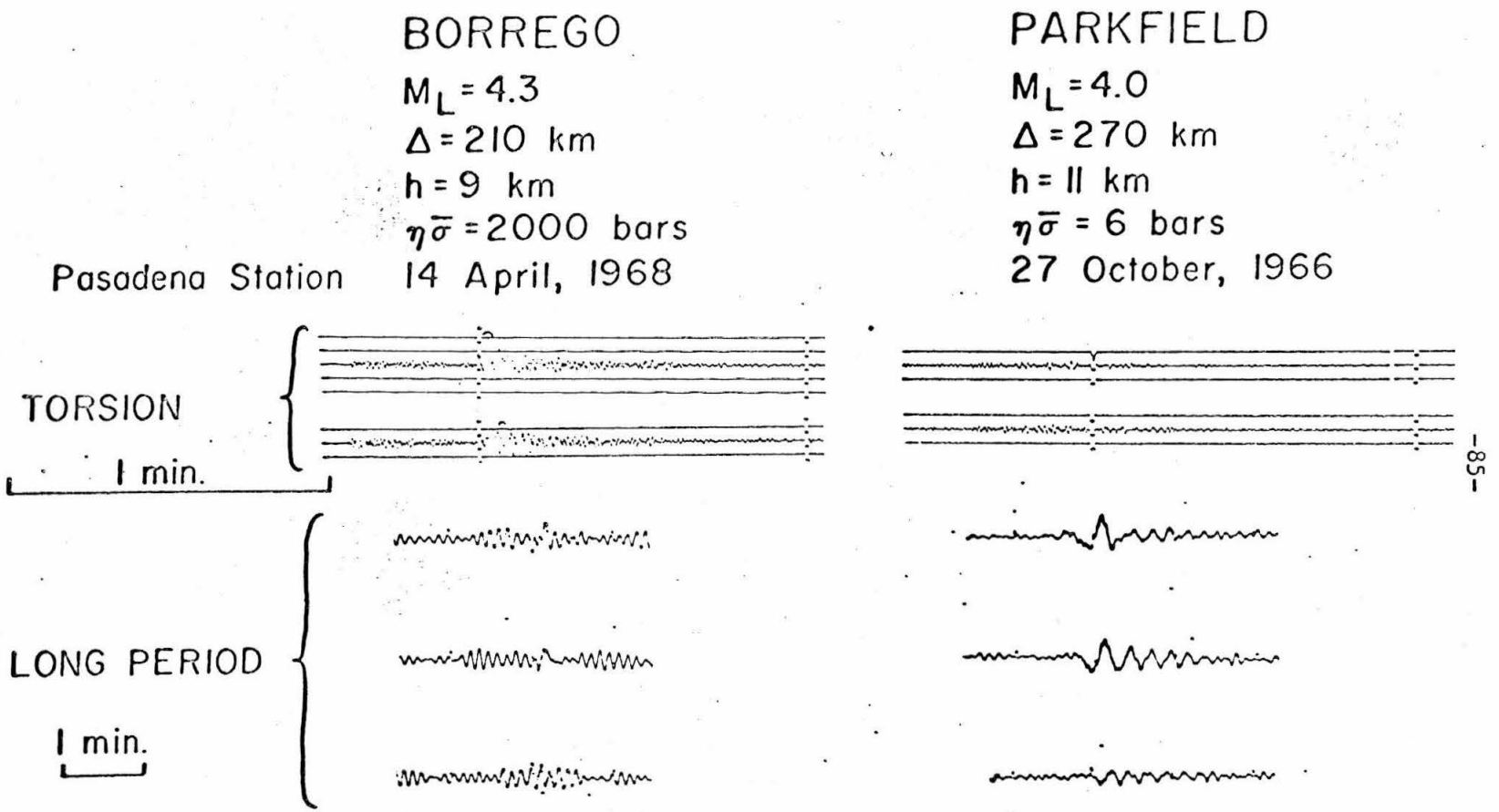

Figure 28. Comparison of an earthquake located near Parkfield with one near Borrego Mountain.

It is felt that an explicit expression for apparent stress versus depth is not justified by the data presented in Figure 27. We may say, however, that in the Borrego region the apparent stress at a depth of 10 km is about 10 times larger than that close to the surface. This result makes sense, because the hydrostatic pressure increases the frictional strength with depth. The Parkfield behavior on the other hand seems anomalous. The lack of strength increase with depth could be explained by the presence of serpentinite in the Parkfield source region. It is possible that in this region the dehydration process of serpentinite demonstrated in the laboratory by Raleigh and Paterson (1965), decreases the frictional strength.

Now that we have demonstrated that real stress differences between regions can be detected, we turn to a broad scale study of regional differences in apparent stress. Figure 29 is a map of the apparent stresses in the Western United States. The moments of 90% of these data were obtained by the AR method. The energy estimate is, in all cases, based on the local magnitude.

In this figure the average apparent stresses of various regions are given in bars. The number of earthquakes represented by the average is given below the stress value in parentheses. Along the major fault zones the apparent stresses are generally low. The most seismically active portions of the San Andreas system have

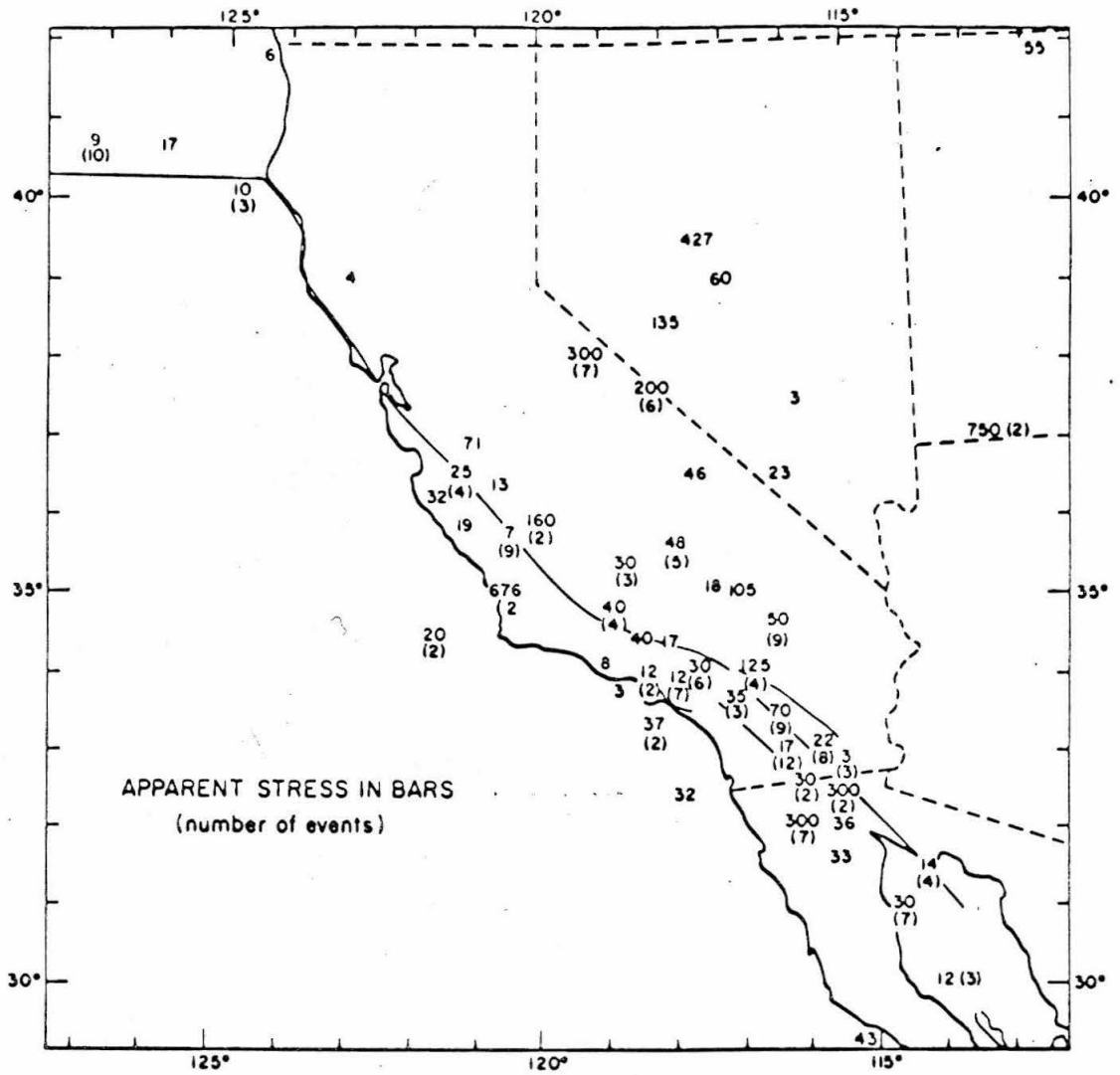

Figure 29. Map of the apparent stresses in the western United States.

the lowest apparent stresses. Higher values are connected with seismically quieter regions, e.g., Frazier Peak and San Gorgonio Pass. Conspicuously high averages are measured along the Nevada-California boarder, and in the Laguna Salada region. These high values probably reflect both greater average depth and greater strength of the source material than is found along the well developed San Andreas fault system.

A STUDY OF BORREGO MOUNTAIN AFTERSHOCKS

Setting of the Experiment

The Borrego Mountain, California, earthquake of April 9, 1968, was associated with a 35 km surface fracture and was followed by a large number of aftershocks. An ad hoc field party of the California Institute of Technology, was joined by geologists and geophysicists of the U. S. Geological Survey, Menlo Park (Allen et al, 1968).

The effects of this earthquake were documented and analyzed in even greater detail than were the effects of the Parkfield earthquake.

The USGS operated up to 25 transportable seismographs in the source area. This extensive coverage made it possible to locate aftershocks along the entire fault length with great accuracy. Many well defined focal plane solutions were also obtained (Hamilton, 1970).

The experience with Parkfield aftershocks and the prospect of good hypocenter determinations by the USGS prompted J. N. Brune to set up a long-period experiment in the source region. Horizontal penduli were installed on outcropping granite on either side of the fault trace at distances of about 3 km (triangles in Figure 33). The direction of recording was chosen parallel to the fault. The instrument response is given as curve 1 in Figure 30. The peak magnification was varied between 1.2×10^7 and 1.2×10^4. Another type of horizontal instrument, a low-gain "jerk-meter," was also operated at station Squaw Peak (Figure 33). The response of this instrument is given by curve 2 in Figure 30. The long-period penduli recorded on tape; the jerk-meter recorded on film. Figures 31 and 32 show examples of earthquakes recorded by the long-period penduli and the jerk-meter.

The purpose of the experiment was to estimate as many as possible of the following source parameters for very small earthquakes: moment, energy, fault dimension, dislocation, apparent stress, and stress drop. It was attempted to derive all of these parameters from a S-wave analysis in the frequency range of 0.5 to 20 cps.

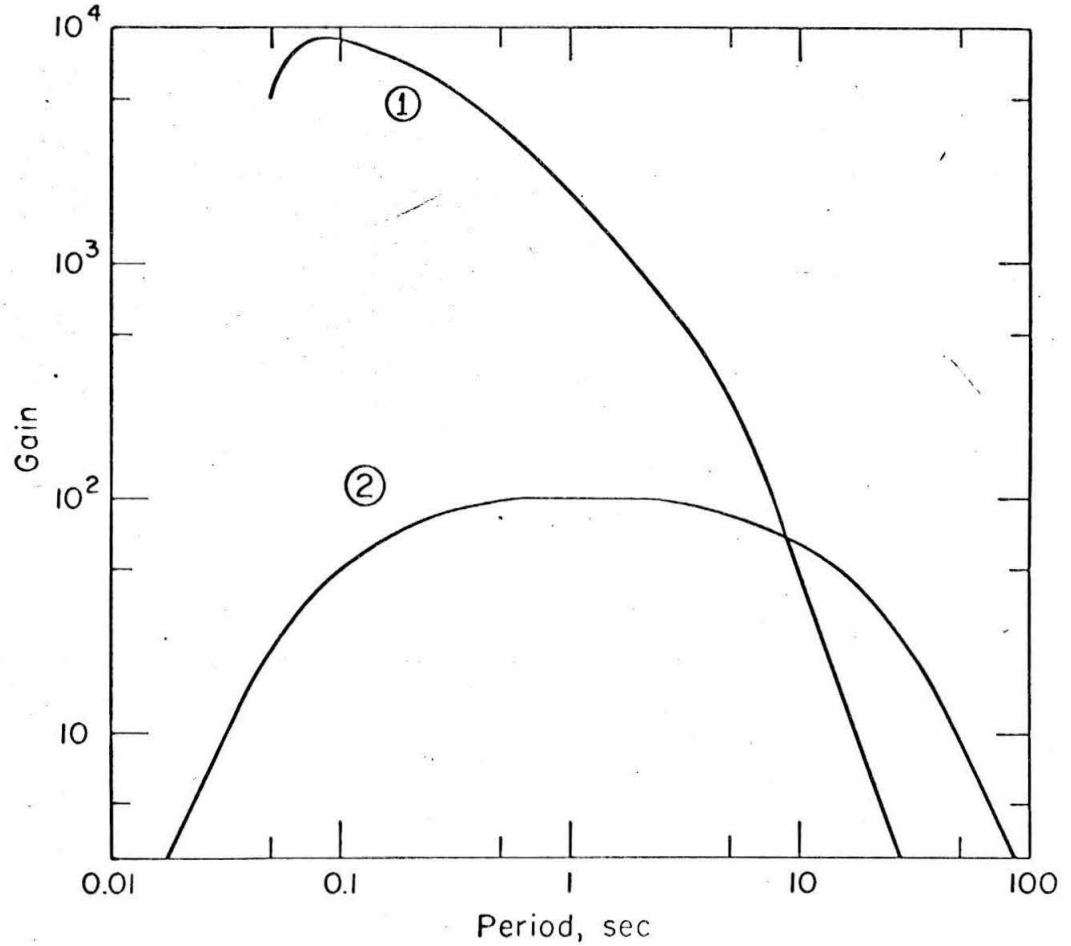

Figure 30. Instrument response of the long period pendulum, curve 1, and the "jerk-meter," curve 2.

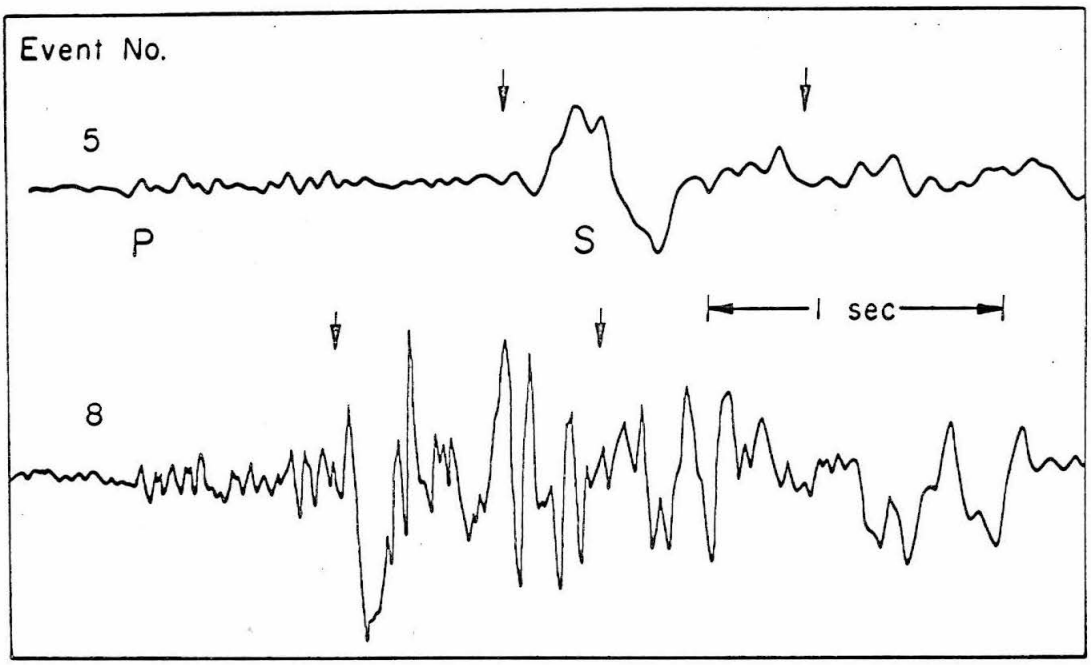

Figure 31. Two examples of small earthquakes recorded by the long period pendulum at Squaw Peak, Borrego Mountain, California.

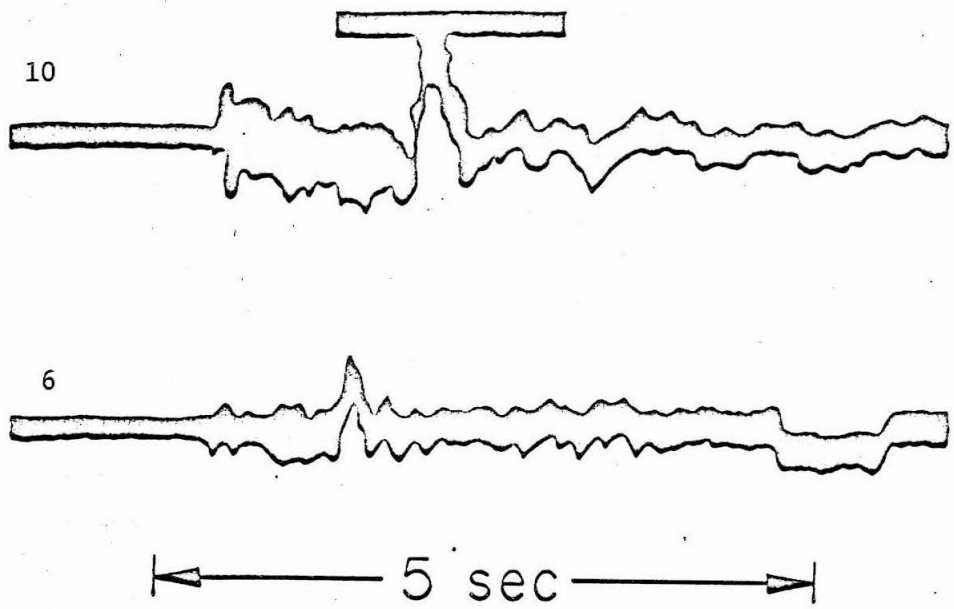

Figure 32. Two examples of earthquakes recorded on the "jerk-meter" at Squaw Peak, Borrego Mountain, California.

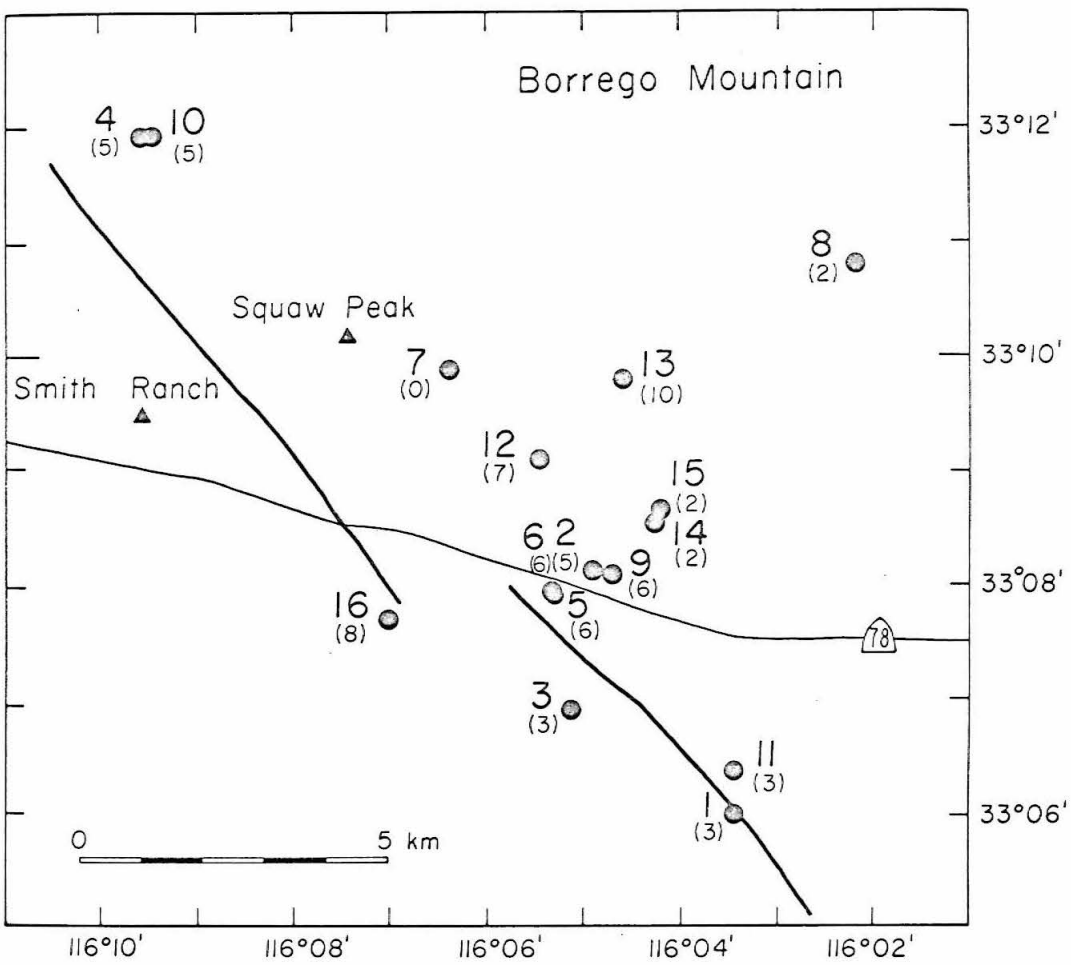

Figure 33. Map showing epicenters of the analyzed Borrego earthquakes (Hamilton, 1970), recording sites and surface fault trace (Allen et al, 1968).

Selection of Data

The effective attenuation (anelastic attenuation and scattering) can severely modify the recorded high frequency seismic spectrum even at a moderate distance from the source. For this reason only earthquakes with hypocentral distances of less than 11 km were studied; 11 km was chosen because with this maximal distance the whole depth range could be covered. Figure 33 is a map of the two recording sites and the epicenters of the 14 analyzed earthquakes.

Press (1964) found that the Lg phase was attenuated with a Q-factor of about 500 in granite. In the present study a Q factor close to that value but somewhat smaller, would be expected for most events, because the larger parts of the ray paths are likely to lie in granite with the rest in sediments. A Q value of 50 can be considered an extreme lower limit. The modification of the spectrum by the effective attenuation is demonstrated in Figure 34. It is seen that for an extreme value of Q = 50, the effect on the spectrum is appreciable. The earthquake in Figure 34, event number 8, is one of the most unsatisfactory ones. Even with a high Q value the division of the spectrum in a constant and a decreasing part is not very clear. For Q = 50 the drop-off frequency ν_o cannot be determined in the analyzed range. An earthquake like number 5, Figure 35, however, is much less affected

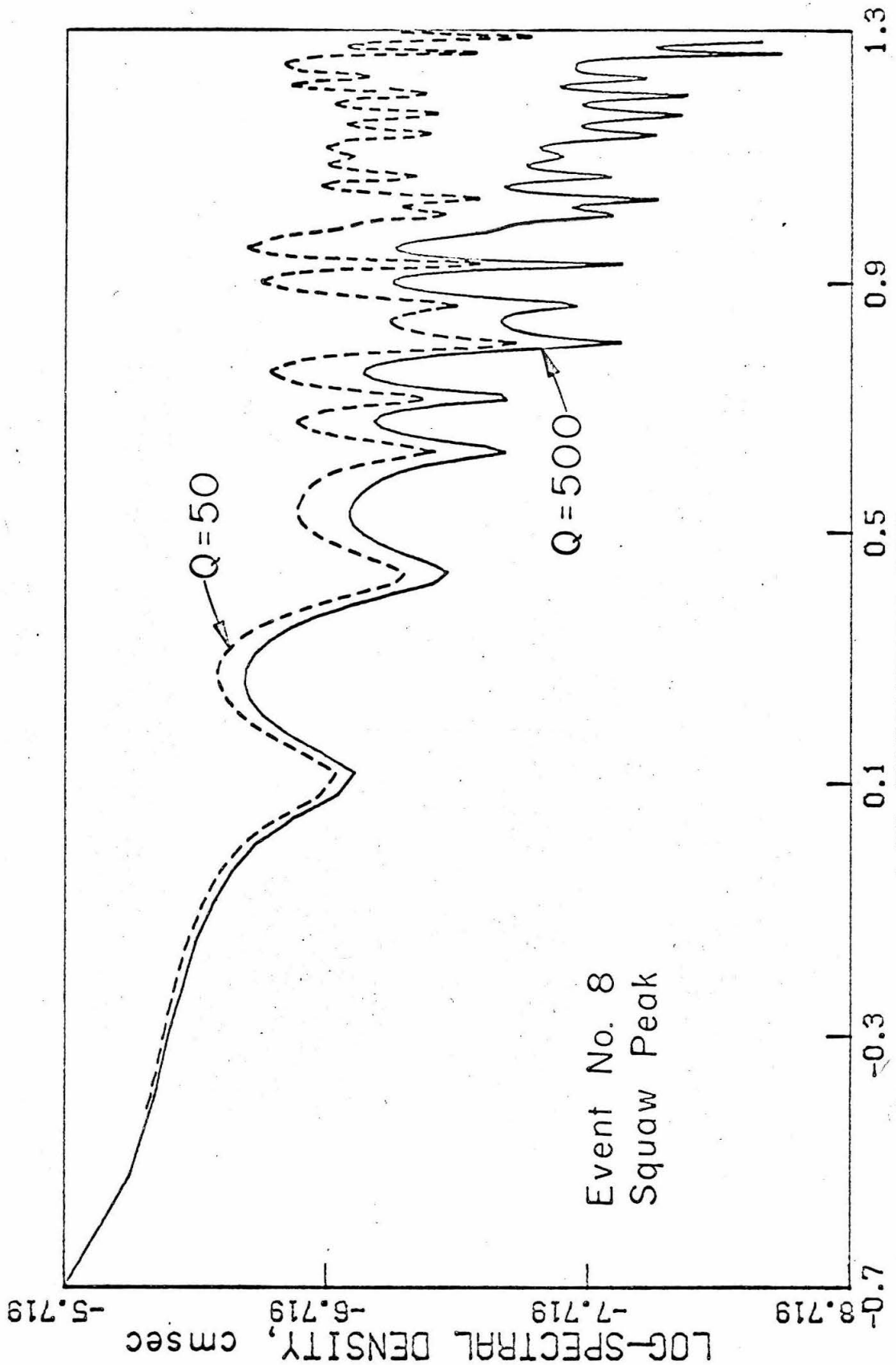
LOG-SPECTRAL DENSITY, cmsec
-5.719
-6.719
-7.719
-8.719
-0.7
-0.3
0.1
0.5
0.9
1.3
LOG-FREQUENCY, CPS
Q=50
Q=500
Event No. 8
Squaw Peak

Figure 34

by a low Q-value and ν_o can be determined for Q = 50. For this study a Q factor of 300 was taken. The values of the seismic moment would not be altered if Q = 50 were chosen, however, the values of the source dimension would have to be divided by about two for most events, which would imply that the stress drops would have to be multiplied by 8, and the inferred dislocation at the source would be larger by a factor of 4. The calculated energy carried by the S-wave would be modified by more than an order of magnitude.

It is concluded that for most studied earthquakes with restriction of the distance to 11 km, all source parameters except the energy and the apparent stress can be quite safely estimated. The analyzed earthquakes are listed in Table 6. ϕ is the azimuth of the strike, δ the dip, and λ the slip angle.

Seismic Moment

The long-period level of the S-wave spectra was corrected for (a) attenuation with Q = 300, (b) the effect of the free surface using Gutenberg's (1944) results, (c) the orientation of the instrument assuming a direct ray from source to receiver, and (d) the radiation pattern using the results of Ben-Menahem et al (1965). For all the analyzed earthquakes first motion studies were kindly made available by R. Hamilton, U.S.G.S., Menlo Park. The fault plane solutions for more than half the shocks were well defined.

Table 6

Selected Earthquakes, Borrego Mt.*

No.	Date d	m	y	Time h	m	s	Lat. minutes over 33°N	Long. minutes over 116°W	Depth km	Fault mech. parameters* ϕ deg	δ deg	λ deg
1a	24	04	68	04	12	41	06.00	03.43	2.8	65	90	0
1b	24	04	68	04	12	41	06.00	03.43	2.8	110	45	90
1c	24	04	68	04	12	41	06.00	03.43	2.8	20	45	90
3	24	04	68	07	30	27	06.92	05.12	2.6	240	40	56
4	24	04	68	07	49	34	11.92	09.56	5.4	298	68	90
5a	24	04	68	09	01	02	07.96	05.30	5.7	64	90	0
5b	24	04	68	09	01	02	07.96	05.30	5.7	249	50	40
6	24	04	68	09	03	12	07.97	05.34	5.7	231	70	-20
7	25	04	68	06	57	46	09.88	06.38	2.7	225	70	0
8	25	04	68	07	33	16	10.80	02.17	1.8	203	61	-33
9	25	04	68	10	14	24	08.09	04.70	5.9	45	90	0
10	27	04	68	09	32	30	11.95	09.44	5.1	295	50	41

Table 6 (continued)

No.	Date d	m	y	Time h	m	s	Lat. minutes over 33°N	Long. minutes over 116°W	Depth km	Fault mech. parameters* ϕ deg	δ deg	λ deg
11	29	04	68	01	03	00	06.37	03.43	2.7	14	90	0
12	29	04	68	02	05	31	09.10	05.43	7.4	255	80	20
13	29	04	68	12	58	13	09.80	04.58	10.3	24	60	-23
14	01	05	68	11	36	24	08.55	04.24	2.2	26	90	0
15	01	05	68	11	36	37	08.65	04.19	1.6	231	76	53
16	03	05	68	05	09	44	07.71	07.00	8.4	221	55	39
2	24	04	68	07	29	34	08.13	04.89	5.2	50	70	54

*Data kindly furnished by R. Hamilton, Menlo Park.

The seismic moment was computed with the equation

$$M_o = \tilde{u}\ 4\pi R\beta^2$$

given by Keilis-Borok (1959), where $\tilde{u}$ = corrected spectral amplitude, R = hypocentral distance and β = shear wave velocity. The results are given in Table 8. The value for the uncorrected level of the long-period spectral density is given in Table 7.

Source Dimensions

Several investigators have related the corner of the seismic body wave spectra where the amplitude starts to drop off (ν_o in Figure 15) to the dimensions of theoretical source models (e.g. Kasahara, 1957; Berckhemer and Jacob, 1968). Most of these models were based either on a spherical source volume or on dislocation theory. Brune (1970) has recently developed a theory relating the amplitude spectra of S-waves to a source with a propagating stress step function. In this study source dimensions are obtained by comparing observed spectra to theoretical spectra. Because the direction of propagation is not known, the curve given by Brune (1970) for an average position of the recording site with respect to the propagation direction, was used.

Table 7

Spectral Data, Squaw Peak

No.	Distance Hypocentre km	Azimuth at Station deg.	LP Spectr. Dens. cm sec 10^{-6}	$\nu_o = \frac{\omega_o}{2\pi}$ cps	E_{SV} erg 10^9
1a	10.3	141	0.17	3.7	(22.8)
1b	10.3	141	0.17	3.7	2.0
1c	10.3	141	0.17	3.7	3.8
3	7.5	144		2.8	-
4	7.1	-45	0.8	3.4	-
5a	7.8	141	0.37	2.2	6.4
5b	7.8	141	0.37	2.2	1.0
6	7.7	141	16.5	1.9	-
7	1.8	109	0.8	2.0	-
8	8.5	82	0.36	4.6	-
9	8.3	132	0.082	3.4	-
10	10.4	-43	4.7	5.2	-
11	9.8	139	0.18	4.0	8.5
12	8.3	123	0.5	2.2	-
13	11.2	99	0.51	2.9	-
14	6.2	121	0.25	4.9	-
15	6.0	119	1.67	3.3	-
16	9.6	171	1.1	3.5	-

Table 7 (continued)

Spectral Data, Smith Ranch

No.	Distance Hypocentre	Azimuth at Station deg.	LP Spectr. Dens. cm sec 10^{-6}	$\nu_o = \frac{\omega_o}{2\pi}$ cps	E_{SV} erg 10^9
2	9.3	109	0.594	2.4	-
3	8.8	124	0.1	3.2-6.2	-
4	7.1	0	1.0	2.6	-
5a	9.2	113	0.37	5.2	-
5b	9.2	113	0.37	5.2	-

In Figure 35 an example of a fit of the theoretical to the observed spectrum is shown. A comparison with the instrument response curve (Figure 30) will convince the reader that the shape of the S-wave spectrum is not produced by the instrument. The arrow in Figure 35 indicates the frequency ν_o which, after the fit, coincides with $\omega/\alpha = 1$ of the theoretical curve. ω/α is the dimensionless frequency constituting the abscissa of Brune's (1970) theoretical plots. The radius of a circular source is obtained using Brune's definition of α

$$\frac{\omega}{\alpha} = \frac{1}{2.21} \frac{\omega r}{\beta} = 1$$

where $\omega = 2\pi \nu_o$ and r is the radius of the source, it follows $r = \frac{1.1}{\nu_o}$. For the analyzed earthquakes ν_o is given in Table 7 and r is given in Table 8 (Q = 300). In the extreme case of Q = 50 the radius would have to be divided by approximately 2.

Stress drop and Dislocation

The source dimensions were obtained for the case of a circular source. In this case the stress drop is calculated from the moment and the source radius by

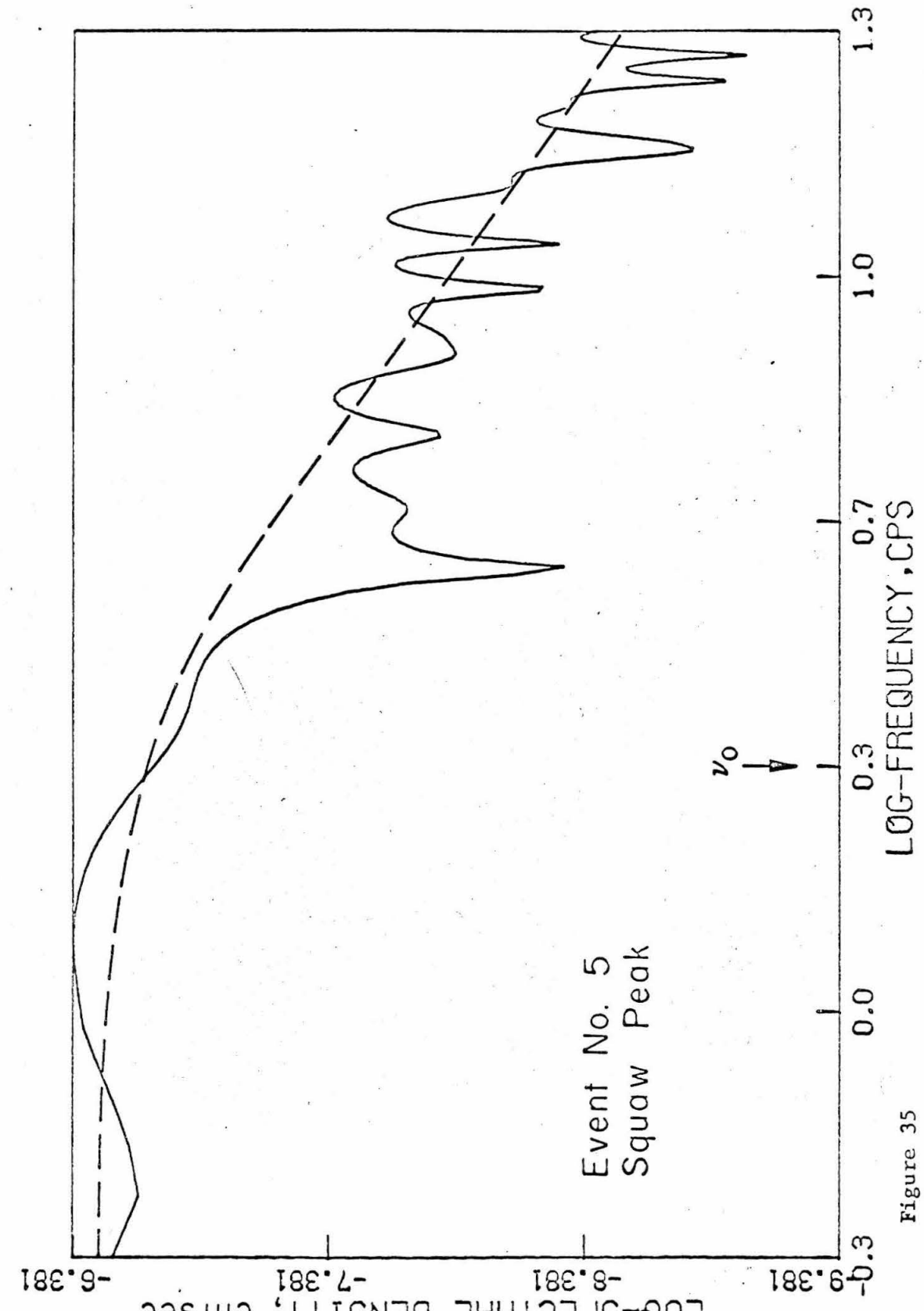
LOG-SPECTRAL DENSITY, cm sec
-6.381
-7.381
-8.381
-9.381
-0.3
0.0
0.3
0.7
1.0
1.3
LOG-FREQUENCY, CPS
ν_o
Event No. 5
Squaw Peak

Figure 35

Table 8

Moments and Source Dimensions, Squaw Peak

No.	Moment dyne-cm 10^{18}	Source Radius km	Stress drop bar	M_{GS}^*	Depth* km	Dislocation cm 10^{-2}	Quality
1a	(3.7)	0.3	(0.053)	1.09	2.8	0.21	B
1b	1.0	0.3	0.014	1.09	2.8	0.21	B
1c	1.4	0.3	0.02	1.09	2.8	0.21	B
3	(1.5)	0.4	0.009	0.92	2.6	0.15	B
4	1.1	0.32	0.013	1.68	5.4	0.12	B
5a	2.5	0.5	0.008	1.25	5.7	0.09	B
5b	1.9	0.5	0.006	1.25	5.7	0.09	B
6	(1400.)	0.6	2.5	2.6	5.7	41.	B
7	0.64	0.4-0.5	0.003	1.48	0	0.06	B
8	2.0	0.24	0.057	1.63	1.8	0.56	A
9	node	0.32	-	0.56	5.9	-	C
10	3.6	(0.25)	(0.09)	2.26	5.1	0.62	B
11	2.1	0.28	0.038	1.22	2.7	0.43	A
12	0.6	0.5	0.002	1.31	7.4	0.03	A
13	1.1	0.38	0.008	1.66	10.3	0.08	A
14	(0.5)	0.22	0.009	1.1	2.2	0.02	B
15	9.0	0.32	0.108	1.54	1.6	1.4	A
16	2.5	0.31	0.03	1.68	8.4	0.29	A

Table 8 (continued)

Moments and Source Dimensions, Smith Ranch

No.	Moment dyne-cm 10^{18}	Source Radius km	Stress drop bar	M^*_{GS}	Depth* km	Dislocation cm 10^{-2}	Quality
2	9.1	0.46	0.366	1.51	5.2	0.46	B
3	0.62	0.34-0.18	0.006-0.036	0.92	2.6	0.15	B
4	1.1	0.43	0.005	1.68	5.4	0.07	B
5a	3.4	0.2	0.166	1.25	5.7	0.72	B
5b	2.0	0.2	0.098	1.25	5.7	0.72	B

*Hamilton (1970)

$$\tau = \frac{7}{18} \frac{M_o}{r^3}$$

(Brune, 1970), and the dislocation is obtained from the definition of the moment (Aki, 1966)

$$\bar{u} = \frac{M_o}{\mu \pi r^2}$$

Both of these parameters are given in Table 8.

Energy

The estimate of the seismic energy radiated by the source of these small earthquake is a very crude approximation. There are too many factors of uncertainty for a good estimate. A large contribution to the S-wave energy comes from frequencies around 10 cps. The energy estimate can be changed by an order of magnitude by changing Q by a factor of 2. The same corrections that were applied to the spectral density for the moment determination will have to be made for the energy estimate. Because the energy depends on amplitude squared, all these corrections will be squared.

An attempt was made to estimate for a few earthquakes the amount of SV energy radiated in the frequency band 0.5 to 20 cps.

Wu's (1966) procedure was used and the results are given in Table 7.

An additional uncertainty factor arises from the fact that for most fault plane solutions the partitioning of energy was such that most of the energy was contained in the SH wave. The geometry of the experiment, however, was such that SV motion was preferentially recorded. The SV energy in Table 7 is therefore a lower bound. If the other phases were considered, the total energy would typically be a factor of 5 higher.

The determination of all the source parameters was based on the assumption that the analyzed wave was an S-wave uncontaminated by surface waves. The length of the digitized part of the seismic record was typically about 2 sec. This window (arrows in Figure 31) was taken in order to minimize the contamination by surface waves, yet to allow, on the other hand, a reliable determination of the spectral density at a frequency of 0.5 cps. The recording site in most cases was located so close to the source that the angle of incidence of a direct ray was larger than 45°, and the distance to the epicenter was about two wavelengths (of a one second wave).

Magnitude

Magnitudes determined by the USGS, M_{GS}, were available for all studied events. It was determined from 20 cps P-waves according to the procedure described by Eaton et al (1970). Some of the larger of the events produced a deflection of the Wood-Anderson instrument at Barrett, a station of the CIT network, about 70 km from the source region. For these shocks local magnitude, M_L, was estimated.
M_L was found to be about 0.4 larger than M_{GS}, around magnitude 1 1/2. With two exceptions, all the analyzed events are within a half order of magnitude of each other. Therefore, it was decided to use a local magnitude derived from M_{GS} by

$$M_L = M_{GS} + 0.4 \qquad \text{at } M_{GS} \cong 1 - 1\ 1/2$$

M_{GS} is given in Table 8 but M_L is used in the figures and in the discussion. For the two largest events M_L as observed at Barrett was used.

Discussion

First, the moment-magnitude relation is of interest. Figure 36 shows that the relation established earlier for the western United States can be extended down to magnitude 1 without modification

$$M_o = 1.7M + 15.1 \qquad 1 \leq M_L \leq 6$$

Another relation that has been of interest to seismologists for years is the length-magnitude relation. In Figure 37, the length, L = 2r, of the Borrego Mountain aftershocks are added to the data previously obtained. Down to magnitude two the Borrego data confirm the earlier estimate based on the Parkfield data and the data of Smith et al (1967). For Borrego shocks with magnitudes smaller than two, however, the inferred fault lengths are excessively large and scatter greatly.
No peculiarity could be found in the experiment that could artificially alter the source size versus magnitude dependence. As mentioned earlier, if we chose a Q factor of 50 the dimensions would be decreased by a factor of approximately 2. It is felt that the lack of correlation with magnitude has to be explained by the rupture mechanism. Two rupture mechanisms that could account

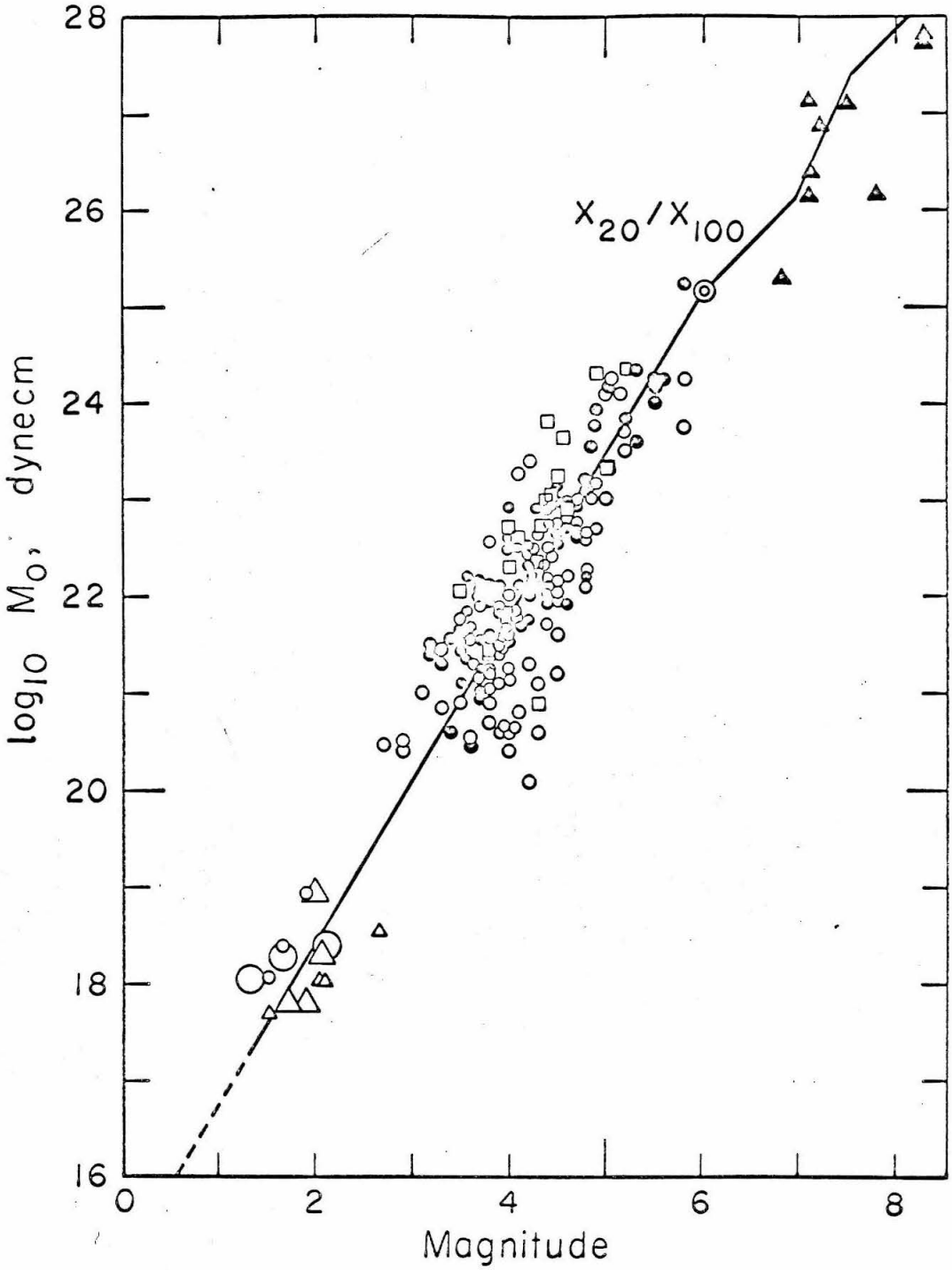

Figure 36. Moment-magnitude relation for small earthquakes. For the smallest shocks triangles indicate events with epicenters more than 2 km from the fault trace.

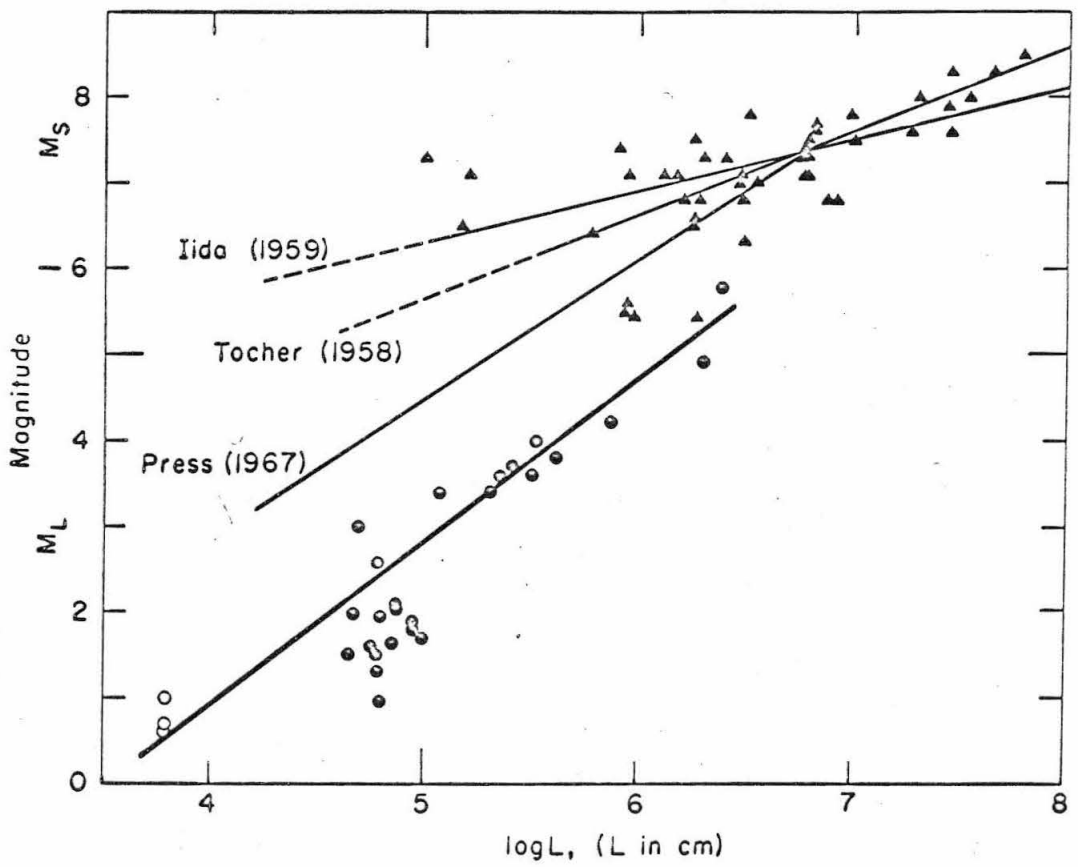

Figure 37. Magnitude-fault length relation. Triangles are after King and Knopoff (1968a).

for the observations will be discussed later.

The large source dimensions imply that the dislocation and the stress drops (Table 8) are extremely small. The dislocations are of the order of 10^{-3} cm and the stress drops of the order of 10^{-2} bars. The scatter is considerable. One is not used to thinking in terms of such small values, however, they agree with the stress drop-magnitude relations put forth by King and Knopoff (1968a), and there is nothing physically impossible about them.

If these fault lengths are accepted as representative, the magnitude vs length relation (eq. 14) is no longer valid for these small shocks. This would imply that the energy versus length relation (equation 15) would change to $E_S \sim L^{4.6}$. The elastic energy, however, is expected to depend on L^3 approximately. This discrepancy can be explained by a decrease of the seismic efficiency factor with smaller shocks. We will later see that there are other reasons as well, to believe that the seismically radiated energy is an unusually small fraction of the elastic energy released by the Borrego Mountain earthquakes.

In Figure 38 the Parkfield and Borrego data are added to the plot of LD^2 (length times dislocation squared) versus magnitude by King and Knopoff (1968a). The straight line through the data is the relation proposed by King and Knopoff to hold for magnitudes

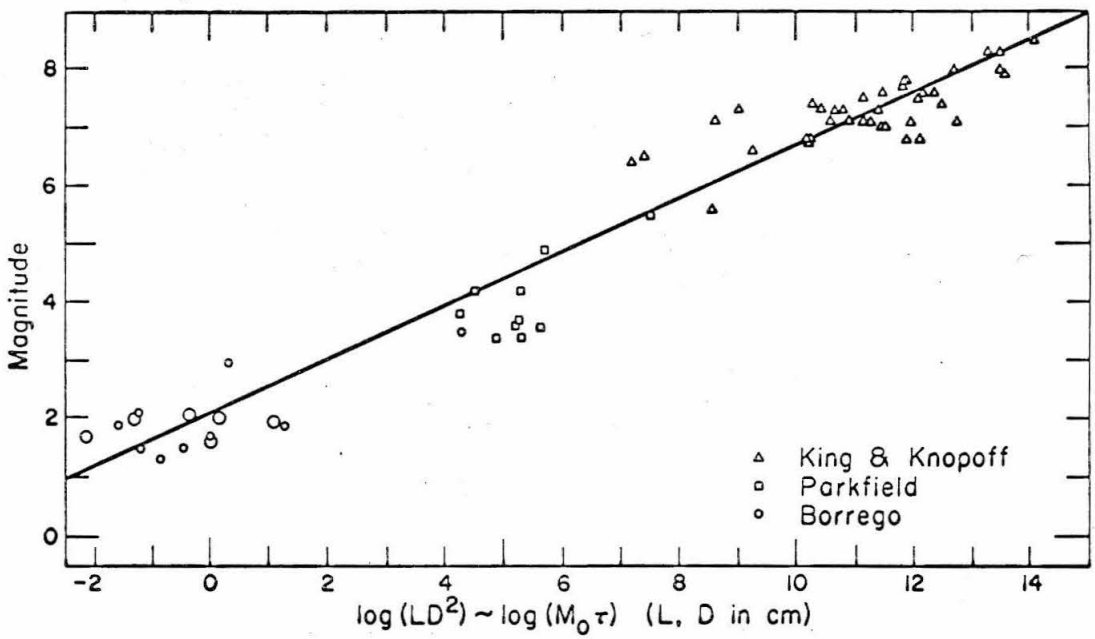

Figure 38. Magnitude versus moment times stress drop..

larger than five. The relation is

$$\log LD^2 = 2.24\ M - 4.99 \qquad 1 \leq M \leq 8.5 \qquad (17)$$

It seems to hold over the entire range of the data. This is surprising because (a) the magnitudes in this range are based on different instruments and definitions, and (b) a single relation holds over 17 orders of magnitude.

An important fact that had not been noted by King and Knopoff, is that the product of LD^2 can be related to the product of moment times stress drop. From the relation of moment to the fault

area and dislocation (Aki, 1966), together with the stress drop definition we get

$$\begin{aligned} M_o &= \mu LWD \\ \tau &= k \frac{D}{W} \mu \\ M_o \tau &= k\mu^2 LD^2 \end{aligned} \qquad (18)$$

where k is a constant factor which takes on different values for different fault geometry. This factor is four times smaller in the case of an infinitely long vertical surface strike-slip fault (Knopoff, 1958) than it is in the case of a circular fault plane in an infinite medium (Neuber, 1937; Keilis-Borok, 1959). In the case of a dip-slip fault, the value of k is in between the other two cases (Starr, 1928). Equations 18 show that the LD^2 dependence on magnitude (equation 17) implies an $M_o \cdot \tau$ dependence on magnitude. Since we have derived the M_o-magnitude dependence earlier, the implication is that the τ - magnitude dependence can be derived from the LD^2-magnitude plot. King and Knopoff (1968a) came to the same conclusion on the basis of the relation of LD^2 to the elastically released energy. Their argument has the disadvantage that (a) the magnitude energy relation holding

in the magnitude ranges of interest, must be known, (b) the seismic efficiency is assumed constant, and (c) the value of the efficiency must be assumed. In the present argument involving the seismic moment, none of these assumptions are necessary.

We can, for instance, derive the stress drop-magnitude relation using equations 17 and 18 with an average $k = \frac{4}{3}$ and $\mu = 3.10^{11}$ and using the following smoothed moment-magnitude relation based on Figure 19:

$$\log M_o = 1.55\ M + 15.6 \qquad 1 \leq M \leq 8.5 \qquad (19)$$

we obtain as an approximation

$$\log \tau = 0.69\ M - 2.66 \qquad 1 \leq M \leq 8.5 \qquad (20)$$

This equation is an average for various tectonic regions. It is expected that the equation will be altered slightly for individual tectonic conditions. In particular, regions with higher shear stresses will have smaller additive constants and regions with lower stresses will have larger additive constants. The equation is valid for shallow earthquakes only. Equations 19 and 20 are approximations because k can vary. We will now look at the data in more detail and avoid this inaccuracy.

Instead of eliminating the seismic moment from equations 17, 18, and 19, to obtain equation 20, we could eliminate the magnitude. This procedure is more desirable because the moment is a more physically meaningful quantity. Rather than obtaining the stress drop-moment relation from these equations, we will compute the stress drop for each individual earthquake and plot it against the moment. In this way, each time we can use the appropriate value for k and eliminate this uncertainty factor.

The stress drops plotted in Figure 39 against moment, are based on the data collected from the literature by Brune and Allen (1967) and Chinnery (1969) together with the data presented in this work. The values of the two largest events, Alaska 1964 and Kurile 1963, were obtained from Kanamori (1970b and 1970a). Figure 39 shows that the stress drop increase with moment

$$M_o = 10^{23} \cdot \tau^{2.86} \qquad 17 \leq \log M_o \leq 31 \qquad (21)$$

An approximate magnitude scale is given on the top of Figure 39. A stress drop magnitude relation (more accurate than that in equation 20) is obtained by combining equations 19 and 21. This relation is

$$\log \tau = 0.54\ M - 2.58 \qquad 1 \leq M \leq 8.5 \qquad (22)$$

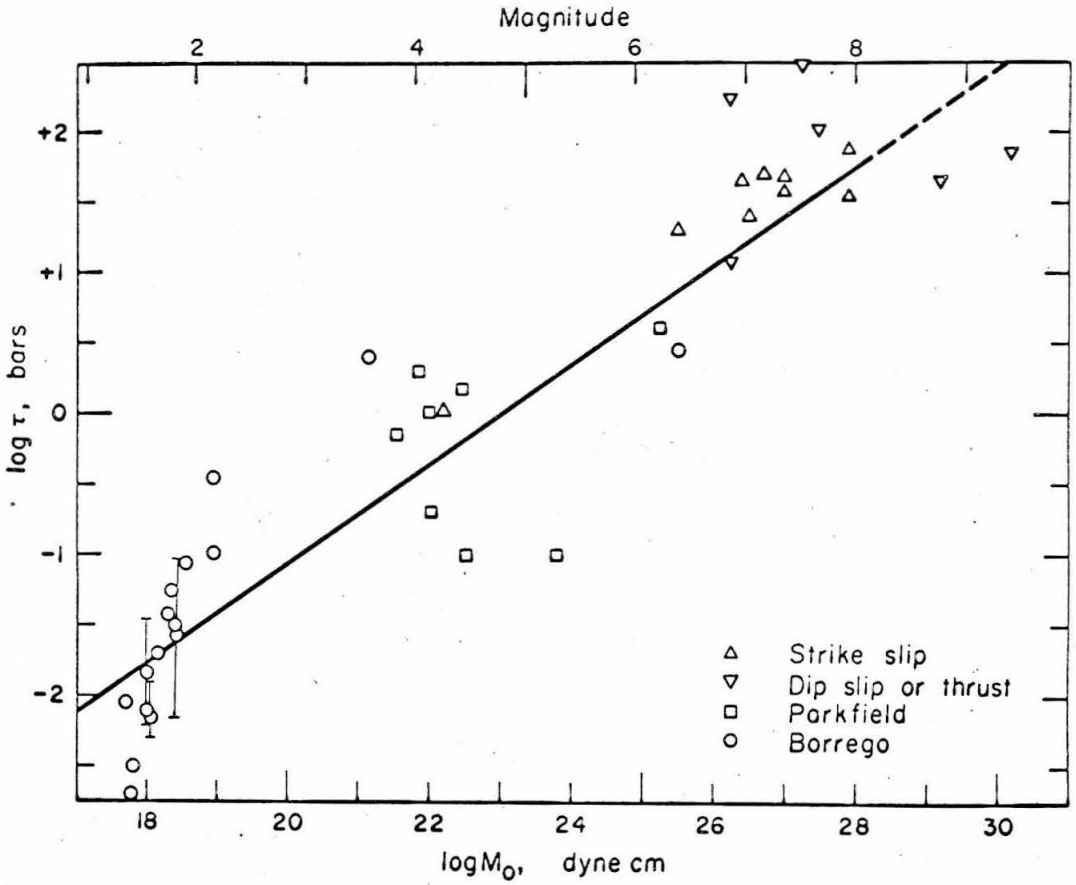

Figure 39. Stress drop versus moment and magnitude.

The factor 0.54 in equation 22 corresponds to King and Knopoff's parameter a_1. This means that for the average tectonic region the curve with parameter $a_1 \cong 0.54$ in King and Knopoff's plot of fractional stress drops versus magnitude is the correct one. Based on limited data for the San Andreas region, Scholz et al (1969) found $a_1 = 0.4$. In Table 9 the stress drops corresponding to equation 22 are given as a function of magnitude.

Table 9

Manitude M	Stress drop τ, bars
8.5	100.
8	55.
7	16.
6	4.6
5	1.3
4	0.4
3	0.11
2	0.03
1	0.01

The stress drop of the largest earthquakes give a minimum estimate of the crustal strength, as pointed out earlier by Chinnery (1964) and Brune et al (1968). There is a considerable scatter in the data. Particularly, at small moments the stress drops vary over more than an order of magnitude. However, in Figure 39, twenty-nine of the thirty-nine data points are within a factor of 3 from the straight line fitted to the data.

The attempt to reduce equation 21 to a relation between more fundamental parameters like linear dimension and dislocation, is not very successful, because for many earthquakes, length and width are different by an order of magnitude. If we were dealing with roughly rectangular or circular sources, which is probably the case for a considerable number of earthquakes, equation 21 would imply

$$\overline{u} = \text{const} \cdot r^{2.6}$$

No physical explanation of the significance of such a relationship is offered here. In fact, it is doubtful that any simple relationship should hold over a magnitude range from 1 to 8.5. It is more likely that a different rupture mechanism is associated with large and small earthquakes. At intermediate magnitudes a mixture of the two mechanisms may take place. Some suggestions for such

mechanisms are presented later in this chapter.

Originally, it was intended to obtain the apparent stresses as a function of depth between 0 and 10 km. This was made impossible by the smallness of the recorded energies in relation to the large inferred source dimensions. If the SV-energy in Table 7 is divided by the moment, an apparent strain of 10^{-10} is obtained. A similar value is computed if equation (53) by Brune (1970) is used. This would indicate that small earthquakes have exceedingly low efficiency for radiating waves, or that they have large incoherent sources, or that very small dislocations sealing behind themselves can propagate over large areas. Yet the data are definitely divided into two groups in Figure 36. The Borrego aftershocks whose epicenters fall within 1 km from the surface trace (circles) plot above the average line, as low stress events do, and the shocks with epicenters off the fault trace (triangles) plot below, as high stress events do. The size of the symbols reflects the quality of the solutions. This result might be explained if the apparent stress reflects the strength of the material in the source region. The well developed fault surface is a zone of weakness offering less resistance to accumulating stresses than does the less fractured material away from the fault.

The large source dimensions and small energies of the small Borrego Mt. earthquakes could be explained by the hypothesis that we are dealing with incoherent sources. In this hypothesis it is postulated that actual rupture takes place only on several small and distributed portions of the inferred fault surface. This is a multiple event mechanism. A given small earthquake is made up of a sequence of fault slips. In this model the portions of fault area linking individual ruptures do not rupture, but adjust elastically to the strain drops in the neighboring bursting areas. Let us estimate the order of magnitude of the strains that would have to be stored elastically. If we assume individual dislocations of 10 times the average value occurring over one-tenth of the total area, the strain drop of one such burst would be approximately 0.3×10^{-5}, corresponding to 1 bar stress drop. Such a small amount of strain could easily be stored elastically along the unbroken parts of the fault.

In another similar hypothesis, the dislocation over the fault surface may be taken as approximately constant and caused by a small propagating dislocation (the fault surface becomes sealed after the dislocation passes). The area of such a source could be arbitrarily large and is controlled only by the local geological properties which determined the particular stress distributions in the source region. The source areas of all

studied earthquakes in the Borrego region are approximately the same and equal to 0.1 km^2. A comparatively small earthquake would have a correspondingly small dislocation over the same source size. The total seismic moment of such a source is still determined by the spectral amplitudes of waves with periods longer than the time required for the dislocation for propagation over the entire source area. This model is similar to the multiple event source except that the energy release is assumed to occur smoothly rather than erratically.

At present, there is no evidence for or against multiple event sources for very small earthquakes. In the following chapter, it is shown that such a mechanism is appropriate for some large earthquakes. In the theoretical study by Brune (1970) such sources are properly modeled as sources with very small stress drop.

The effect on the energy radiated and the apparent stress calculation can be seen in the following way: The amplitudes of waves with wavelength comparable to the fracture length, for instance, the length of the propagating dislocation, are proportional to the stress drop, not the total stress. The model of a dislocation propagating and sealing up behind, implies

that the dislocation length, the length over which simultaneous displacement motion occurs, is smaller than the source. If we choose the dislocation length to be smaller or equal to 100 m, a very weak constraint, the wavelengths of the entire frequency band recorded in our experiment will be comparable to or larger than the dislocation length. This means that all spectral amplitudes observed will be proportional to the stress drop rather than the total stress.

This hypothesis is a plausible one for small earthquakes where the displacements are small and could be imagined to occur as dislocation without the production of melt on the fault surface (Brune and McKenzie, personal communication). For large earthquakes this hypothesis may not be applicable. Melting might always occur causing the stress drop to nearly equal the total stress. Brune and McKenzie suggest on this basis that earthquakes might be divided in two categories with different dependence of source parameters on magnitude.

The third hypothesis with which we could explain the smallness of the radiated energy with respect to the moment, is that melting is associated with small

earthquakes, as well as large earthquakes. The energy that is lacking in the radiation of the Borrego Mt. shocks could all have been absorbed in the melting process. If melting occurs, small earthquakes are expected to be less efficient in seismic radiation (see chapter IV), than large ones. It is felt that at this point the data for intermediate size earthquakes are not sufficient to warrant a final choice of source mechanism.

CONCLUSIONS

The following relationships between moment M_o and local magnitude M_L have been found:

Parkfield

$$\log M_o = 1.4\, M_L + 17.0 \qquad 3 < M_L < 6$$

Western United States

$$\log M_o = 1.7\, M_L + 15.1 \qquad 1 < M_L < 6$$

This result indicates that the contribution of small earthquakes to the slip in active tectonic zones is relatively insignificant.

From the Fourier spectral densities of the surface waves used in this study, the following relationship between M_L and surface wave magnitude M_S is derived:

$$M_S = 1.7\ M_L - 4.1 \qquad 1 < M_L < 6$$

An approximate relationship for obtaining the seismic moment from the surface wave parameter AR of Brune et al (1963) has been derived:

$$\log M_o = \log AR_{300} + 20.1$$

Large regional variations in the excitation of long-period surface waves have been interpreted in terms of regional variations in the product of the average stress times the seismic efficiency. This product varies from about 7 bars along the San Andreas fault to over 100 bars in the Laguna-Salada and Nevada-Arizona regions.

Field measurements have yielded approximate estimates of fault offset, length, and width for earthquakes in the Parkfield region. For aftershocks of the Borrego Mountain earthquake, S-wave spectra obtained at hypocentral distances of less than 11 km were compared with theoretical spectra. In this way, fault dimensions of earthquakes as small as magnitude 1 were estimated. Source dimensions of earthquakes on active strike-slip faults in Southern California are related to magnitude by the following equation:

$$M_L = 1.9 \log L - 6.7 \qquad 3 < M_L < 6$$

Thus, the source dimensions for these earthquakes are much larger than for equivalent magnitude explosions. This may, in part, be the explanation for the relatively greater excitation of surface waves by earthquakes than by explosions of equivalent local magnitude M_L.

The product of LD^2 is related to the product of τM_o and it is shown that the stress drop τ is a function of magnitude, i.e. is a function of moment

$$M_o = 10^{23} \tau^{2.86}$$

This relation holds approximately in the magnitude range 1 to 8.5 and implies that the dislocation scales roughly with the fault dimension to the 2.6 power. The corresponding stress drop magnitude relation is $\log \tau = 0.54 M - 2.58$.

For small local earthquakes in the Borrego Mountain region, a source model of the propagating dislocation of approximately 10^{-3} cm that seals behind itself and propagates either smoothly or erratically over relatively large areas is found to be the most plausible explanation of the observations. The amount of high frequency energy radiated in the frequency band 0.5 to 20 cps by these small earthquakes,was insufficient to obtain an estimate for the absolute stresses in the source region.

Chapter III

SEISMIC TRIGGERING AND SEISMIC SHAKING AS MECHANISMS FOR TECTONIC STRAIN RELEASE

ABSTRACT

Evidence is given that seismic triggering and seismic shaking can act as mechanism for tectonic strain release. Seismic triggering (a small event causing larger later events) is considered to have played an important role in the 1964 Alaska earthquake, M = 8.4. The Borrego Mountain earthquake, 1968, M = 6.5, is believed to have caused displacement on distant faults by seismic shaking.

The seismograms of the Alaskan earthquake of 28 March 1964 are characterized by multiple P-phases not predicted by the travel time curves. Seismograms with low magnifications from 80 stations covering distances from 40° to 90° and a wide range of azimuths were analyzed. The character of the P-wave portion of the seismograms is interpreted in terms of an approximate multiple event source mechanism where

the propagating rupture triggers larger distinct events. Six events were located using the Gutenberg sine-curve method. The times after the initial origin time were 9, 19, 28, 29, 44, and 72 sec respectively, and the events were located 35, 66, 89, 93, 165, and 250 km away from the initial epicenter. Dividing the distance by the delay-time gives an average rupture velocity of 3.5 km/sec.

The Borrego Mountain earthquake of 9 April 1968 caused small but consistent surface displacements on three faults far outside the source area and zone of aftershock activity. Right-lateral displacements of 1 to 2 cm occurred along 22, 23, and 50 km segments of the Imperial, Superstition Hills, and San Andreas (Banning-Mission Creek) faults, respectively, at distances of 70, 45, and 50 km from the epicenter. Although not noticed until four days after the earthquake, association of these fractures with the earthquake is suggested by the freshness of the en-echelon cracks at that time, and the fact that creep was not occurring along most of these faults during the year before or the year following the event. Dynamic strains associated with propagating waves (shaking) are a more likely cause of the distant displacements than the static strain caused by the main fault, inasmuch as the dynamic strains were much larger, and the static strain at the San Andreas

fault was in the wrong sense for the observed displacements. All three of the distant faults are "active" faults in that they show evidence of repeated Quaternary displacements, and surface displacements occurred only along those segments where the fault trace is well delineated in surface exposures, at least in uncultivated areas. This is the first documented example of fault displacement caused by seismic shaking far from the source area, although it has probably gone undetectd many previous times here and in similar tectonic environments. This phenomenon forces us to be much more conservative in estimating the probabilities of surface displacements along active faults in seismic regions.

THE ALASKA EARTHQUAKE OF 28 MARCH 1964: A COMPLEX MULTIPLE RUPTURE

Introduction

The region of energy release during large shallow earthquakes, as determined from the distribution of aftershocks, surface rupture, and long-period surface-wave radiation, is of the order of 500 to 1000 km length. However, the nature of energy release that occurs in this zone is not well understood. Surface wave radiation suggests that the gross pattern of energy release

is like a propagating source (Benioff, 1955a; Benioff et al, 1961; Ben-Menahem, 1961; Ben-Menahem and Toksoz, 1962, 1963; Press et al, 1961) with velocity of about 3 km/sec, but the long wavelengths used lack the resolution to determine the details of the release, in particular whether it is smooth or erratic. Body waves from large earthquakes often suggest a complicated pattern of energy release. (Vesanen, 1942; Usami, 1956; Richter, 1958; Miyamura et al, 1964; Bath, 1965.) In this study the P-wave portion of seismograms from the Alaskan earthquake of 28 March 1964 are studied in detail and interpreted in terms of a multiple source in order to better understand the nature of energy release during large earthquakes.

Data

Seismograms from low magnification instruments at 70 stations were collected. The instrument types used were Wiechert, JMA 59, WWNSS, Milne-Shaw and Galitzin. The stations covered a wide range of azimuths and distances ranging from 40° to 90°. The azimuth distribution, however, was not even since stations are concentrated in Europe, North and South America, and Japan. Figure 40 shows records from stations in Europe, Mexico, and Japan. Arrows point out 6 of the most outstanding phases. These phases do not correspond to any of the phases predicted by standard

travel-time curves. The amplitude of the first arrival is much smaller than that of the following phases. The average body wave magnitude corresponding to the very first P-pulse determined from WWNSS stations, is 6.6. Phases with successively larger amplitudes follow the first event. The magnitude determined for the largest amplitudes in the P-wave train, occurring about 60 seconds after the first arrival is 7.8. This value agrees approximately with the corresponding magnitudes determined from surface waves (7.7) using the conversion formula between surface wave magnitude and body wave magnitude given by Richter (1958). The character of the first two minutes of the seismograms cannot be explained by either second arrivals of a simple point source or a simple smoothly propagating rupture. Therefore, a more complex source is necessary and the records suggest that the source might be approximated by a series of point sources distributed in space and time.

Analysis

In order to establish the distribution of events for the multiple point-source approximation, all outstanding phases in the first two minutes of the seismograms were read. For each station a list of time lags with respect to the first arrival resulted. The criteria for picking a time lag were a sudden

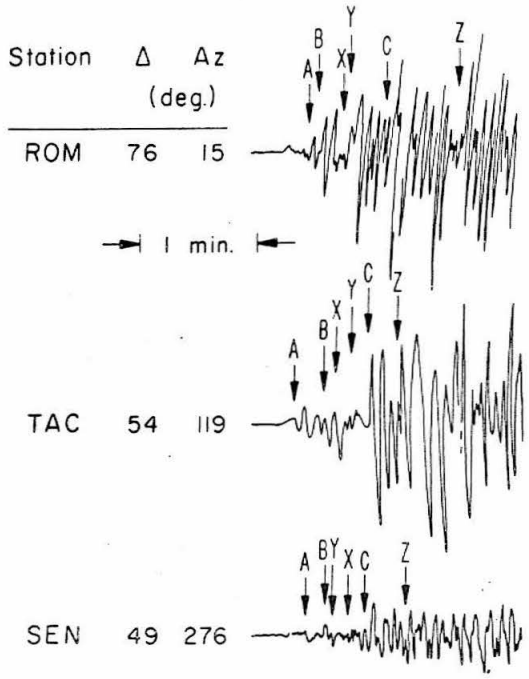

FIG. 40 *P*-wave portion of seismograms from Europe, Mexico and Japan. Arrows point out the phases attributed to the six determined events. The table on the right gives the time-lags of the phases with respect to the first arrivals.

Wyss and Brune (1967)

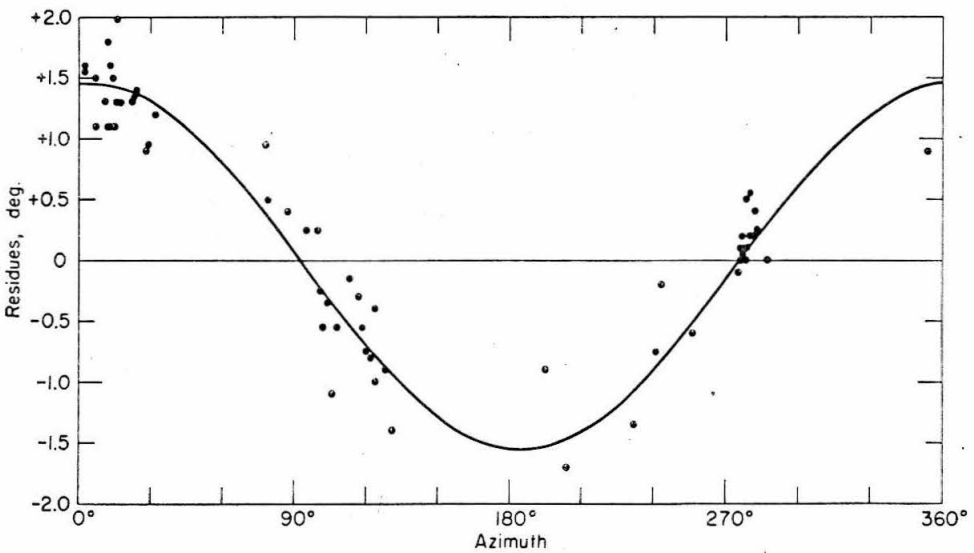

FIG. 41 Sine-curve plot for the location of event C. Standard deviation 22 km.

Wyss and Brune (1967)

substantial increase in amplitude and an abrupt change in phase. The stations were ordered in azimuth for comparison of their time lag sequences. The largest and most obvious pulse, event C on Figure 40, could be identified and correlated between the stations of different azimuth without difficulty. The other pulses were harder to correlate. The time lag with which they appear on the records is a function not only of source time and position differences, but also of the azimuth and distance of the stations. In order to aid in further correlation a model of a propagating rupture spreading out in a horizontal plane with a velocity of 3.3 km/sec was assumed. A tentative correlation was then made by computing the approximate distance from the initial epicenter under these assumptions. The approximate distance is given by:

$$\Delta_i = \frac{t_i}{\frac{1}{\beta} + \cos(\theta - \phi)\frac{dp}{d\Delta}}$$

t_i = seconds after first arrival, read from the seismograms,

β = propagating velocity of rupture, assumed,

$\frac{dp}{d\Delta}$ = slope of travel-time curve,

θ = azimuth from the initial epicenter to station,

ϕ = azimuth from the event to initial epicenter, parameter.

The distances Δ_i were computed from the time lags of several stations at different azimuths and distances, under variation of the parameter ϕ, the propagation direction. For different ϕ, different combinations of time lags could give more or less concordant results for the distance Δ_i. For combinations of time lags that were concordant, relocation of the epicenters of the corresponding events using the Gutenberg sine-curve method, was carried out with all available readings. In Figure 41 the distance residues for the location of event C are plotted as a function of azimuth. The reliability of certain combinations of time lags is indicated by the scattering of the residues of the Gutenberg sine-curve method. Incorrect combinations made it impossible to fit a sine-curve. After detailed analysis of the records, using the above described procedure, 6 events denoted by A, B, C, X, Y, and Z were identified; they are shown in Figure 42. Epicenters for the events A, B, and C are well established for the following reasons: (1) The standard deviation for the sine-curve fit is small; (2) These events are represented by conspicuous pulses on 90 to 95 percent of the analyzed records; (3) Their locations lie within the zone of aftershocks; and (4) The delay times from the initial epicenter give quite reasonable rupture velocities, about 3.5 km/sec.

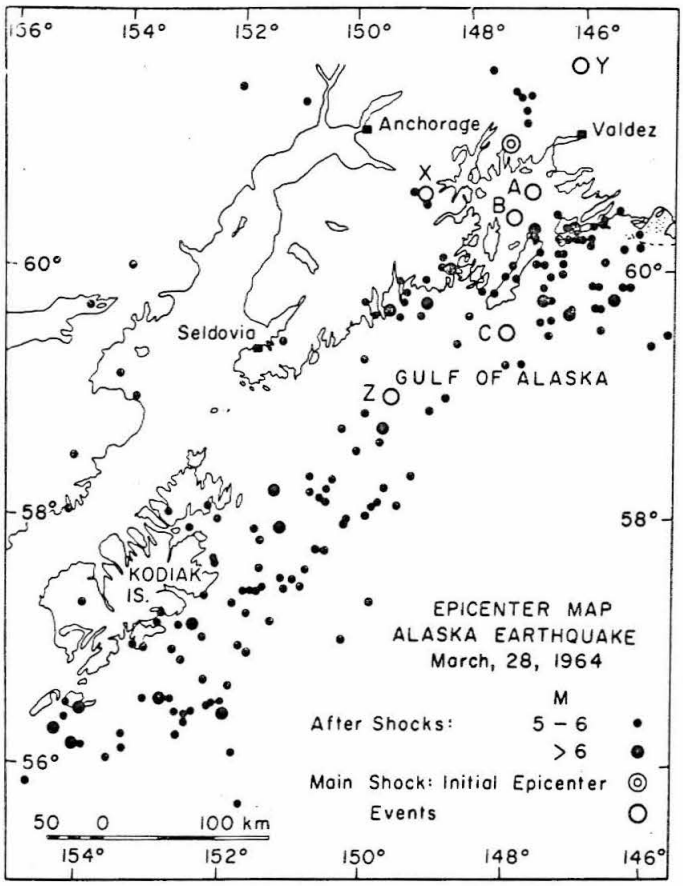

FIG. 42 Epicenter map showing locations of six events A, B, C, X, Y and Z. Aftershocks according to Algermissen (1966).

Wyss and Brune (1967).

The events X, Y, and Z are presented here as possible additional events with a somewhat lower degree of confidence. They could be identified on 60 to 75 percent of the analyzed records. Because of the very high amplitudes and the complexity of the signal, no further events could be established beyond 80 sec after the first

arrival, although they very probably occurred.

Discussion

The preceding analysis has indicated that the energy release during the Alaskan earthquake was characterized by more or less distinct high amplitude bursts or events, possibly superimposed on a smaller continuous level of energy release associated with a propagating wave and/or rupture. This is consistent with Haskell's (1964) conclusion that large earthquakes must have erratic source-time functions since a simple moving source does not radiate as much short-period energy as is observed. The events could represent consecutive bifurcation points caused by the rupture velocity accelerating to a limiting value as suggested by Mansinha (1964). If his calculations would apply for the studied earthquake, the velocity of transverse waves in the source region would be obtained by dividing the rupture velocity of 3.5 km/sec by a factor of about 0.7. The resulting transverse wave velocity of 5.0 km/sec would indicate that the source region is to be placed in the upper mantle rather than the crust. The aftershocks, on the other hand, occurred at an average depth of 22 km and our study appears to be consistent with the thrust fault model put forward

by Plafker (1965) and Savage and Hastie (1966). This raises the question as to whether event C represents a breakout-phase (Savage, 1965). A fault plane dipping 9°NW and having a depth of

Table 10

Rupture Propagation Velocity

Event	Time lag [sec]	Distance to initial event [km]	V [km/sec]
A	9	35	3.9
B	19	66	3.5
C	44	165	3.8
X	28	89	3.1
Y	29	93	3.2
Z	72	250	3.5

Average propagation velocity: $\overline{V}$ = 3.5 km/sec.

about 22 km at the original epicenter would intersect the surface in the region of event C. The resulting difference in depth of event C with respect to the original epicenter, 20 km, leads to a

decrease of the time delay as determined from the time lags on the seismic records. The distance from the original epicenter remains in first order the same, so the rupture velocity deduced from event C is then increased to about 4 km/sec. Alternatively, event C may be a stopping phase representing the end of the southward rupture.

The sequence of events started out from the initial epicenter location. During the first 44 seconds, events apparently occurred at various azimuths. Event Y perhaps represents a stopping phase for the northerly direction of propagation. After event C the sequence continued 600 km in a southwesterly direction to the south tip of Kodiak Island. The last event that could be identified, event Z, lies 250 km from the initial rupture and occurred 72 sec later (Figure 42). Later events probably occurred southwest of the event Z, but could not be identified because of the complexity of the seismograms.

The standard deviation of the distance residues for the Gutenberg sine-curve location of the epicenters was 0.2 degrees (22 km). Considering the complexity of the analyzed records, this standard deviation is quite satisfacotry. The locations and time lags give velocities between 3.1 and 3.9 km/sec for a disturbance radiating from the origin and triggering events (Table 10). The average southwesterly component of the propagation velocity is about

3.2 km/sec and thus the velocities determined in this manner agree approximately with those determined from the directivity of the surface wave radiation pattern for this earthquake (Furumoto, 1965). The values of the rupture velocity can be varied somewhat if variations in depth relative to the first shock are allowed.

The pulses representing events A, B, and C on the records are compared to the initial pulse in the average 6, 12, and 30 times larger respectively, corresponding to a magnitude increase from approximately 6.6 to 7.8. In Figure 42 it appears that the events are not surrounded by aftershocks in their immediate vicinity. This suggests that the strain was released in the vicinity of the events so that there was no strain-energy left for aftershocks.

DISPLACEMENTS ON THE IMPERIAL, SUPERSTITION HILLS, AND SAN ANDREAS FAULTS CAUSED BY THE BORREGO MOUNTAIN EARTHQUAKE OF 9 APRIL 1968

Introduction

The Borrego Mountain earthquake of 9 April 1968 (magnitude 6.5) was associated not only with a conspicuous surface break in its source region along the Coyote Creek fault (Clark et al, 1970), but also with displacements far outside the epicentral region along three major faults in the Imperial Valley region to the east and southeast of the epicenter (Figure 43). The Imperial, Superstition Hills, and San Andreas[1] faults broke along segments of at least 22, 23, and 30 km length, respectively, at distances of 70, 45, and 50 km from the epicenter. Remeasurements of several small-scale geodetic networks as well as observations of en-echelon

[1]The branch of the San Andreas fault system northeast of the Salton Sea has sometimes been called the Banning-Mission Creek fault because it represents the combined Banning and Mission Creek faults southeast of their point of coalescence near Indio, and because of this fault's debatable continuity with the San Andreas fault farther north. The name San Andreas is used herein for the sake of brevity and in keeping with U.S. Geological Survey usage.

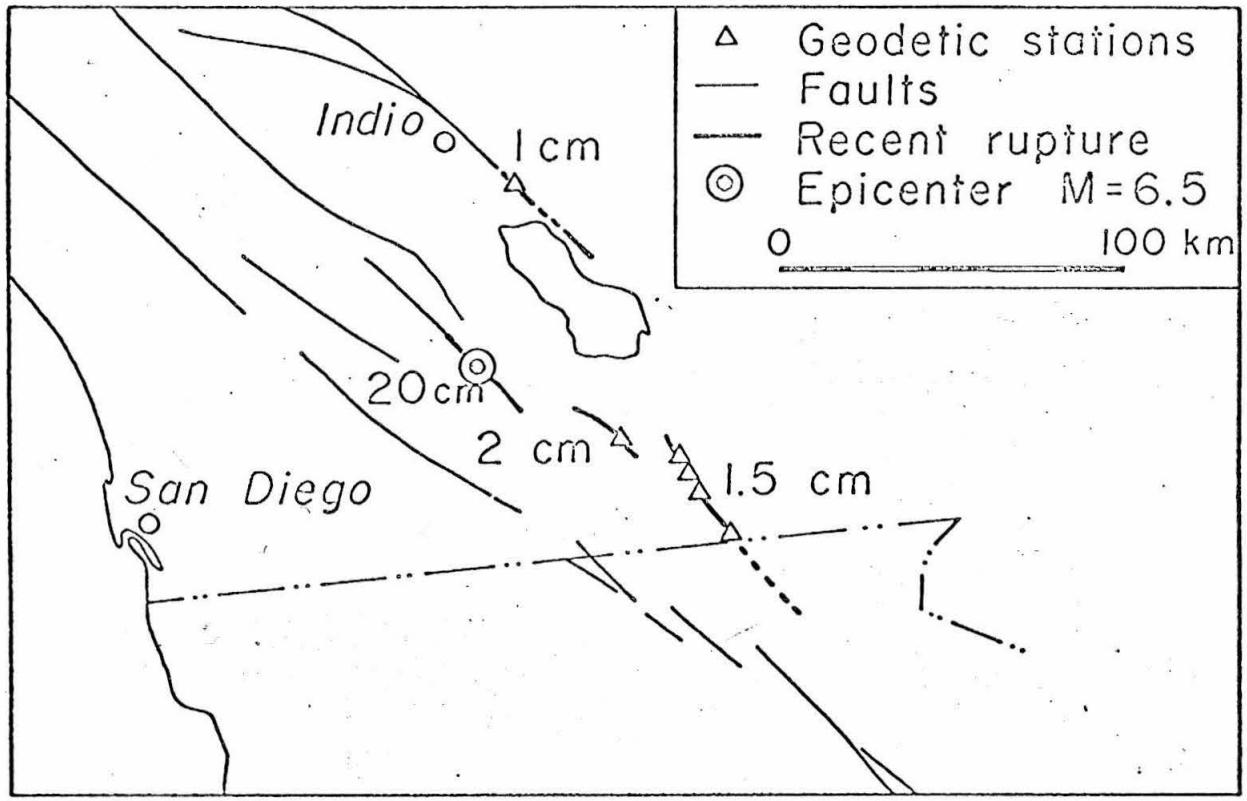

Figure 43. Map of Southern California showing displacements associated with the Borrego Mountain earthquake.

cracking showed that right-lateral displacements of 1 to 2 cm had occurred on these three distant faults. This is the first documented case of an earthquake apparently causing fault displacements well outside the epicentral region. Something similar may have happened along a segment of the Garlock fault as a result of the 1952 Kern County earthquake on the White Wolf fault (Buwalda and St. Amand, 1955, p. 53), but the Garlock fault is relatively close to the White Wolf fault and was almost within the zone of aftershock activity.

In this study, we argue that the displacements on the Imperial, Superstition Hills, and San Andreas faults were, in fact, caused by the seismic shaking of the distant Borrego Mountain earthquake, and that these displacements were not associated with normal aftershocks, and that they were not caused by the change in the regional static strain field caused by the fault displacements of the Borrego Mountain earthquake.

OBSERVATIONS

Imperial Fault

Although a number of auxilliary faults near Borrego Mountain were examined for possible surface displacements on the day following the 9 April earthquake, the Imperial fault -- 70 km distant -- was not visited until 13 April. At that time Wyss and

Mr. Robert D. Nason noticed fresh en-echelon cracks at Highway 80 suggesting at least 1/3 cm of right-lateral displacement. It was this discovery that then stimulated the careful examination of other distant faults and led to the subsequent documentation of surface displacements on the Superstition Hills and San Andreas faults, as well as at other localities along the Imperial fault.

Because of the unusual fault displacement along the Imperial fault in March, 1966 (Brune and Allen, 1967a), and the suspicion that creep might be occurring along this and related faults, Brune and Allen in 1966 and 1967 had established a series of small geodetic networks that straddled the Imperial, Superstition Hills, and San Andreas faults. These networks, each comprising a single theodolite station and 5 to 10 markers within a few hundred meters on both sides of the fault trace, were patterned on the similar networks that had earlier been established across the San Andreas fault near Parkfield (Chapter I). The locations of these stations are shown in Figure 43, and their coordinates are given in Table 11.

Figure 44 shows that about 1.5 cm of right-lateral displacement took place along the Imperial fault at Highway 80 between 5 January 1968 and 19 April 1968, and evidence is presented in a later section to indicate that this displacement took place at about

Table 11

Small Scale Geodetic Networks

Fault	Station	Coordinates	
Coyote Creek	Ocotillo Wells	33° 08' 36"	116° 07' 47"
Superstition Hills	Imler Creep Meter	32° 55' 37"	115° 41' 48"
Imperial	Harris Rd.	32° 53' 00"	115° 33' 18"
	Workington Rd.	32° 50' 51"	115° 30' 41"
	Melowland	32° 48' 15"	115° 27' 58"
	All American Canal	32° 40' 34"	115° 41' 31"
Banning-Mission Creek (San Andreas)	Thermal	33° 37' 32"	116° 02' 53"
	Bertram	33° 24' 33"	115° 47' 08"

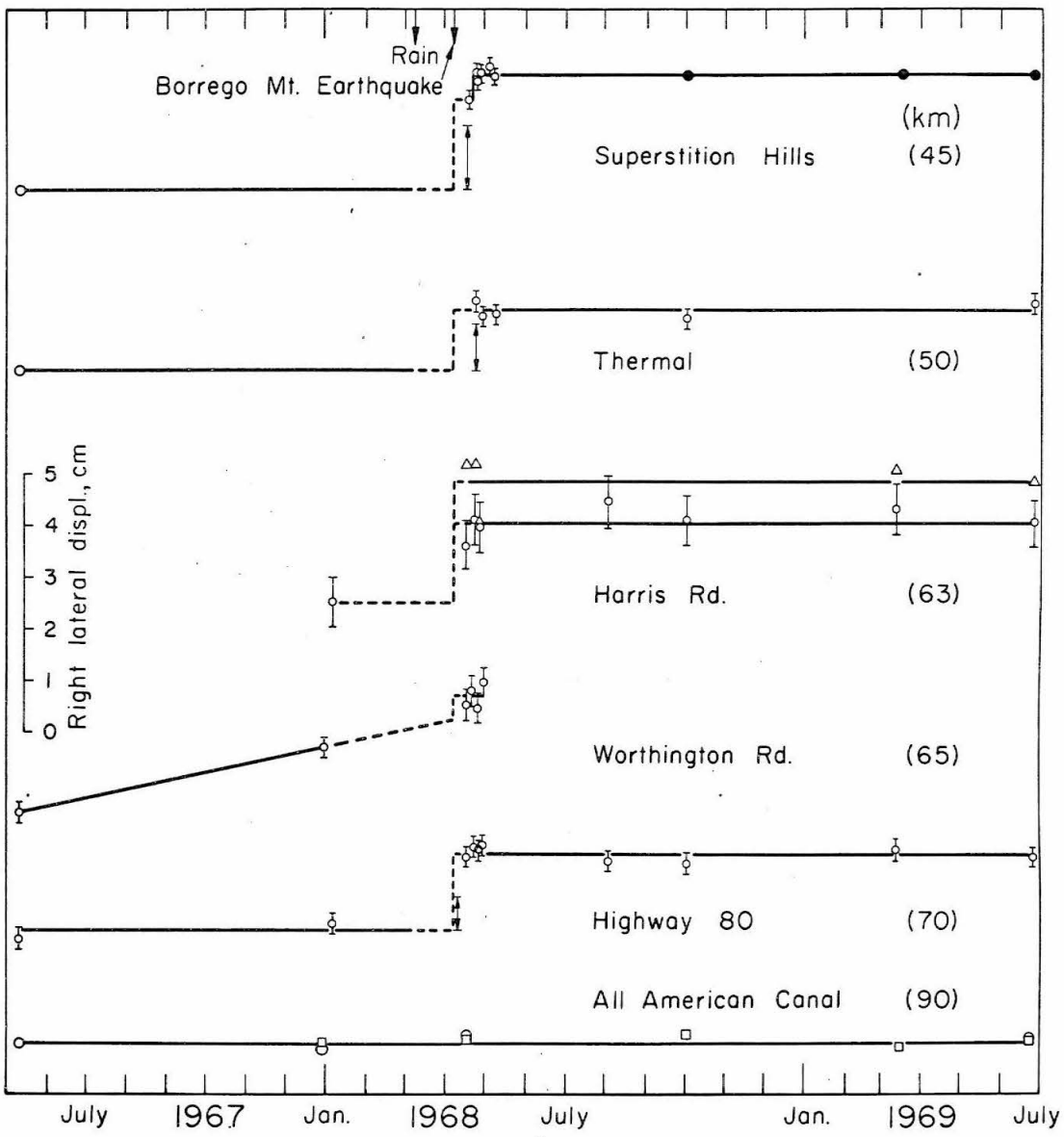

Figure 44. Displacement history of small-scale geodetic networks straddling active faults in the Imperial Valley, Calif.

the time of the Borrego Mountain earthquake, and not as creep distributed throughout the three-month interval. Three additional goedetic networks had been established along the Imperial fault prior to the earthquake (Figures 43, 44), and all but the southernmost network showed clear evidence of fault displacement at about the time of the earthquake.

The geodetic observations were supported by field evidence of surface faulting along more than 22 km of the Imperial fault, extending distinctly farther both to the north and south than the 10 km segment broken during the 1966 shock (Brune and Allen, 1967a). For a more detailed discussion see Allen et al (1970).

Superstition Hills Fault

On 11 May 1967 Allen and Brune had established a small geodetic network across the Superstition Hills fault where it crosses Imler Road (Figure 43), and reoccupation of this station on 19 April 1968, 10 days after the Borrego Mountain earthquake, revealed about 2cm of right-lateral displacement (Figure 44). At the same time, fresh en-echelon cracks showing up to 1.5 cm of right-lateral displacement were discovered along the Quaternary fault trace in the same vicinity. On 25 April, these cracks were

followed northwest for about 8 km along the fault trace, and on 5 May Grantz and Wyss mapped the entire broken zone, extending for 23 km (Allen et al, 1970).

When the cracks were first observed on 19 April, they were relatively fresh-appearing, but by the time mapping was completed on 7 May, wind-blown sand had already obscured much of the fault trace. We conclude that the cracks could not have come into existence long before 19 April, and their origin in association with the Borrego Mountain earthquake on 9 April seems highly probable. Because of suspicion that creep might be taking place on this fault following the earhquake, a creep meter was installed across the fault on 7 May. A continuous recorder registered the displacement as measured by a 10 meter taut invar wire, similar to an instrument previously used at Parkfield (Smith and Wyss, 1968). Neither the subsequent observations of the creep meter nor resurveys of the geodetic network have revealed any suggestion of creep along the fault, thus giving further support to the inference that the observed displacement occurred suddenly during the Borrego Mountain earthquake.

Like the Imperial fault, little is known about the possible extent, if any, of the Superstition Hills fault beyond the segment broken in 1968. On the southeast, the1968 fractures ended about

1 km north of Edgar Road, at very nearly the same point that the Quaternary trace disappears as observed on aerial photographs and in the field. Likewise, the fractures continued northwest only about as far as the mapped trace of the Quaternary fault (Dibblee, 1954; unpublished). The Superstition Hills fault, together with the Superstition Mountain fault, appear to be branches of the San Jacinto fault zone, and if projected still farther northwest, they would join on about the Coyote Creek fault -- also a branch of the San Jacinto zone -- on which the Borrego Mountain earthquake occurred.

San Andreas Fault

In February of 1967, Dr. Arthur Sylvester (personal communication) had pointed out fresh cracks along the trace of the San Andreas fault in the Mecca Hills north of the Salton Sea; they were particularly evident in the 4-km segment between Painted Canyon and Red Canyon (the unlabelled canyon at the bottom of the Thermal Canyon 1:24,000 U.S.G.S. Quadrangle map). Although we were not convinced at that time that the cracks necessarily reflected tectonic movements, we decided to check this possibility by establishing a small geodetic network across the fault in Red Canyon (Figures 43, 44; Table 11). This is a segment of the

San Andreas fault zone along which there has been very little historic seismicity (Allen et al, 1965) or micro-earthquake activity (Brune and Allen, 1967b), but remarkably fresh-appearing scarplets up to 1/2 meter in height are abundant along the fault here. When this area was first visited following the Borrego Mountain earthquake, on 24 April, fresh en-echelon cracks were observed at the base of the scarplets, and at several other localities along the fault trace. Wallace and Wyss subsequently mapped the fresh break for more than 30 km from near Bertram on the south to Thermal Canyon on the north (Allen et al, 1970) although it is significant that surface fracturing was by no means continuous throughout the 30-km segment. The average right-lateral displacement was estimated to be between 0.5 and 1.0 cm. Resurvey of the Red Canyon geodetic network of 24 April indicated 1.2 cm of right-lateral displacement subsequent to the establishment of the station on 11 May 1967, and there has been no significant change since (Figure 44). A second geodetic network was established across the fault near Bertram on 5 May 1968, and it likewise has shown no subsequent change.

Description of the Surface Displacements

The typical style of displacement along the Imperial, Superstition Hills, and San Andreas faults was that of overlapping en-echelon cracks oriented so as to clearly indicate right-lateral displacement. Individual cracks rarely gaped more than a few millimeters, and individual en-echelon breaks were typically less than a meter long. The width of the fractured zone seldom exceeded one meter and was generally much less. The fractures showed up not only in undisturbed soil, but also in asphalt roads that were crossed by each of the three faults. All the broken sections of the Superstition Hills and San Andreas faults were traversed in their entirety by the author. This was not possible along the Imperial fault because of intensive cultivation of most of the area; instead, each road and canal crossing was checked.

The newly formed fractures along the three distant faults were such minor features that they would easily have escaped detection if we had not specifically looked for them, and if we had not known from other geologic evidence the exact locations of the active fault traces to within a very few meters.

Seldom have such well-defined faults been examined in such great detail following a major nearby earthquake, and we suspect

that although this may be the first documentation of fault displacements caused by seismic shaking, the same phenomenon has happened many times before, not only here, but on other active faults in similar tectonic environments as well.

Other Faults

At the same time that fresh displacements were being discovered on the Imperial, Superstition Hills, and San Andreas faults, a number of other faults in the region were carefully checked in the field and found to have no evidence of surface displacements. These include the Superstition Mountain fault, Elsinore fault, Earthquake Valley fault, San Felipe fault, and branches of the San Jacinto fault system north of Borrego Valley. One feature that distinguishes these faults is that they are predominantly in crystalline rocks, whereas parts of the three faults that moved are all in deep alluvium or late Cenozoic sediments. The estimated minimum distance to crystalline basement, based on seismic work by Kovach et al (1962) and Biehler et al (1964), is 3500 meters along the Superstition Hills fault, 6000 meters along the Imperial fault, and perhaps 2000 meters along the San Andreas fault. It is also probably significant that the only three faults in southeastern

California for which we had some evidence of slippage before the earthquake (and had therefore been straddled with small geodetic networks) were the same three faults that moved during the Borrego Mountain earthquake.

MECHANISM

Did the Borrego Mountain Earthquake Cause the Displacements on The Distant Faults?

Displacements on the Imperial, Superstition Hills, and San Andreas faults were not noticed until at least four days following the Borrego Mountain earthquake, and none of these faults had been field-checked for several months prior to the earthquake. Time spans at least as great apply to the geodetic measurements (Figure 44). What, then, is the evidence that the observed displacements took place in association with the Borrego Mountain earthquake and not as gradual creep over a period of several months, or perhaps as separate disconnected events?

Three lines of evidence lead us to believe that the observed fault displacements indeed took place on or about 9 April 1968: (1) The geodetic measurements that were made during the year before and during the year following the earthquake indicate little or no creep, except at Worthington Road. It thus seems unlikely

that creep should have, by accident, characterized only the short interval that included the earthquake. (2) On 8 March 1968, one month before the earthquake, a heavy and unusual rainstorm brought approximately 5 cm of precipitation to the entire Imperial Valley-Coachella Valley area, causing considerable runoff and local flooding. There can be no question whatsoever that all of the fresh cracks that were observed following the earthquake originated after this rainstorm. (3) Blowing dust and sand are characteristic of the entire region, and everyone who studied the displacements on these three faults, as well as the main break near Ocotillo Wells, was impressed with the rate at which fresh features disappeared. Within two weeks following the earthquake, many of the cracks along the main break had become barely recognizable because of blowing sand. It is our judgment, based on field experience in this area, that the fractures first observed between 13 April and 24 April must have come into existence during the first two weeks in April. Particularly, along the Imperial fault the fresh cracks in powdery alluvium that were first observed on 13 April must have originated within the preceding few days. It seems to us to be a reasonable and highly likely conclusion that all of the fractures came into existence at the approximate time of the Borrego Mountain earthquake on 9 April.

Static or Dynamic Strain?

If the hypothesis is accepted that the breaks on the Imperial, Superstition Hills, and San Andreas faults were caused by the Borrego Mountain earthquake, the important question still remains as to whether the displacements were caused by the dynamic strain associated with the shaking, or by the static strain associated with the main fault break. The static strain is the permanent strain field caused by the 33 km long break on the Coyote Creek fault; the dynamic strain is the transitory strain associated with the seismic waves generated by the earthquake.

For an estimate of the static strain, we use Press's (1965) results. The length of the surface break is taken as 33 km, and the hypocentral depth now assigned by Pasadena is 14 km. For an upper limit of the static strain at distance, we therefore use Press's case in which L = D, and the far-field strains were calculated by scaling down Press's figures to correspond to an average fault displacement of 30 cm. The resulting static strains at distances of 45, 70, and 50 km in the directions of the Superstition Hills, Imperial, and San Andreas faults are 4×10^{-7}, 1×10^{-7}, and -3×10^{-7} respectively, assuming these faults to be parallel to the Coyote Creek fault. The minus sign in the case of the Banning-Mission

Creek fault indicates that the residual static strain induced by the Coyote Creek fault displacement was left-lateral.*

The dynamic strain caused by S waves with approximately 4.3 sec period, recorded at El Centro (near the Imperial fault), was about 1.1×10^{-5} (corresponding to a trace amplitude of 4.9 cm at a period of 4.3 sec on the strong motion Wood-Anderson instruments). This is two orders of magnitude larger than the static strain at this distance. This fact, in addition to the pursuasive argument that the static strain would have led to the opposite sense of displacement on the San Andreas fault, makes it highly probable that the dynamic strains ratherthan the static strain induced the observed ruptures on the distant faults.

Sudden Displacement or Creep?

Even granting that the dynamic strains caused the displacements, the question remains as to whether these displacements took place suddenly or during a period of creep lasting several minutes, hours, or days. After the distant displacements were first noticed, geodetic measurements were repeated at closely spaced intervals to determine if creep was perhaps still taking place (Figure 44), and it appears that within the accuracy of the measurements, no creep was occurring at this time on any of the three distant faults.

*This fact was originally pointed out by Dr. John McGinley

The sensitive creep meter installed at Superstition Hills further substantiates this conclusion. Thus, if displacements occurred during a period of creep following the earthquake, this period must have been shorter than five days.

On the other hand, if any of the three distant breaks had occurred as sudden rupture, seismic waves would have been radiated. Inasmuch as the seismographic records of most southern California stations were off-scale for several minutes following the Borrego Mountain earthquake, we cannot state with assurance that earthquakes did not occur at the three distant localities immediately following the main event, although it seems unlikely that the magnitudes of such events could have exceeded 4.5 without being detected. However, three lines of evidence suggest that such sudden displacements -- if they did occur -- were not in any sense "normal" earthquakes: (1) The fault lengths of 22, 23, and 30 km are much longer than could typically be associated with earthquakes of magnitude less than 4.5 (Chapter II). (2) Only very few possible aftershocks could be associated with the three distant faults, in sharp contrast to the usual high aftershock activity accompanying

fault breaks of this length. Despite a careful search of seismic records from several stations close to the distant faults, including temporary stations within the Imperial Valley at Obsidian Butte and near Westmoreland, only six small shocks could be found that might possibly have been associated with the Superstition Hills fault within a month following the earthquake, one small shock that might have been associated with the Imperial fault, and none in the area of the San Andreas fault. A particular search was made of the Hayfield records for events with short S-P intervals, inasmuch as the San Andreas fault is much closer to this station than to the Coyote Creek fault, near which the principal aftershock activity occurred.

The absence of aftershocks in the vicinities of the distant faults is substantiated by micro-earthquake surveys in two of these areas by Mr. Walter Arabasz on 20-21 April. Using a backpack instrument recording on smoked paper, and operating at a magnification of 100,000 at 20 cps, thirteen hours of continuous recording at the Imperial fault near the south end of the fractured segment revealed no nearby microearthquakes. Similar but shorter periods of recording farther north along the Imperial fault and in a granite quarry at Superstition Mountain (5 km from the Superstition Hills faults) likewise revealed little or no

micro-earthquake activity.

(3) Another obvious peculiarity of these displacements is the unusually low ratio of average offset to length of rupture. For most earthquakes when the faulting length is about 20 to 30 km the average offset is about 10 to 100 cm, whereas, the average offsets observed here are only 1 to 2 cm. In addition, it appears that the breaks may not have been continuous on the San Andreas and Imperial faults.

We conclude that the displacements on the three distant faults occurred rapidly, but with a mechanism of strain release different from that of typical earthquakes associated with fault breaks of these lengths, and that this relatively rapid motion commenced with the arrival of the first intense seismic energy from the Borrego Mountain earthquake, and that it probably lasted at most only as long as the strong shaking persisted. The displacements were probably caused by strong seismic shaking, and this is a mechanism of strain release on active faults not previously documented, although some of the observations at Parkfield described in the first chapter and by Smith and Wyss (1968), could be explained in the same way. Evison (1963) argued that surface fault displacements should typically be regarded as "a gross form of earthquake damage,"

caused by some unspecified deeper source of shaking. We agree that the movements on the Imperial, Superstition Hills, and San Andreas faults were caused by an independent source of shaking -- the Borrego Mountain earthquake -- but we reject Evison's hypothesis that this is the normal mechanism of strain release along faults.

Many aspects of the mechanics of displacements on the three distant faults remain unexplained. We assume that elastic strain was released by the displacements, but the depth at which this elastic strain had accumulated is problematical. An attractive but unproved hypothesis is that creep is taking place continually at depth along these three faults, partly reflecting the unusual semi-oceanic crust and complex fault pattern of the region (Allen, 1968); elastic strain is visualized to accumulate only in the overlying thick section of indurated sedimentary rocks, to be relieved intermittently either by episodic creep, by very shallow small earthquakes such as the Imperial earthquake of 1966 (Brune and Allen, 1967a), or by externally caused shaking such as that of 1968. Another unanswered question is: what determined the amount of displacement on the three distant faults? In the first chapter it was argued that the amount of episodic creep displacement is not a function of the nature of the instigating event, but instead is related to the stress-drop between a constant rupture

stress and a constant frictional stress on the fault. Had the tectonic stress accumulated to a critical value, the creep presumably would have started even without being instigated by the earthquake. On the other hand, field evidence might suggest that the total displacements on the three distant faults may have been at least partly a function of the strength of shaking; the larger displacement on the Superstition Hills fault as compared to the Imperial fault may be an indication not of higher stress accumulation, but may be partly due to the stronger shaking closer to the source.

Stress Drops

In order to estimate the stress drops associated with the displacements on the distant faults, a fault depth must be assumed. We arbitrarily assume a depth of 4 km, equal to about half the thickness of the sedimentary section in the center of the Imperial Valley (Biehler et al, 1964), and corresponding to the depth of transition between stable sliding and stick-slip in the Parkfield model of Scholz et al (1969). Assuming an average displacement of 1.5 cm, this corresponds to a stress drop of 0.5 bar -- close to (one-half) the value obtained by Brune and Allen (1967a) for the Imperial earthquake of 1966.

"Triggering"?

We have chosen to avoid use of the word "trigger" in connection with the movements on the Imperial, Superstition Hills, and San Andreas faults, because this would imply that the displacements were instigated by much smaller phenomena than the displacements themselves. As was indicated in the previous section, the maximum dynamic strain at El Centro was about 1.5×10^{-5}. Assuming a fault depth of 4 km and an average displacement of 1.5 cm on the nearby Imperial fault, the calculated strain associated with the displacement was only 2.5×10^{-6}. Thus, although there is no question in our minds that the Borrego Mountain earthquake caused the distant fault displacements, we do not feel that use of the word "trigger" is appropriate, notwithstanding an earlier use of this word in our preliminary report on the events (Allen et al, 1968). By way of contrast, a true example of seismic triggering might be the multiple ruptures of the Alaska earthquake, where small events apparently triggered larger succeeding events.

CONCLUSIONS

The Alaskan earthquake of 28 March 1964 ruptured in a series of events. Such a mechanism may be the mode of rupture for many large earthquakes. The body wave magnitude of the initial

event was 6.6 and it triggered the sequence which grew into one of the largest earthquakes of this century. The rupture propagated initially in various azimuthal directions, but after a time of about 44 sec continued only in a southwesterly direction. The average inferred rupture velocity was 3.5 km/sec. The amount of energy represented by discrete events is much greater than the energy which can be attributed to continuous radiation.

The Borrego Mountain earthquake caused ruptures of 1 to 2 cm along large segments of three tectonically active faults outside the source region. These ruptures occurred only on faults and portions of faults where evidence for recent Quaternary fault activity was evident. It is inferred that the displacements constituted local tectonic strain release and were made possible by the dynamic strain field associated with the Borrego Mountain earthquake. This mechanism of strain release is termed seismic shaking.

Even though seismic triggering and seismic shaking were demonstrated only to have occurred for two events it is most likely that these mechanisms of strain release occur quite frequently. Another example of a complex rupture was described just recently by Trifunac and Brune (1970). It is possible that these mechanisms are also associated with very small earthquakes as was suggested in chapter II.

Chapter IV

SEISMIC MOMENT, STRESS, AND SOURCE DIMENSIONS AS A FUNCTION OF DEPTH IN A DEEP SEISMIC ZONE, AND COMPARISON WITH EARTHQUAKES ON OCEANIC RISES

Abstract

The amplitude spectra of long-period mantle and body waves were used to calculate seismic moments for a total of 103 earthquakes. Thirty-seven were associated with the South American trench system, fourteen earthquakes were located in the Aleutians, and twenty earthquakes which originated on oceanic ridges. The rest of the analyzed events were located in various seismic zones. Seismic energies of these earthquakes were estimated from the spectral densities of short-period P-waves and also from the Gutenberg energy-magnitude relation. The apparent average stress (efficiency times average stress) in the source region was obtained from the ratio of energy to moment. The apparent average stress is a lower bound for the actual average stress. Near the surface a mean value for the apparent average stress is approximately 20 bars for ridges as well as for trenches.

This may indicate that the strength of the materials and the rupture mechanism in the two types of source regions are the same. In South America the mean value of the apparent stress for depths between 45 km and 150 km is 270 bars. Around 600 km depth the mean value is very similar to that at the surface, 18 bars. Differences in apparent average stress most likely reflect differences in strength of the material in the source region. The pattern of strength versus depth can be explained by ocean floor consumption. As lithospheric material plunges underneath oceanic trenches it reaches higher pressures but is heated very slowly, and thus will have relatively high strength until the temperature rises enough to weaken it. Comparison of the apparent average stress with estimates of the stress drop indicate an upper bound of about 0.1 for the seismic efficiency of deep and intermediate earthquakes.

INTRODUCTION

In chapter II it was shown that there exist impressive differences in seismic signatures of different local earthquakes, and that these differences can be interpreted as differences in the stresses accumulated in the source region. The relative

stress in the source region of a teleseism is hard to guess by a casual look at the seismogram, because it is hard to take into account the effects of the epicentral distance. However, in magnitude determinations it sometimes happens that the long-period and surface wave magnitudes disagree with magnitudes based on short periods. Such discrepancies can be interpreted as an indication of unusually large or unusually small stresses.

Seismic signals are the only source of information for intermediate and deep earthquakes. For this reason the methods applied in chapter II for small earthquakes are the only tools that permit us to obtain source parameters for deep earthquakes. It would be of great interest to study on a world wide scale, the relative magnitude of the shear stresses causing earthquakes. One could detect regions of large stress accumulations and thus single out the regions most likely to produce large destructive earthquakes. The understanding of island arcs and the mechanism of consumption of oceanic lithosphere could possibly be greatly advanced by correlating relative stress levels with the detailed geometrical shape of oceanic trench-systems. In general, it would be interesting to relate a global stress pattern to the theory of ocean floor spreading and plate tectonics.

It is of particular interest to compare the apparent stresses of ocean floor creation sites with those of consumption sites, and to study possible changes in stresses, and strength, as a function of depth in deep seismic zones. This chapter is a start to such a global stress analysis. The South American and the Aleutian seismic zones were chosen for the study because when this work was started these two trench systems had the largest numbers of earthquakes with known fault plane solutions.

The apparent strains (stresses) were obtained from the ratio of the seismic energy to the seismic moment. The first average stress estimated in this way was obtained for the Niigata earthquake by Aki (1966) who pointed out the usefulness of the method for the study of deep earthquakes. The seismic energy E_s contained in frequencies between 0 and 1 cycles per second measured at teleseismic distances can be defined as the product of the seismic efficiency factor η with the total energy released by the dislocation

$$E_s(1) = \eta E. \qquad (23)$$

Dividing the seismic energy by the moment one obtains a quantity defined as the apparent average strain.

$$\frac{E_s}{M_o} = \eta\bar{\varepsilon} = \eta\frac{\bar{\sigma}}{\mu} \quad . \tag{24}$$

The apparent shear stress of the source region is obtained by multiplying the apparent shear strain by the shear modulus. The parts of the mantle where earthquakes occur must have different composition and different temperatures than the rest of the mantle. However, even by severe differences in these properties the shear modulus would not change more than about 10%. To compute the stress it is an adequate approximation to use the shear moduli for corresponding depths in the mantle given by Bullen (1963). The apparent average strains and stresses are a lower bound for the average strains and stresses.

Most of the seismically radiated energy is contained in the short period waves. For most earthquakes under magnitude seven, the energy represented by waves with periods longer than 5 sec is negligible compared to the energy associated with waves between 1 and 2 sec period. The seismic energy of an earthquake is a strong function of the amplitude at the short period end of the seismic spectrum. At long periods the spectral amplitudes of an earthquake tend to reach a constant value. The amplitude

level at the long period end of the spectrum is determined by the seismic moment. The ratio of high to low frequency spectral amplitude is a direct measure of the apparent strain in the source region. The apparent strain is the basic quantity determined in this study. Even though it is often more convenient to think in terms of apparent stress, one should remember that the basic measurements yield apparent strain. It should be emphasized at this point that the word "strain" (stress) in this study always means nonhydrostatic strain (stress).

Thus, studies of seismic spectra may lead to estimates of absolute stress, provided other parameters influencing the seismic spectrum can be properly evaluated. The correction factors for attenuation, instrument response, effects of the free surface, radiation pattern, and geometrical spreading were applied. The most uncertain parameter is the seismic efficiency. Berckhemer and Jacob (1968) have fitted seismic spectra to theoretical spectra of P-waves deducing the fault area and stress drop under the assumption of a rupture velocity. By comparison of the apparent stress with the stress drop, one can obtain a largest possible efficiency, since the initial stress had to be equal or larger than the stress drop. The ratios of apparent stress to

stress drop are approximately the same for earthquakes at intermediate and great depth. The fact that the maximal efficiency does not vary between intermediate and great depth could suggest that the efficiency also does not change with depth. The changes of apparent stress would then reflect directly changes of stress. The maximum of the apparent stresses occurs at depths of approximately 100 km. In the major parts of the South American deep seismic zone, the mean value of 10 earthquakes between 45 and 150 km is 270 bars. This value is an order of magnitude larger than the values at 0 and 600 km depth. If the apparent stresses are divided by the maximal seismic efficiency of 0.1 the stresses at 100 km depth are approximately 3 kbar in the average. The fault dimensions corresponding to these high stress earthquakes are extremely small, 2 to 7 km for earthquakes with body wave magnitude 7.0. Although it has not been possible to demonstrate conclusively that this result is not due to a variation of efficiency with depth, it is felt that most of the change of apparent average stress with depth is due to change of average stress with depth. If the variation of stress with depth is real it can be explained by the pressure-temperature environment to which a downgoing slab of lithosphere, as proposed by Isacks, Oliver, and Sykes (1968), is exposed to.

THE SOUTH AMERICAN SEISMIC ZONE

Fault Plane Solutions

For an accurate estimate of the seismic moment and the seismically radiated energy, the fault plane solution of an earthquake has to be known. Thirty-seven earthquakes associated with the South American shear zone were selected on the basis of location (Figure 45) and size as well as of the quality of existing fault plane solutions. The source of the fault plane solution is given in the last column of Table 12. The code is 1 = Stauder and Bollinger (1964), 2 = Stauder and Bollinger (1966), 3 = Wickens and Hodgson (1967), 4 = Khattri (1969), 5 = earthquakes for which the moment was obtained by Berckhemer and Jacob (1968), and 6 = Stauder (1970).

Moments

The equivalent double-couple seismic moment, as defined in the dislocation theory of faulting (Maruyama, 1963), was obtained from spectral densities observed at Pasadena. Where it was possible, the moment was determined from long period mantle waves as well as from long period P-waves. In the case of the mantle waves, the far-field displacement for a double-couple and the excitation

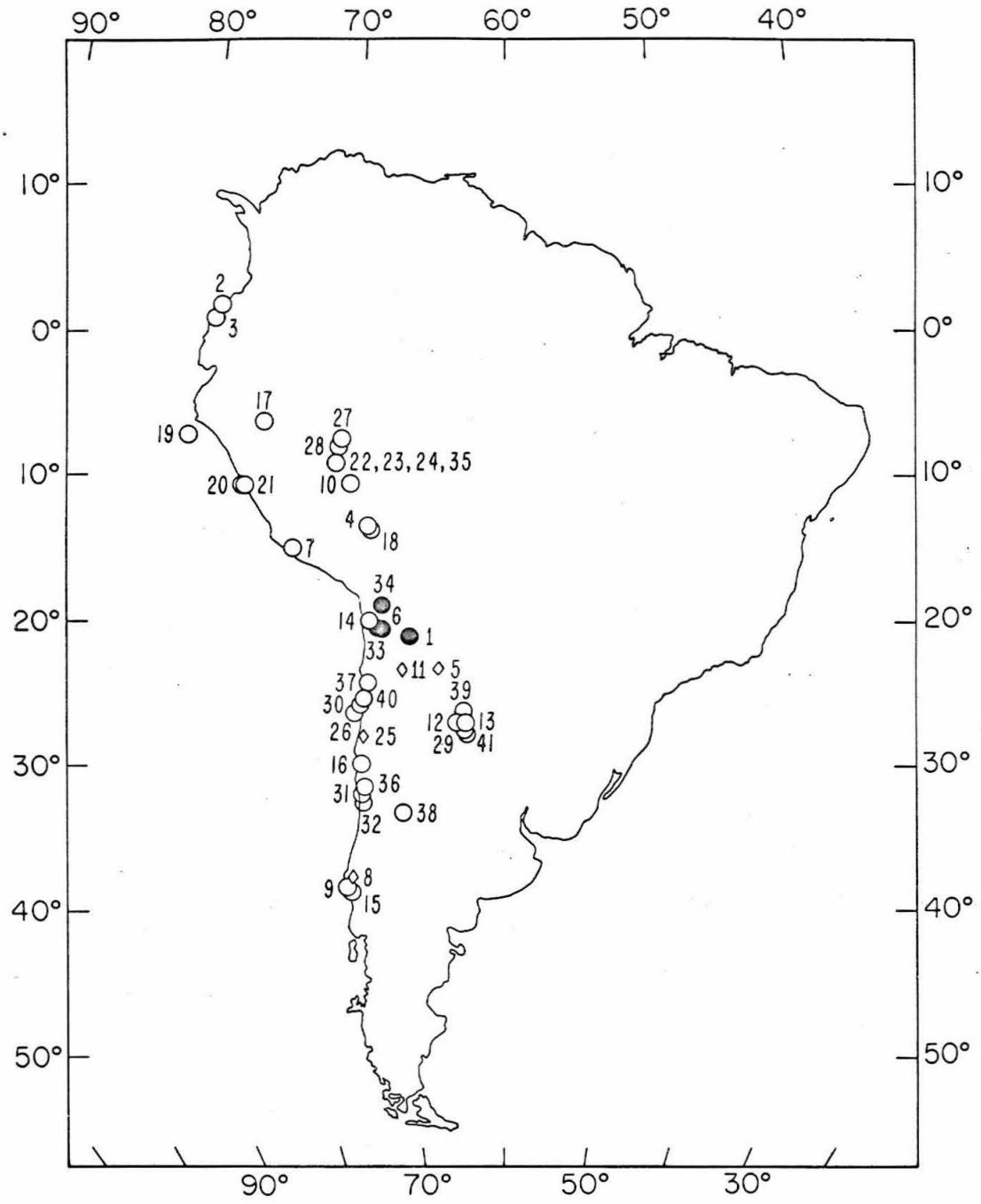

Figure 45. Map of South America showing epicenters of analyzed earthquakes.

Table 12

List of Earthquakes in South America

No.	Date d m y	Time h m s	Latitude S	Longitude W	Depth (km)	Fault Mechanism Source
1	29 11 57	22 19 41	21.0	67.0	190	3
2	01 02 58	16 10 15	- 1.7	79.3	0	3
3	14 04 58	21 32 28	- 1.0	79.5	0	3
4	26 07 58	17 37 13	13.5	69.5	630	3
5	12 05 59	09 46 55	23.2	65.0	26	3
6	14 06 59	00 12 02	20.4	69.0	83	3
7	15 01 60	09 30 19	15.0	75.0	70	3
8	22 05 60	10 32 43	37.5	73.0	0	7
9	20 06 60	02 01 09	38.2	72.8	0	3
10	31 08 61	01 48 39	10.4	70.7	605	3
11	03 08 62	08 56 12	23.2	67.5	71	1
12	29 09 62	15 17 48	27.0	63.6	575	6
13	08 12 62	21 27 18	27.0	63.0	620	6
14	29 12 62	10 41 04	20.0	69.9	46	1
15	05 02 63	20 39 22	38.4	73.2	41	2
16	10 03 63	10 51 48	29.9	71.2	70	2
17	13 04 63	02 20 58	6.2	76.5	125	2
18	15 08 63	17 25 06	13.8	69.3	543	2
19	29 08 63	15 30 31	7.1	81.6	23	2
20	17 09 63	05 54 34	10.6	78.2	61	2
21	24 09 63	16 30 16	10.6	78.0	80	2
22	09 11 63	21 15 30	9.0	71.5	575	2
23	10 11 63	01 00 39	9.2	71.5	600	2
24	11 11 63	19 54 09	9.1	71.4	585	5
25	25 07 64	19 31 07	27.9	70.9	26	6
26	18 08 64	04 44 58	26.4	71.5	8	6
27	28 11 64	16 41 33	7.7	71.2	626	5
28	28 11 64	16 49 30	8.0	71.4	655	5
29	09 12 64	13 35 42	27.5	63.2	580	6
30	23 02 65	22 11 50	25.7	70.5	40	6
31	22 03 65	22 56 26	31.9	71.5	80	6
32	28 03 65	16 33 16	32.4	71.3	72	6
33	12 06 65	18 50 12	20.5	69.3	102	6
34	20 08 65	09 42 49	18.9	69.0	128	6
35	03 11 65	01 39 03	9.1	71.4	590	4
36	10 04 66	16 36 14	31.5	71.2	64	6
37	27 07 66	04 48 59	24.2	70.3	35	6
38	10 11 66	03 02 32	31.9	68.4	120	6
39	20 12 66	12 26 55	26.1	63.2	589	6
40	28 12 66	08 18 07	25.5	70.7	47	6
41	09 09 67	10 06 44	27.7	63.1	578	6

functions given by Ben-Menahem and Harkrider (1964) were used to obtain seismic moment from Rayleigh and Love waves with periods between 70 and 150 seconds. Geometrical spreading and attenuation were accounted for, the latter by using the Q-values given by Ben-Menahem (1965). For the P-waves the far-field displacement for a double-couple given by Keilis-Borok (1959) and Ben-Menahem et al (1965) was used. The geometrical spreading and the attenuation were accounted for using a program described by Julian and Anderson (1968). The effects of the crust and the free surface were compensated using the results of Ben-Menahem et al (1965). P-waves with periods around 20 seconds were used. In Table 13 the moments obtained from mantle waves are given as M_o (surf), the moments obtained from P-waves are given as M_o(P). The period of the surface wave on which the calculation was based is also given in Table 13.

For the 17 shocks where the moment was obtained by both surface waves and body waves, the values agree within a factor of 3 with two exceptions where it agrees within a factor of 4. This agreement is considered good. The moment determined by surface waves is considered more reliable since it is not as greatly affected by local crustal properties as the shorter period body waves. Where it was available, the moment determined from surface waves was used for the strain and stress determinations.

Table 13

Seismic Moments, Apparent Strains and Apparent Stresses (South America)

No.	h [km]	T(surf) [sec]	M_o(surf) dyne cm 10^{26}	M_o(P) dyne cm 10^{26}	m_b	$E_G(m_b)$ dyne cm 10^{21}	$10E_p$(1) dyne cm 10^{21}	$\eta\bar{\varepsilon}$ 10^{-5}	$\eta\bar{\sigma}$ bars	Quality
1	190	120	51.	78.	7.5	630.	-	12.4	91.	B
2	0	100	2.6	7.0	6.9	23.	-	8.8	26.	B
3	0	100	1.8	1.6	6.8	13.	-	7.2	22.	B
4	630	200	28.	-	6.9	25.	-	0.9	12.	B
5	26	100	0.96	1.9	7.0	40.		40.	120.	B
6	83	100	5.9	11.4	7.15	91.	70.	15.	102.	B
7	70	100	2.0	8.0	6.9	25.	11.	12.5	81.	B
8	0	100	1.7	-	7.2	120.	-	71.	210.	B
9	0	100	3.8	-	6.9	25.	-	6.6	20.	B
10	605	-	-	8.3	6.9	25.	36.	3.	39.	B
11	71	100	2.3	2.3	7.25	160.	-	70.	450.	A
12	575	-	-	1.5	6.5	2.5	2.4	1.7	22.	B
13	620	200	12.	3.8	6.6	4.3	3.4	0.5	7.0	A
14	46	100	0.3	0.6	6.7	7.6	-	25.	170.	A
15	41	100	0.64	-	6.5	2.5	-	3.9	24.	A
16	70	30	0.03	-	6.3	0.8	0.7	26.6	173.	B
17	125	100	0.26	1.0	7.0	40.	44.	154.	1050.	A
18	543	200	140.	-	7.35	280.	100.	2.	24.	A
19	23	100	5.2		7.0	40.	-	7.7	23.	A
20	61	85	0.11		6.7	8.0	-	73.	470.	A
21	80	85	2.0	3.0	7.0	40.	14	20.	132.	A
22	575	240	7.4	8.3	7.0	40.	-	5.4	70.	A
23	600	-	-	0.32*	6.3	0.8	-	2.5	33.	A
24	585	-	-	0.003*	5.4	0.0058	-	1.9	25.	B
25	26	100	0.53	0.74	6.7	7.6	-	14.3	43.	A
26	8	70	3.7	-	6.9	23.	-	6.2	19.	A
27	626	-	-	0.097*	5.6	0.017	-	0.18	2.	B
28	655	-	-	0.079*	5.6	0.017	-	0.22	3.	B
29	580	100	0.3	0.87	6.2	0.48	0.06	0.55	7.	A
30	60	70	4.2	3.0	6.75	10.	-	2.4	15.	A
31	80	70	0.063	-	6.4	1.5	-	23.	155.	B
32	72	100	5.4	6.6	7.2	120.		22.	145.	A
33	102	100	0.1	-	6.0	0.16	0.013	1.6	11.	B
34	128	100	1.6	-	6.3	0.52	-	0.33	2.	A
35	590	-	-	1.2	6.6	4.4	-	3.6	48.	A
36	64	100	-	0.08	6.0	0.16	-	2.0	13.	B
37	35	70	0.1	-	6.1	0.27	-	2.7	8.	B
38	120	70	0.15	-	6.4	1.5	-	10.	67.	B
39	589	-	-	0.38	5.85	0.069	-	0.18	2.	B
40		100	23.	18.	7.45	48.	-	2.1	13.	A
41	578	-	-	0.87	6.1	0.27	-	0.31	4.	A

*Berckhemer and Jacob (1968)

Energy

The estimation of energy is less reliable than the determination of the moment. The major part of the observed seismic energy is associated with the body waves. The amplitudes of these waves are subject to strong attenuation, and effects of the local crustal structure at the source and the receiver. This uncertainty in amplitude is very important since the energy is a function of the amplitude squared. In many previous studies involving the seismic energy, the Gutenberg energy magnitude formula has been used (Gutenberg and Richter, 1956) $\log E = 5.8 + 2.4\ m$. However, the accuracy of this formula for deep earthquakes has not been ascertained. In this study P-wave energies were estimated from spectral analysis of seismograms and it was concluded that the Gutenberg-Richter energy magnitude relation provides a good estimate, even for deep shocks.

The energies determined in this study are based on the energies carried by the P-waves. The amplitudes of the S-waves are generally about 3 times larger than those of the P-waves

(Haskell, 1964; Archambeau, 1964). Since the energy in seismic waves is a function of the amplitude squared, the energy carried by the S-waves is about 10 times larger than the P-wave energy. The attenuation of the P-waves is less severe than that of S-waves. Therefore, the indirect estimate using the P-wave energy was preferred to a direct estimate of the S-wave energy. The spectral density of the P-wave at 1 sec period was estimated from the short period vertical records at Pasadena by the formula:

$$u = 2a \frac{Tn}{2\pi}$$

Where u is the amplitude spectral density, a is the ground amplitude, T is the period and n is the number of periods with amplitude a. The spectral densities between 100 and 5 sec period were also available from Fourier analysis of the Pasadena long period records. The high frequency waves account for most of the seismically radiated energy. For most earthquakes the energy associated with waves of lower frequencies than 0.5 cps is much smaller than the energy traveling in a 1 cps wave. For this reason it was considered to be a good approximation to assume that the amplitude spectral density was constant from ∞ to 1 sec

period and equal to the spectral density at 1 sec period. In cases where longer period waves made an unusually large contribution, this energy was also accounted for. On this basis the lower bound for seismic energy called $E_p(1)$ is defined. All the energy that was produced at the source but was not accounted for in the described estimate is taken care of by the seismic efficiency factor η.

The attenuation and geometrical spreading were accounted for in the same way as was done for the moment determination. For attenuation correction the Q-model MM8 described by Anderson et al (1965) was used. The radiation pattern was also taken into account and the integration around the source was performed on a unit sphere using Wu's procedure (Wu, 1966). To estimate the energy from the spectral density the following equation was used:

$$E_p = \frac{1}{15\pi^2} \int_0^{\omega_0} \frac{\rho_s}{A^2(ih)} \frac{u_s^2(\omega) F^2(\omega)}{Amp^2 B^2(\omega)} \omega^2 \, d\omega \qquad (25)$$

where ρ_s is the density at the surface, u_s is the spectral density observed at the surface, F is the correction for attenuation, ω is frequency, A(ih) is the correction for the radiation pattern ($1/15\ \pi^2$) is the factor resulting from the integration over a unit sphere, B is the correction for the effect of the crust and free surface, and Amp = $u_s(\rho_s/I_f)^{1/2}$, where I_f = power per unit solid angle on a focal unit sphere. For frequencies between 0 and 1 cps the integral in equation (25) simplifies to

$$E_p(1) = \frac{1.4}{T^3} \left[\frac{F(\omega_o)u(\omega_0)}{A(ih)\text{Amp } B(\omega_o)} \right]^2$$

The energy carried by the surface waves is automatically included in the body wave energy, since the integration was performed on a unit sphere around the source. $E_s = 10\ E_p(1)$ is taken as the estimate for the lower bound of seismically radiated energy. This value can be compared in Table 13 with $E_G(m_b)$, the energy estimated by the energy magnitude relation (Gutenberg and Richter, 1956). The magnitudes were based on the radiation pattern corrected amplitudes of the short-period P-waves recorded at Pasadena and Uppsala. The agreement between the energies estimated by the two methods is fair except for the two smallest shocks. This

discrepancy is considered in a later section. For shallow events $E_p(1)$ could not be obtained because the 1 sec P-wave did not reach the distant station of observation. The $E_p(1)$ determination was independent of the assumptions on which the magnitude determination and the energy-magnitude relation are based, and allowed a check on the Gutenberg energy for shocks between 70 and 650 km depth. Both energy estimates are based on the P-waves of the same seismographs. The agreement of the results obtained by the two methods indicates that there is no gross systematic error with depth in the Gutenberg energy determination between 70 and 650 km. The Gutenberg energy estimate was therefore used for all strain determinations.

Both energy estimates carried out are only a lower bound for the total energy, which could be an order of magnitude larger at all depths as Wu (1966) suggests on the basis of his analyses of the S-waves. In this case, all the estimated strains and stresses would be an order of magnitude larger. The main concerns of this study, however, are the variations of apparent strain with depth and not so much its absolute value. To obtain a better estimate for the latter a better energy determiatnion is clearly needed. This improvement must come from local recordings of short period waves that propagated from the hypocenter up the high Q slabs.

Apparent Strain and Stress

The apparent strain and apparent stress values for all earthquakes studied in South America are given in Table 13 in columns 9 and 10, respectively. The apparent strain and apparent stress for four additional earthquakes for which Berckhemer and Jacob (1968) give the moment were computed and included in Table 13. The last column in Table 13 gives the quality of the data for each earthquake. Good data are marked by the letter A. The letter B indicates less reliable results with either a poor fault plane solution or a small size of the earthquake, in which case the moment determination may be less accurate. The apparent strain and apparent stress values for all 41 earthquakes in Table 13 are plotted versus depth in Figures 46 and 47, respectively. The numbers correspond to the first column in Tables 12 and 13. The size of the symbols indicate the quality of the analysis. A large symbol corresponds to quality A, a small symbol to quality B. Diamond shaped symbols indicate shallow earthquakes not located in the general seismic zone. Full circles with crosses indicate earthquakes located around 20°S, a portion of the seismic zone characterized by complete lack of deep earthquakes.

An estimate of the errors that may be connected with points plotted in Figures 46 and 47 must be based on the accuracy with

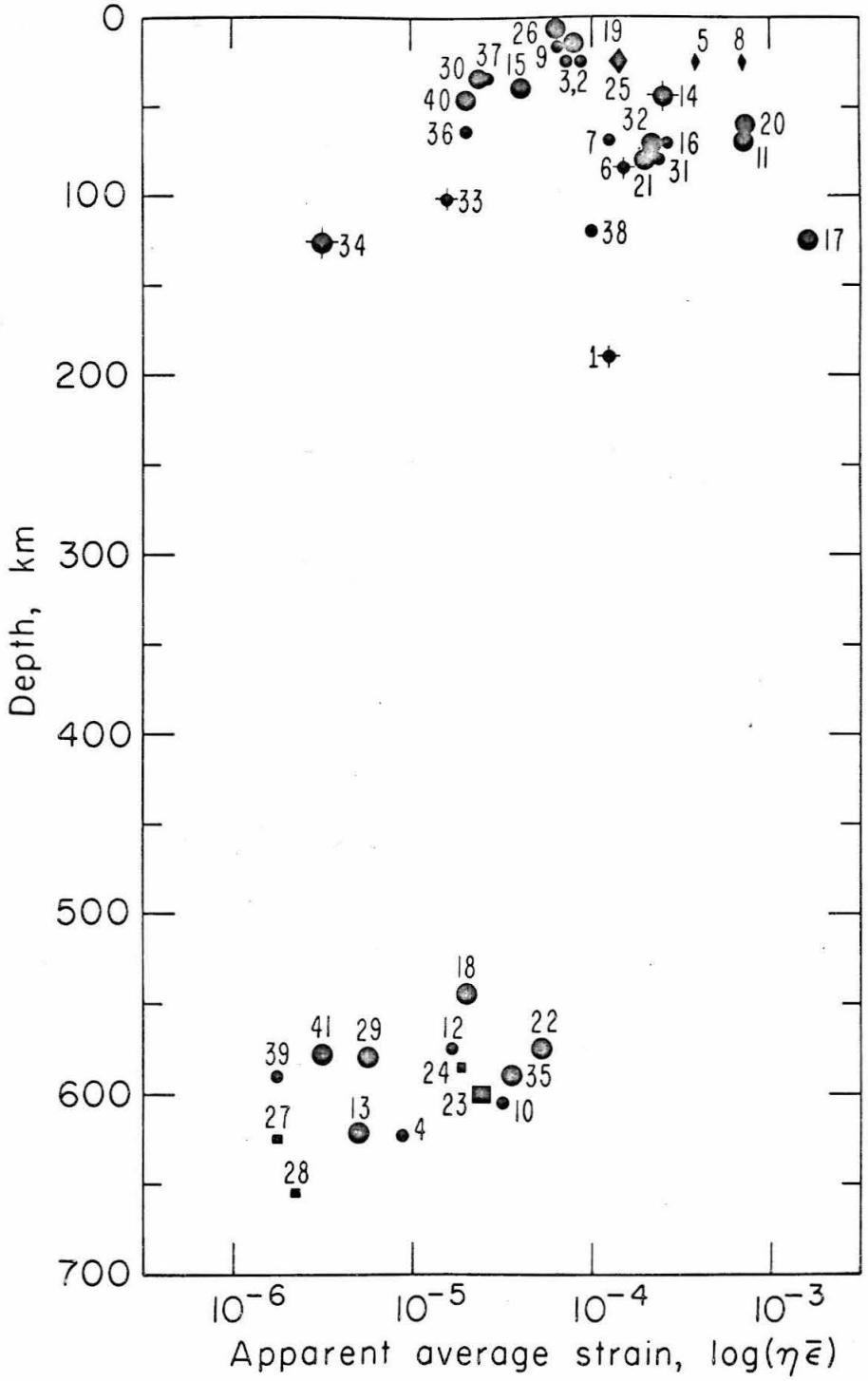

Figure 46. Apparent average strain for South American earthquakes as a function of depth.

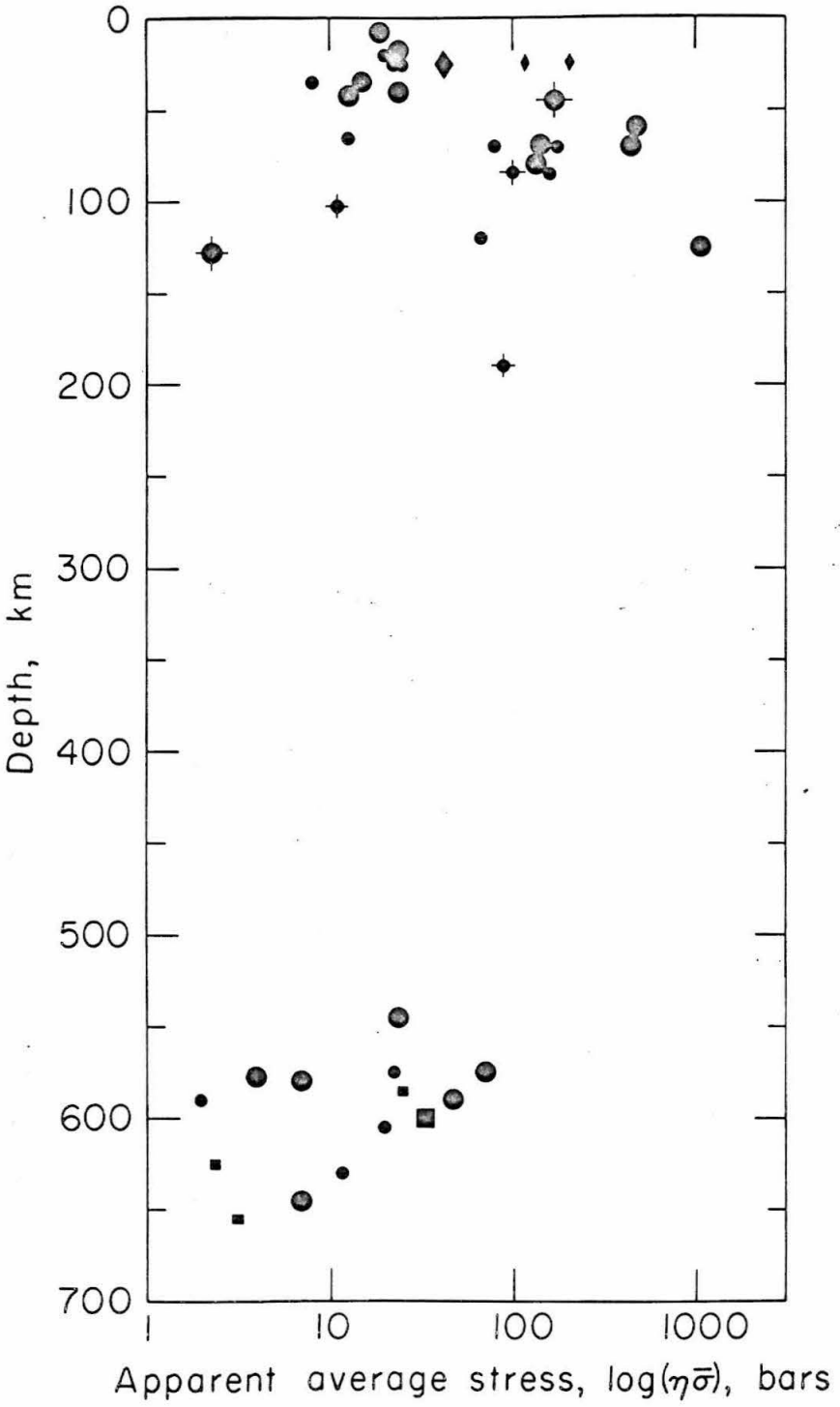

Figure 47. Apparent average stress of South American earthquakes as a function of depth.

which the depth, the moment, and the energy are determined. The depths are taken from the USCGS and the I.I.S. hypocentral locations and pP readings at Pasadena. For shallow earthquakes, where the fault dimensions may exceed the hypocentral depth, the value for depth is more or less meaningless and the scatter is considerable. Based on the agreement between moment obtained by surface wave and by body wave analyses, the moment is believed to be accurate to within a factor of 2.5. The lower bound estimated for the seismic energy may be considerably different from the total seismic energy. This difference however, may be taken into account by the seismic efficiency factor. The accuracy we are concerned with here is only the accuracy in estimating a consistent lower bound, since we are mainly concerned with comparing earthquakes. The agreement between the Gutenberg energy estimate and the estimate obtained by spectral density, in the average a factor of 3, is taken as an estimate of the relative accuracy of the energy values. The apparent strain values of a single shock could therefore be wrong in the worst case by an order of magnitude. The mean error, however, is smaller. The apparent strain (stress) versus depth pattern in Figures 46 and 47 is believed to be significant.

In order to evaluate the changes of apparent strain (stress) with depth in a typical portion of the South American deep seismic

zone, the earthquakes with hypocenters outside this zone (diamond symbols) and those located in the peculiar region around 20°C (full circles with cross) must be excluded. Then we see that from the surface downward, the pattern is one of rapid increase of apparent stress in the first 100 kilometers. Around that depth a mean value of 270 bars and a largest value of about 1 kbar is reached. With greater depth the apparent stress seems to decrease again. Unfortunately, there are no data available for intermediate depths, since no earthquakes occur there in South America. From limited data on other trench systems (Table 17), it appears that the decrease occurs gradually. At great depths, the apparent stresses reach a minimum with values comparable to the ones at the free surface ($\sim$ 20 bars).

For a qualitative evaluation of evidence for the relatively high apparent stresses around 100 km depth, examples of long period seismograms are shown in Figure 48. The hypocenters were at depths of 0, 125, and 600 km, respectively. By inspection, one can observe that the earthquake with h = 125 km radiated strong high frequency and weak low frequency waves compared with both the shallow and deep examples. The energy estimate is strongly dependent on the high frequency content and the moment estimate on the low frequency content. The ratio of high to low frequency spectral amplitude, energy to moment, is a direct measure

Date	h [km]	m_b	(a)	(b)	$\eta\bar{\sigma}$ [bars]
29 08 63	23	6.5			23
13 04 63	125	7.0			1050
08 12 62	620	6.6			7

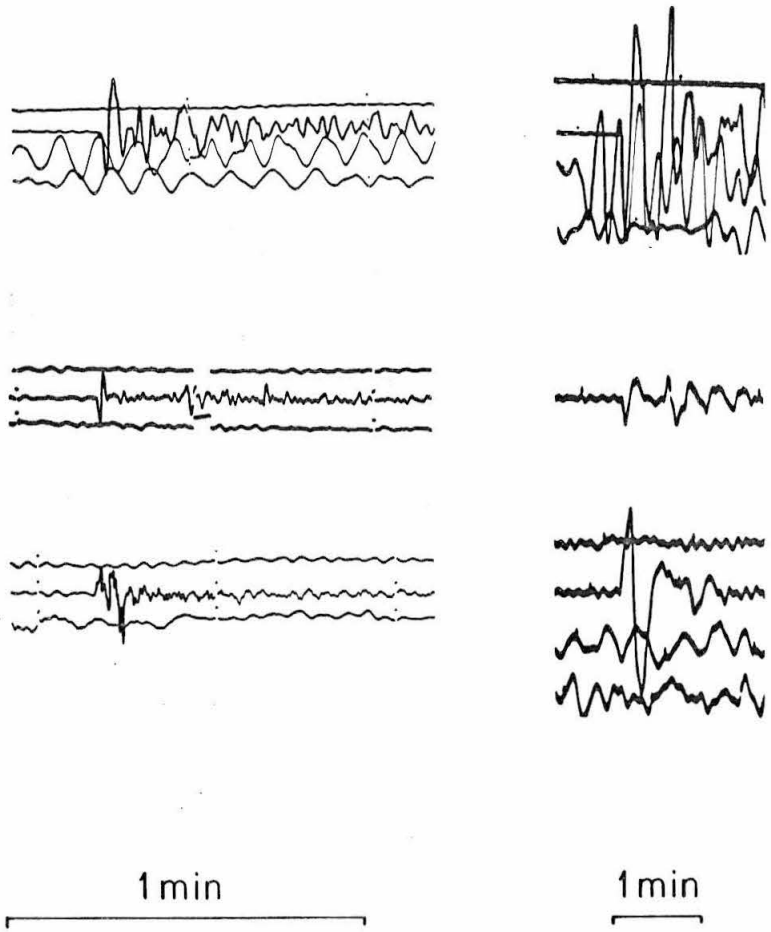

Figure 48.

of the apparent strain (stress) in the source region. The apparent stress for the earthquake with depth 125 km is approximately seventy times higher than the apparent stresses in the source regions of the other two examples.

The diamond-shaped symbols in Figures 45, 46, and 47 indicate shallow earthquakes with locations at considerable distance landward from the trench. The hypocentres of these events do not fall into the general zone of seismic activity. The shallow earthquakes located in the main underthrust zone have low apparent stresses suggesting that the break occurs along well-developed and relatively well-lubricated fault zones. Shallow earthquakes located outside the main zone (diamond symbols) have high apparent stresses, which may suggest that they occur along less well-developed fault surfaces.

Figure 49 represents another way of looking at the same data, the seismic moment is plotted as a function of the body wave magnitude. The line through the data is the theoretical curve obtained by Brune and King (1967). This line is still a very good fit. As was pointed out in the second chapter, data points falling above this line correspond to earthquakes with low stresses in their source region and data points below this line indicate high stresses. The division is very clear. The deep

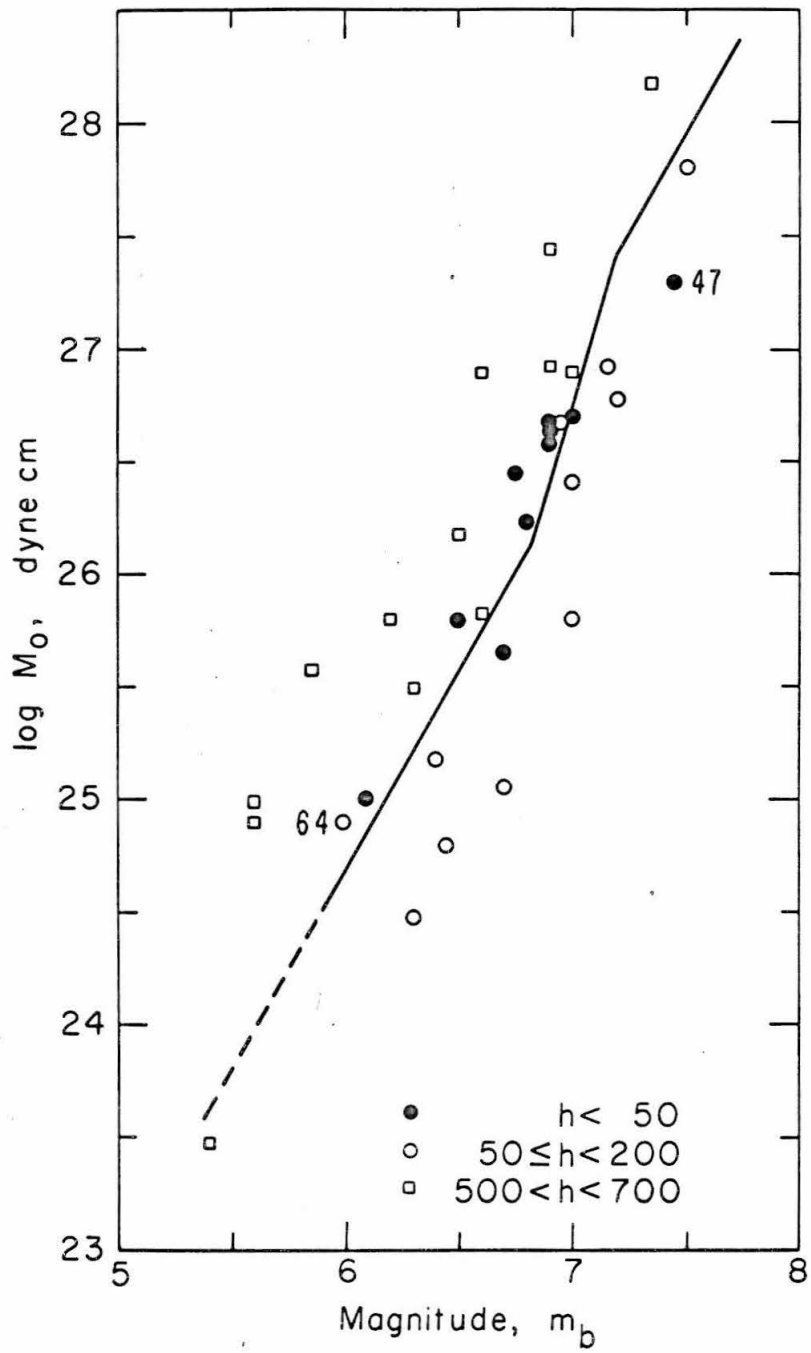

Figure 49. Moment-magnitude relation for South American earthquakes. Numbers indicate depth.

earthquakes fall above the line, while the shocks of intermediate depth fall below it. Numbers near some points give focal depth in km.

Seismic Efficiency and Source Dimensions

Since the apparent stress is a product of the seismic efficiency and the average stress in the source region, it is a question which of the two factors is responsible for the variation of the apparent stress with depth.

It is impossible to determine the seismic efficiency without additional measurements in the source region, such as measurements of the dissipated energy, or of the total elastically released energy. If both the apparent stress $(\overline{\eta\sigma})$ and the stress drop τ are available, an upper bound for the efficiency η may be estimated. To obtain the stress drop it is necessary to be able to estimate the source dimensions or the displacements associated with the dislocation. Berckhemer and Jacob (1968) have obtained the stress-drops of six South American shocks by assuming a rupture velocity at the source. Their estimate of stress drop was based on comparison of measured amplitude spectral density of the P-wave to the spectral density of propagating rupture models. The total stress, for which the apparent stress is a lower bound, must be at least as large as the stress drop.

From a comparison of Berckhemer and Jacob's results for stress drop with the apparent stress, one can obtain an approximate upper bound for the efficiency.

Since $\sigma_2 \geq 0$ and $\tau \leq \sigma_1$

$$(\eta\bar{\sigma}) = \eta \frac{\sigma_1 + \sigma_2}{2} \geq \eta \frac{\sigma_1}{2} \geq \eta \frac{\tau}{2} \qquad (26)$$

$$\eta \leq \frac{2(\eta\bar{\sigma})}{\tau} = \eta_{max}$$

The maximum of the seismic efficiency is equal to the actual efficiency if the stress drops to zero. When melting occurs at the dislocation surface the stress may indeed almost drop to zero and the maximum efficiency , particularly for large shocks, may be not too different from the actual efficiency.

Berckhemer and Jacob (1968) determined stress drops for two models. One assuming a rupture velocity of 2.5 km/sec called τ_1, and one assuming 3.5 km/sec called τ_2. In Table 14 the maximum efficiency η_{1max} and η_{2max} corresponding to the two models are given. The values in Table 14 suggest that for deep earthquakes the level of the maximal seismic efficiency may be around 10%. It also appears that the maximal seismic efficiency is a function of magnitude. In order to determine the dependence of efficiency on magnitude, the apparent stress of deep earthquakes was

Table 14

Maximum Efficiency and Dislocation Area

No.	h	Stress Drop τ_1 [bar]	Stress Drop τ_2 [bar]	Maximum Efficiency η_{1max}	Maximum Efficiency η_{2max}	m_b	Dislocation Area F_1 km^2	Dislocation Area F_2 km^2
17	125	24000	8500	0.09	0.25	7.0	3.	6.
21	80	6900	2450	0.04	0.11	7.0	20.	40.
22	575	1200*	425*	0.12	0.33	7.0	140.*	280.*
23	600	920*	325*	0.07	0.2	6.3	20.*	40.*
24	585	30*	11*	>1.	>1.	5.4	7.*	14.*
27	626	270*	95*	0.02	0.05	5.6	20.*	40.*
28	655	220*	78*	0.03	0.08	5.6	20.*	40.*
35	590	250*	89*	0.38	1.	6.6	34.*	68.*

*Berckhemer and Jacob (1968)

plotted versus body wave magnitude in Figure 50a. The large symbols again indicate reliable solutions, the small symbols less reliable ones. Triangles indicate earthquakes with locations around 27°S, circles represent earthquakes between latitude 8°S and 15°S. It emerges very clearly that the apparent stress of deep earthquakes is a function of magnitude. On the map of South America the deep earthquakes plot as two groups, tirangles and circles in Figure 50a, with epicenter 4 and 18 somewhat apart from the others. Each group separately exhibits approximately the same dependence of the apparent stress on magnitude. The hypocenters of each cluster are located very close to each other and magnitude does not vary systematically with depth. The total stress therefore can be assumed to be roughly constant in each group. Under this assumption it is the efficiency that varies with magnitude. It may be significant that the earthquakes of the northernmost group display consistently the highest apparent stresses at all magnitudes. But it is felt that at this point there is not enough data to make the case for this regional difference convincing. The straight line in Figure 50a therefore is an average least square fit (considering all data except one anomalous point) with the equation

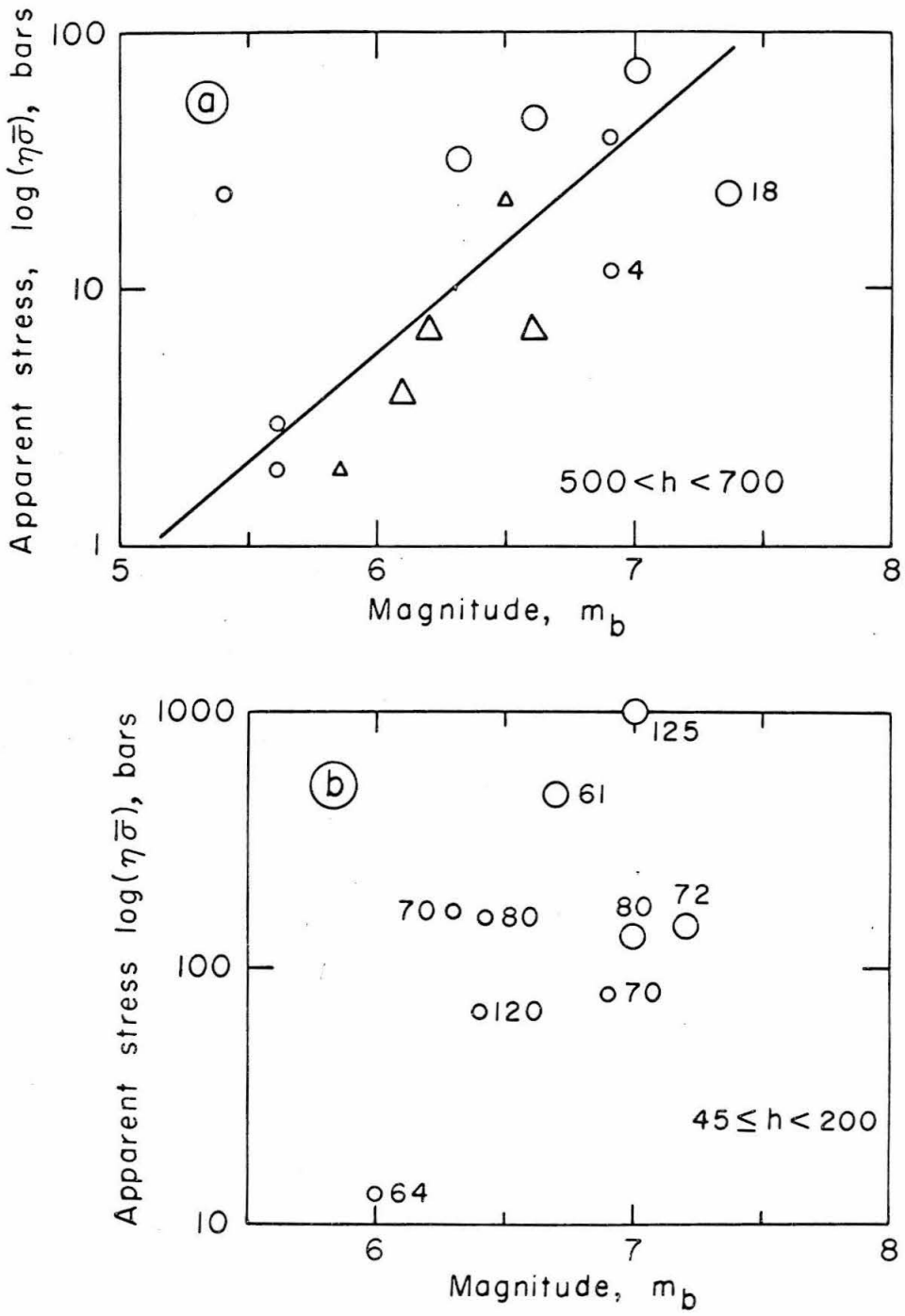

Figure 50. Apparent stress-magnitude relation of South American (a) deep and (b) intermediate earthquakes.

$$\log (\eta\bar{\sigma}) = 0.8\ m_b - 4.1 \qquad \begin{matrix} 500\ \text{km} < h \\ 5.5 < m_b < 7.5 \end{matrix} \qquad (27)$$

If the average stress is assumed to be a constant the slope of 0.8 indicates the variation of the efficiency with magnitude

$$\log \eta = 0.8\ m_b + c \qquad (28)$$

To put a straight line through the data in Figure 50a is a crude approximation. It implies that earthquakes of sufficient size, say around $m_b = 8.0$, will be 100% efficient. This is impossible and a curve decreasing in slope with increasing magnitude would be a more realistic approximation.

The above results are only valid for deep shocks. Intermediate depth earthquakes are more difficult to analyze since the apparent stress increases rapidly with depth. The data for intermediate shocks are plotted in Figure 50b. The earthquakes located in the anomalous region around 20°S are omitted. The numbers next to the symbols give depth in kilometers. The range of magnitudes covered is not large enough to warrant definite conclusions, but the efficiency of intermediate earthquakes may well be a strong function of magnitude. The dislocation area of two shocks with

intermediate depth were determined following Berckhemer and Jacob (1968) and the stress drops as well as the maximal efficiencies were estimated (Table 14). The maximal efficiencies of these earthquakes at intermediate depth are approximately the same as the ones for deep earthquakes.

The apparent stresses of shallow shocks analyzed in this study do not vary significantly with magnitude. This observation is in agreement with the study by King (1969) who found a very small dependence of efficiency on magnitude for shallow shocks.

The dependence of apparent stress versus magnitude could be caused by two factors, either by the physics of the source or a systematic bias in the analysis due to overestimation of moment or underestimation of energy for small shocks. The seismic moment as an error source can safely be discarded. The seismic energy, however, could indeed be systematically underestimated for small shocks. In determining $E_p(1)$ only periods down to 1 sec were considered. For the largest events the periods with the main energy contribution are included in this interval. For small shocks the waves with periods shorter than 1 sec carry a larger fraction of the total energy than those neglected periods do for large shocks. The comparison of $E_p(1)$ with the Gutenberg energy E_G in Table 13 shows that E_G is corrected for this effect. Yet

it may be that the correction is not large enough. High frequency recordings of waves propagating up the high Q zone under island arcs, as reported by Oliver and Isacks (1967), may furnish the answer to this problem. Until more detailed studies are carried out the energy underestimation cannot be ruled out as a possible systematic error.

Earthquakes at great depth could be associated with dehydration of hydrous minerals (Raleigh and Paterson, 1965; Isacks et al, 1968) or with melt on the shear plane (Orowan, 1960; Griggs and Baker, 1969; Savage, 1969). In the latter case, a very simple physical explanation for the varying efficiency could be offered. With increasing magnitude the amount of melt, and the amount of energy lost by melting, increase in rough proportion to the square of the earthquake dimensions. The amount of available elastic energy, however, increases with the third power of the earthquake dimensions. This would mean that for large shocks a smaller proportion of energy disappears into heat. The efficiency consequently increases with increasing magnitude.

In order to make the data presented in Figure 47 more homogeneous the apparent average stress was normalized to magnitude 7.0. It was assumed that equation (28) holds not only for deep but also for intermediate earthquakes, so all shocks with hypocenter below

45 km were normalized according to equation (28). For shallow shocks no correction was considered necessary. The result is shown in Figure 51. Earthquakes with epicenters outside the typical seismic zone are omitted. The symbols are the same as in Figures 46 and 47. The general pattern of Figures 46 and 47 is preserved and the scatter is reduced. The averages of the normalized apparent stresses are: 18 bars at $h \leq 45$ km, 380 bars at $45 \text{ km} < h \leq 125$ km and 44 bars at $450 \text{ km} < h < 660$ km. These values apply for a magnitude 7.0 event for which at all depths the efficiency is estimated to be less than 0.1. If the stress drops almost to zero the efficiency will be close to 0.1.

The apparent strain is the energy density in the source region. The fact that an earthquake of a given magnitude is caused by larger strains around 100 km depth than at the surface, implies that the source dimensions at 100 km depth are much smaller. Using the method of Berckhemer and Jacob (1968) the dislocation areas were roughly estimated for two shocks around 100 km depth. The fault dimensions of these magnitude 7.0 events are estimated to be between 2 and 7 km. These values are surprisingly small but they agree with several observations listed by Iida (1959). The high stresses correspond well to the breaking stresses of crustal rocks. The estimated stresses of 3 kbars at 100 km depth also agree well with the pressure a sinking slab exerts on the lithosphere. McKenzie (1969) estimated density differences

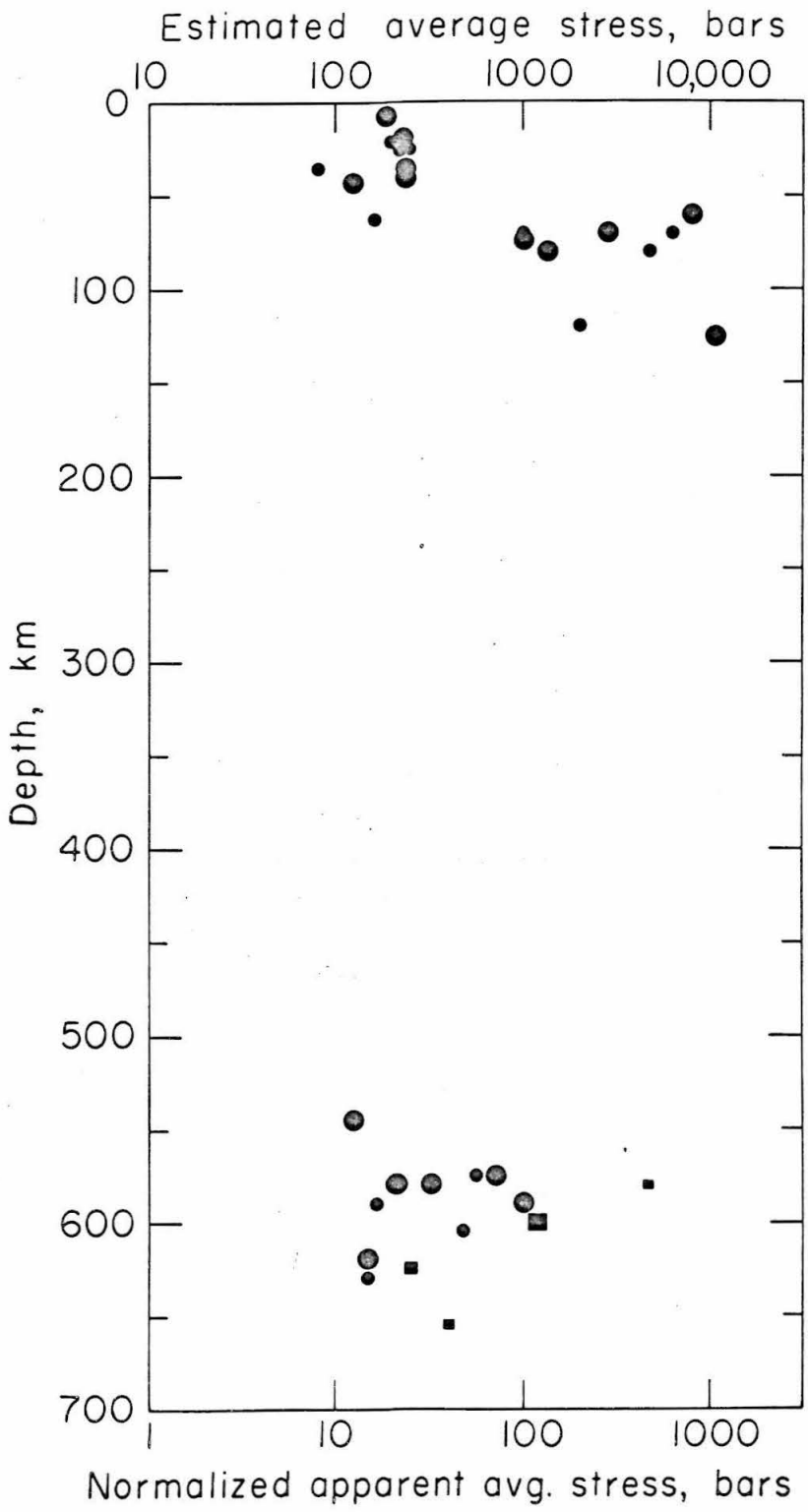

Figure 51. Normalized apparent stress and estimated true stress in South America versus depth.

between the mantle and the downgoing slab due to temperature differences and obtained a minimum estimate of 2.5 kbar for the stresses that could be accumulated in the slab.

Comparison with Other Trenches

Oliver and Isacks (1967) studied the high frequency content of S and P waves from deep earthquakes in the Tonga-Fiji region with local stations. They found that waves with ray paths in the deep seismic zone to a station in Tonga were much less attenuated than waves with ray paths in the surrounding mantle. From these observations they concluded that cold lithospheric material was plunging underneath the island arc remaining relatively cold down to the depth of the deepest earthquakes. A corollary is that low attenuation for the deepest earthquakes can only be observed if the downgoing slab of lithosphere is continuous and has the high Q property all along its length. From limited data, presented in Table 17, it appears that in other trench systems the apparent stresses also increase rapidly with depth, reach a maximum and decrease again at greater depth. Stresses associated with earthquakes of intermediate depths in some trenches have intermediate values between the high stresses at 100 km depth, and the low stresses around 600 km depth. This may indicate that in this island arc the material at intermediate depth

has intermediate values of strength.

Kasahara (1957) has estimated the source volume of shallow and deep shocks in Japan. Dividing the Gutenberg energy by the volume, he obtained energy density. This value corresponds to:

$$\eta\left(\varepsilon_1^2 - \varepsilon_2^2\right) = \eta\left(\varepsilon_1 - \varepsilon_2\right)\left(\varepsilon_1 + \varepsilon_2\right) = 2\eta \cdot \Delta\varepsilon \cdot \overline{\varepsilon}$$

and is not quite comparable to the apparent strain determined in this study. Even though Kasahara's study was confined to a different island arc, his results for shallow and deep shocks are in approximate agreement with the results presented here. Kasahara has not, however, analyzed shocks in the critical depth range around 100 km.

If a ray would propagate down the rigid high Q slab (Oliver and Isacks, 1967) and up another such rigid slab to a recording station, the high frequencies would fail to be filtered in the low velocity zone. This would lead to a relative overestimate of the energy and hence to an overestimate of the apparent average stress relative to earthquakes at greater depth. In this study, therefore, care was taken not to consider ray-paths propagating down or up a slab.

Ocean Floor Consumption

The two variables which control the strength of rocks in the earth are pressure and temperature. The changes of elastic properties of material present in the lithosphere and mantle are small and can be neglected with one important exception, the behavior of serpentinite described by Raleigh and Paterson (1965). Under confining pressure of 5 kbars and low temperature serpentinite shows high strength. Above 300° to 500°C dehydration occurs and the serpentinite loses strength very rapidly. In general, increasing pressure increases the strength, increasing temperature decreases it. In particular, at the depth of the low-velocity channel, around 100 km, the temperature-pressure conditions are such that partial melt is very likely to be present (Anderson and Sammis, 1970) and the material has extremely low strength. In the zone of deep earthquakes, however, the present analysis indicates that the material around 100 km has very high strength. The hydrostatic pressure in the downgoing slab and the neighboring mantle is approximately the same. It is clear that the temperature must be different.

This result is supporting the hypothesis of ocean floor consumption. As the lithosphere plunges downward the pressure increases instantaneously. Due to the low heat conductivity of the material, the slab is heated up by the surrounding mantle

very slowly. Simple models of the temperature distribution in a downgoing slab indicate that the slab can stay relatively cool with respect to the surrounding mantle down to the depth of the deepest earthquakes (McKenzie, 1969). Two lines of evidence indicate that earthquakes a depth below about 60 km do not account for the slip of the downgoing slab with respect to the adjacent mantle. Brune (1968) showed that the slip rate computed from the sum of the seismic moments for intermediate and deep earthquakes is much too small. He concluded that creep along a weak boundary between the mantle and the lithospheric slab must take place. In addition, Isacks et al (1968) and Isacks and Molnar (1969) have shown that the fault planes for intermediate and deep earthquakes are not oriented parallel to the slip direction of the slab. They showed that instead the pressure or the tension axis are parallel to the slab. The stresses released by earthquakes are stresses propagated along the slab as it is pulled or pushed down into the mantle, as the case may be. The amount of stress the material in the slab is able to accumulate before it breaks, is only a function of the local strength of material in the slab. The present results suggest that as the slab plunges down the strength of the lithosphere increases first, and when the increase in temperature becomes appreciable, around 150 km, weakening starts.

The strength then decreases until at depths around 600 km the strength is almost as small as the strength at the surface. At still greater depth the slab material can no longer support stresses large enough to produce earthquakes, and it blends into the rest of the mantle. The length of the South American slab is demonstrated to be in a thermal steady state. The length of this slab is not determined by the age of the present consumption site, or a change in mantle properties at this depth, but it is only a function of the temperature-pressure conditions in the mantle and the local consumption rate. It will be important to determine in island arcs where the seismic activity is continuous from the surface to great depths whether the decrease in strength is sudden or gradual, that is, whether the mechanism of brittle fracture proposed by Raleigh and Paterson (1965) is applicable or not.

It is now very interesting to next determine the stresses associated with the lower terminating earthquakes in trench systems where the deepest activity occurs at intermediate depth. If such earthquakes indicate low strength, i.e., apparent stresses in the order of 20 to 50 bars, one can conclude the slab is heated up at its lower termination to the extent that it cannot support stresses and blends with the mantle. This implies that it has reached a thermal steady state and its short length must

be due to a slow consumption rate. If, on the other hand, such lower terminating earthquakes of intermediate depth yield intermediate to high values of strength, i.e, apparent stresses between 100 to 1,000 bars, the slab would not be heated up enough to terminate the earthquake activity. In this case the shortness of the slab would have to be a function of the time during which the trench was active. The shorter the slab with relatively high stress bottom, the younger the consuming system.

In the South American slab there is an anomalous region between latitude 13 and 19°S. In this part the deepest earthquakes large enough to yield fault plane solutions and moment determinations occur at depths of about 120 km, and deep earthquakes do not occur at all (Barazangi and Dorman, 1969). The stress analysis in this region showed that shocks around 100 km depth have anomalously low stresses comparable to the stresses of very deep earthquakes in the other portions of the downgoing slab. These events are marked by full circles with a superimposed cross in Figures 45, 46, and 47. The absence of deep focus earthquakes together with the low strength of the slab at 100 km depth suggests that in this portion the slab may be heated up faster than anywhere else. The seismicity off the coast of South America indicates that there exists only one rigid plate between the equator and 40°S. The

consumption rate therefore cannot drop and increase again from north to south along the trench. The marked change in direction of the trench around 17°S may be interpreted as the meeting point of two trenches, the convex Peruvian trench and the straight Chilean trench. The downgoing slab may be broken up in this discontinuous region. The surrounding mantle may then partially penetrate the slab material, which will be heated up far more efficiently than an ordinary portion of the slab. The stresses at intermediate depth will then indicate low strength, and stresses for deep earthquakes will not be able to be accumulated.

EARTHQUAKES ON RIDGES COMPARED TO SHALLOW EARTHQUAKES IN TRENCHES

INTRODUCTION

Both the creation and the consumption of lithosphere is associated with earthquakes. Over ridges the heat flow is high (Bullard et al, 1956); over trenches it is rather low (Bullard, 1963; McKenzie and Slater, 1968). At ridges material is presumed to rise and thus the source region is characterized by decreasing hydrostatic pressure and decreasing temperature. In trench areas the opposite condition prevails. The high heat flow values on ridges indicate that the material there is warmer than in the average crust, except for very shallow depths, where the temperature equals that at the surface. If there are any earthquakes occurring at depths exceeding 20 to 30 km, the weakness of the relatively warm source material should be reflected by small apparent stress values. It is interesting, therefore, to compare the magnitude of the apparent stresses causing earthquakes at the ridges and trenches, and to consider the possibility of two completely different rupture mechanisms.

Data

The method used to determine moment and radiated energy for earthquakes on ridges was the same as described above. Across oceanic ridges S-waves are strongly absorbed (Molnar and Oliver, 1969). The P-wave, however, on which our energy estimate is based is not as strongly affected. The energy of earthquakes on ridges is probably underestimated relative to earthquakes in trenches. In the worst possible case, 100 km with material of Q = 100 around the source, the error would be a factor of two. The results are not corrected for this effect because there is no data on which to base a correction.

The results for 14 Aleutian earthquakes are given in Table 15. The shocks are grouped following Stauder (1968) into (a) those which are located under the trench, and (b) those which are located under islands. All with one exception are shallow events with depth determinations that are likely to be too large because of the effect described by Davies and McKenzie (1969). The one intermediate depth event is associated with a relatively large stress as South American intermediate depths earthquakes are. An exception as to the source mechanism is the shock of 14 June 1962 which was associated with strike-slip faulting. It has a relatively large apparent stress value and will be excluded in taking the average. The average of the apparent stress in the two Aleutian

Table 15

Apparent Strains and Stresses in the Aleutians

Date d	m	y	Hour	Latitude N	Longitude	Magnitude m_b	Energy E_G dyne-cm x 10^{20}	Moment M_o(surf) dyne-cm x 10^{25}	Moment M_o(P) dyne cm x 10^{25}	Apparent Strain $\eta\bar{\varepsilon}$ 10^{-5}	Apparent Stress $\eta\bar{\sigma}$ bar	Depth h km	Fault Mechanism Reference
22	02	58	10	50.5	-175.	6.6	44.	26.	15.	2.1	6.3	33	22
07	02	65	02	51.4	173.4	6.2	4.7	4.	-	1.2	3.6	40	22
30	03	65	02	50.6	177.9	7.1	694.	39.	37.	18.0	54.	51	22
29	07	65	08	50.9	-171.4	6.8	130.	7.6	8.4	16.3	49.	23	22
01	10	65	08	50.1	178.2	6.8	130.	17.	5.8	11.4	34.	23	22
02	06	66	03	51.1	176.0	6.2	4.7	1.7	0.37	11.	33.	41	22
07	08	66	02	50.6	-171.3	6.8	130.	30.	11.	5.3	19.	39	22
14	06	62	07	54.3	169.1	6.3	8.3	0.24	-	35.	105.	34	22
21	12	62	08	52.4	-168.5	6.7	76.	-	5.7	13.	39.	33	21
22	12	62	15	52.5	-168.8	6.3	8.3	7.	2.6	1.7	5.	47	21
26	12	62	22	53.9	168.7	6.6	44.	9.5	12.	4.0	12.	33	22
01	01	63	23	56.5	-157.7	6.6	44.	4.3	5.2	9.2	28.	50	22
02	07	65	20	53.1	-177.6	6.9	230.	730.	-	0.3	1.	59	22
02	04	63	16	53.2	-171.7	6.4	14.5	0.15	-	100.	700.	142	22

subgroups are slightly different, 28 ± 16 bars under trenches, 17 ± 13 bars under islands. Considering the accuracy of apparent stress determinations and the small population of the two groups, this difference cannot be considered significant.

The average of all shallow Aleutian earthquakes is 24 ± 16 bars which within the accuracy is the same as the value obtained for South American shallow events, 18 ± 8 bars.

The fault mechanism references are given in tha last column of Table 15 and 16. The code is as follows:

2 Banghar and Sykes (1969)

6 Bolt et al (1968)

21 Stauder and Bollinger (1964)

22 Stauder and Bollinger (1966)

23 Sykes (1967)

24 Tobin and Sykes (1968)

25 Sykes (1968)

Tsai (1969) has recently determined depths for earthquakes on ridges and fracture zones by surface wave analysis. At the

same time he obtained the moment for these earthquakes. In Table 16 the apparent strains (stresses) for 27 events located on oceanic ridges and fracture zones are given. The moments for 17 shocks calculated by Tsai are included. Where the moments were obtained by Tsai and in the present study, they are in very good agreement. The events in this table are grouped in normal faults occurring on the ridges proper and strike slip events located on transform faults. There are no differences between the apparent strains (stresses) of these two groups. The apparent stresses in geographic regions like North Atlantic ridge, East Pacific rise, and NE Pacific are also the same. The average of the apparent stresses of all shocks of Table 17 is 17 ± 12 bars. This value is the same within the accuracy as the average of all shallow Aleutian and all

Table 16

Apparent Strains and Stresses on Ridges and Transform Faults

Date d m y	Hour	Latitude	Longitude	Magn. m_b	Energy E_G dyne-cm $\times 10^{20}$	Moment M_o(surf) dyne-cm $\times 10^{25}$	Moment $M_o^{\dagger}$ dyne-cm $\times 10^{25}$	Apparent Strain $\eta\bar{\varepsilon}$ $\times 10^{-5}$	Apparent Stress $\eta\bar{\sigma}$ bars	Fault Mechanism Reference
06 08 62	01	32.26 N	41.03 W	6.2	4.8	1.4	1.45	3.4	10.2	23
25 09 63	07	16.70 S	28.57 E	6.2	4.8	3.2	-	1.5	4.5	23
25 08 64	13	78.12 N	126.64 E	6.9	230.	36.6	-	6.3	18.9	23
01 10 64	11	43.40 N	126.60 W	6.0	1.6	-	0.14	11.4	35.2	6
18 04 65	06	41.50 N	127.22 W	5.4*	0.8	2.2	0.94	0.5	1.5	24
02 06 65	23	16.0 N	46.8 W	6.5	25.2	-	2.79	9.0	27.	25
16 11 65	15	31.03 N	41.49 W	6.6	44.	5.65	5.22	8.1	24.3	23
20 03 66	01	00.81 N	29.93 E	6.6	44.	40.3	-	1.1	3.3	23
20 06 65	18	42.93 N	126.29 W	5.6*	1.6	0.18	0.19	8.6	25.8	24
04 07 66	12	37.5 N	24.8 W	5.6*	1.6	-	0.91	0.57	1.7	2
07 03 63	05	26.87 S	113.58 W	6.85	174.	10.0	-	17.4	52.2	23
28 03 63	00	66.29 N	19.78 W	6.6	44.	27.6	-	1.6	4.8	23
03 04 63	14	54.40 S	128.2 W	6.2	4.8	1.33	-	3.5	10.5	23
19 05 63	21	23.87 N	45.96 W	6.55	33.	24.6	-	1.3	3.9	23
03 08 63	10	07.45 N	35.82 W	6.9	230.	20.4	-	11.	33.	23
22 08 63	09	42.80 N	126.19 W	5.3*	0.56	0.81	-	0.7	2.1	24
17 11 63	00	07.80 N	37.35 W	6.5	25.2	14.0	18.00	1.6	4.8	23
31 03 64	09	50.83 N	130.05 W	5.8*	3.2	3.8	1.69	1.2	3.6	24
17 05 64	19	35.29 N	36.07 W	6.25	6.3	1.7	-	3.7	11.1	23
07 07 64	13	43.35 N	127.20 W	5.4*	0.8	0.26	0.038	5.3	15.9	24
14 06 65	09	44.6 N	129.50 W	5.4*	0.8	-	0.16	5.0	15.	6
16 08 65	12	0.5 S	20.0 W	6.7	76.	-	2.76	28.	84.	25
16-09 65	04	40.35 N	125.84 W	5.4*	0.8	0.19	0.065	6.2	18.6	24
15 11 65	11	0.17 S	18.70 W	6.4	14.5	8.4	2.03	2.8	8.4	23
06 12 65	11	18.87 N	107.18 W	6.5	25.2	-	13.72	1.8	5.4	23
22 05 66	07	21.26 N	108.75 W	5.5*	1.1	0.18	0.20	5.8	17.4	25
23 05 66	11	21.36 N	108.65 W	5.6*	1.6	-	0.31	5.2	15.6	25

†Tsai (1969). *Local magnitude M_L

shallow South American earthquakes. It is concluded therefore, that the average apparent stresses for shallow shocks of all regions considered is the same; it is around 20 bars.

Discussion

Since the apparent stress is a product of two parameters, seismic efficiency times average stress, the fact that it is constant can be interpreted in two ways. One possibility is that the two parameters vary from region to region in such a way that their product is constant. This coincidence would seem unlikely unless some physical significance of this product, other than it being a lower bound for average shear stress, could be postulated. The other possibility is that the shear stress and the seismic efficiency are both constant. The invariance of shear stress implies uniformity of material strength. In this connection it will be very important whether the rather large depths for earthquakes on ridges proposed by Tsai (1969) can be confirmed by more direct depth determination methods.

If the seismic efficiency is sensitive to the type of fracture associated with an earthquake, the fact that it is constant could suggest that the same process of fracture takes place on ridges and in trenches. Since dehydration of hydrous

minerals is not likely to occur on ridges where material goes from higher to lower temperature, this idea would favor a fracture process associated with melting (Orowan, 1960; Griggs and Baker, 1969; Savage, 1969), rather than one involving dehydration (Raleigh and Paterson, 1965).

Miscellaneous Earthquakes

Originally it was intended to make an apparent stress analyses for the entire circum-Pacific earthquake belt. During the presented work, it turned out that a considerable number of data points is needed in any part of a seismic region in order to determine the stress pattern there. The moments and apparent stresses of earthquakes from regions where a comprehensive apparent stress analysis was not yet possible are given in Table 17. The moments, energies, and apparent stresses were obtained in the way described in the beginning of this chapter. The type of wave, its period, and spectral density on which the moment determination was based, is also given in Table 17. The code for the earthquake mechanism references is 1 = Schaffner (1959), 2 = Schaffner (1961), 3 = Ben-Menahem and Toksoz (1963), 4 = Stauder and Bollinger (1964), 5 = Stauder and Bollinger (1966), 6 = Wu (1966), 7 = Wickens and Hodgson (1967), 8 = Berckhemer and Jacob (1968), 9 = Brune and Engen (1969). This last reference furnished not fault plane

Table 17

Moments and Stresses of Miscellaneous Earthquakes

No.	Station	Date	Hour	Latitude	Longitude	Depth Km	m_b	Moment dyne cm 10^{26}	$\bar{\sigma}$ 10^{-5}	$\bar{\sigma}$ bars	Source Mechanism Reference	Quality	Amplitude cm-sec	Period sec	Phase
1		01 09 62	19	35.6	50.0	11	7.0	18.	2.	7.	7	B	1.66	100	G_1
2		15 08 50	14	28 ½	96 ½	0	8.0	274.	36.	108.	9 & 1	B			
3	COL	26 06 41	11	12 ½	92 ½	60	8.0	94.			9 & 2				
3	SLC	26 06 41	11	12 ½	92 ½	60	8.0	38.	164.	1050.	9 & 2	A			
4	BOZ	01 02 38	19	-5½	130 ½	0	7.9	60.			9 & 2				
4	COL	01 02 38	19	-5½	130 ½	0	7.9	423.	24.	72.	9 & 2	A			
4	SJP	01 02 38	19	-5½	130 ½	0	7.9	238.			9 & 2				
5		21 03 64	03	-6.4	127.9	370	6.85	1.	18.	157.	6	A	2.4	200	R_1
6		07 03 62		19.3	145.3	680	6.8	(1.3)	10.	147.	7	C	0.17	20	P
7		15 08 59	08	22.0	121.0	33	6.5	11.	0.23	1.	7	B	46.	100	G_1
8		26 04 59	20	24.0	122.5	150	7.6	4.4	15.	105	7	A	26.4	100	R_1
8		26 04 59	20	25.0	122.5	150	7.6	5.3			7		1.5	20	P
9		07 12 62	14	29.2	139.2	440	6.9	1.9	12.	120.	7	A	2.2	80	R_1
9		07 12 62	14	29.2	139.2	440	6.9	0.94			7		0.3	20	P
10		22 01 59	05	37.6	142.1	33	6.4	2.0	0.7	2.	7	A	2.4	100	R_2
10		22 01 59	05	37.6	142.1	33	6.4	2.0			7		0.41	20	P
11	SJP	04 03 52	01	42½	144	35-55	7.9	244.			9 & 1		-	-	-
11	CHI	04 03 52	01	42½	144	35-55	7.9	566.	20.	60.	9 & 1	B	-	-	-
11	SLC	04 03 52	01	42½	144	35-55	7.9	(1640.)			9 & 1		-	-	-
12		15 11 63	21	44.3	149.0	33	6.35	2.0	0.6	1.	5	A	13.8	100	G_1
12		15 11 63	21	44.3	149.0	33	6.35	(1.3)			5		(0.16)	20	P
13		30 03 63	16	44.2	148.0	33	6.7	0.18	42.	126.	5	A	0.8	50	R_1
14		20 10 63	00	44.7	150.7	20	6.8	50.	0.3	1.	9 & 5	A	-	-	-
15		16 03 63	08	46.5	154.7	0	7.5	8.7	75.	225.	5	B	48.	100	G_2
16		28 06 63	21	46.5	153.2	33	6.6	3.3	1.3	4.	5	A	17.8	100	R_1
16		28 06 63	21	46.5	153.2	33	6.6	(6.8)			5		0.23	20	P
17		22 05 63	13	48.6	154.7	22	7.2	2.5	48.	138.	5	A	7.4	70	G_1
17		22 05 63	13	48.6	154.7	22	7.2	0.54			5		0.22	20	P
18		18 03 64	04	52.5	153.6	425	6.3	0.13	6.	56.	8	A	-	-	-
19	SLC	04 11 52	16	52.6	160.3	0	7.8	415.			9 & 3		-	-	-
19	CHI	04 11 52	16	52.6	160.3	0	7.8	298.			9 & 3		-	-	-
19	BOZ	04 11 52	16	52.6	160.3	0	7.8	560.	9.	26.	9 & 3	A	-	-	-
19	SJP	04 11 52	16	52.6	160.3	0	7.8	230.			9 & 3		-	-	-
20		25 07 60	11	53.8	158.8	100	7.4	16.	23.	154.	7	B	67.	100	R_1
20		25 07 60	11	53.8	158.8	100	7.4	2.6			7		0.8	20	P
21	BOZ	01 04 46	12	52 3/4	-163½	0	7.2	142.			9 & 1		-	-	-
21	SLC	01 04 46	12	52 3/4	-163½	0	7.2	46.4			9 & 1		-	-	-
21	COL	01 04 46	12	52 3/4	-163½	0	7.2	48.0	1.4	4.	9 & 1	A	-	-	-
21	UKI	01 04 46	12	52 3/4	-163½	0	7.2	40.0			9 & 1		-	-	-
21	WES	01 04 46	12	52 3/4	-163½	0	7.2	137.0			9 & 1		-	-	-
21	TUC	01 04 46	12	52 3/4	-163½	0	7.2	105.			9 & 1		-	-	-
22		20 01 61	17	56.6	-152.3	0	6.4	0.13	11.	33.	7	B	0.86	100	R_1
23		25 07 62	04	18.9	-81.1	0	6.2	0.9	0.53	2.	4	A	6.8	100	R_1
23		25 07 62	04	18.9	-81.1	0	6.2	0.2			4		0.16	20	P
24		24 05 59	19	17.5	-97.2	63	7.0	(3.5)	20.	130.	7	B	(14.3)	70	G_1
24		24 05 59	19	17.5	-97.2	63	7.0	1.4			7		(0.4 NS)	20	P
25		08 01 59	01	15.5	-61.	100	6.7	0.055	145.	970.	7	B	1.3	100	G_1
26		18 07 34	01	8.2	-82.6	0	7.4	21.	17.	51.	9 & 1	B	-	-	
27		26 06 63	17	7.1	-82.3	20.	6.5	0.35	7.	21.	5	A	6.6	100	R_1
27		26 06 63	17	7.1	-82.3	20.	6.5	0.42			5		0.12	20	P
28		30 07 62	20	5.0	-76.3	59	6.7	5.4	1.4	9.	4	B	2.5	100	G_2
29		07 03 63	05	-17.0	-113.5	0	6.85	0.41	42.	126.	9 & 5	A	-	-	-
30		04 07 63	10	-26.3	-177.7	158	6.8	0.73	18.	127.	6	A	5.2	100	R_1
30		04 07 63	10	-26.3	-177.7	158	6.8	0.57			6		0.34	20	P
31		08 03 60	16	-16.5	168.5	230	7.35	3.5	77.	590.	6	A	17.5	80	G_1
31		08 03 60	16	-16.5	168.5	230	7.35	1.3			6		0.57	20	P
32		18 06 62	23	-4.8	151.8	100	7.05	0.26	190.	1270.	7	B	0.66	100	R_1

solutions but amplitude spectral densities. The second column in Table 17 gives the code name of the station where the amplitude was measured. If this column is blank the station was Pasadena.

CONCLUSIONS

An attempt was made to determine the total stress in the source region of earthquakes in the South American seismic zone. It is impossible to obtain rigorously the total shear stress causing earthquakes because the seismic efficiency cannot be known without additional measurements in the source region. What can be determined is the apparent stress, the product of average stress with seismic efficiency. A comparison of the maximal seismic efficiency at different depths allows the conclusion that the varations with depth of apparent stress closely reflect the variations of the total stress. It was demonstrated that there exist variations of more than an order of magnitude between the ratios of short-period to long-period waves radiated by earthquakes of different depth. From this ratio the apparent average stress in the source region was obtained. The apparent average stresses reach a maximum around 100 km depth. The mean value for a magnitude 7.0 earthquake at this depth is 380 bars, an order of magnitude larger than the values at shallow and 600 km depth.

Under the assumption of a rupture velocity at the source the stress drop associated with deep earthquakes can be obtained. The stress drops at intermediate depth are approximately an order of magnitude higher than the ones at shallow and great depth.

From a comparison of stress drop with apparent stress, an upper bound can be put on the seismic efficiency. The seismic efficiency defined at teleseismic distances is in the order of 10% and does not vary significantly with depth.

On these grounds the total shear stresses associated with earthquakes are estimated to be at least 200 bars between the surface and 40 km, 3 kbars around 100 km depth and 440 bars at 600 km depth. Changes of the average stress reflect changes of the strength of the earthquake zone as a function of depth. The strength increases with increasing depth and reaches a maximum at about 100 km. At greater depth the strength decreases again until at 600 km it reaches about the same values as at the surface. This pattern is believed to be an expression of the temperature-pressure conditions in a slab of lithosphere which is plunging into the mantle. With increasing pressure the strength increases, until the slab is heated up enough to be progressively weakened by increasing temperature. At depths below about 650 km the South American slab becomes so weak that no earthquakes can occur. The apparent average stresses are a good test for the nature of the bottom cutoff of an island arc. If the deepest earthquakes in a given island arc indicate high stresses the island arc is not in thermal steady state, i.e., it is young. If the deepest earthquakes indicate stresses comparable

to the ones at zero depth, the island arc is in thermal steady state.

The concave bend in the South American trench around latitude 17°S is associated with a discontinuity of deep seismic activity and with low stresses at 100 km depth. The South American trench should perhaps be viewed as two trenches, the Chilean and the Peruvian, meeting at 17°S.

The high stresses and strains between 45 and 120 km depth indicate high energy density in the source region. In order to produce an earthquake of a given size a comparatively small volume is needed. At these depths the fault dimensions of a magnitude 7.0 event are estimated to range from 1 to 10 km.

The shallow earthquakes of the South American and the Aleutian trench are compared with earthquakes located on ridges. The average of the apparent stress in all regions is close to 20 bars. This may suggest that rupture in trenches and on ridges occurs by the same mechanism.

REFERENCES

Aki, K., Generation and propagation of G waves from the Niigata earthquake of June 16, 1964. Part 2. Estimation of earthquake moment, released energy, and stress-strain drop from G wave spectrum, Bull. Earthquake Res. Inst., Tokyo Univ., 44, 73-88, 1966.

Aki, K., Scaling law of seismic spectrums, J. Geophys. Res., 72, 1217-1231, 1967.

Aki, K., Seismic displacements near a fault, J. Geophys. Res., 73, 5359-5377, 1968.

Albee, A. L., and T. L. Smith, Earthquake characteristics and fault activity in Southern California, in Engineering Geology in Southern California, Editors R. Land and R. Proctor, Assoc. Eng. Geologist, L. A. Section, Spec. Publ., 1966.

Algermissen, S. T., Seismic studies in Alaska, ESSA Symposium on Earthquake Prediction, U. S. Department of Commerce, 1966.

Allen, C. R., The tectonic environments of seismically active and inactive areas along the San Andreas fault system: Stanford Univ. Pub. Geol. Sci., v. 11, p. 70-82, 1968.

Allen, C. R., P. St. Amand, C. F. Richter, and J. M. Nordquist, Relationship between seismicity and geologic structure in the southern California region, Bull. Seism. Soc. Am., 55, 753-797, 1965.

Allen, C. R., and S. W. Smith, Parkfield earthquakes of June 27-29, Monterey and San Luis Obispo counties, California. Pre-earthquake and post-earthquake surficial displacements, Bull. Seism. Soc. Am., 56, 966-967, 1966.

Allen, C. R., A. Grantz, J. N. Brune, M. M. Clark, R. V. Sharp, T. G. Theodore, E. W. Wolfe, and M. Wyss, The Borrego Mountain, California earthquake of 9 April 1968: A Preliminary report, Bull. Seism. Soc. Am., 58, 1183-1186, 1968.

Allen, C. R., M. Wyss, J. N. Brune, A. Grantz, and R. Wallace, Displacement on the Imperial, Superstition Hills, and San Andreas faults caused by the Borrego Mountain earthquake of 9 April 1968, U. S. Geol. Survey Prof. Paper, in preparation, 1970.

Anderson, Don L., Ari Ben-Menahem, and Charles B. Archambeau, Attenuation of seismic energy in the upper mantle, J. Geophys. Res., 70, 1441-1448, 1965.

Anderson, D. L., and David G. Harkrider, Universal dispersion tables, II. Variational parameters for amplitudes, phase velocity and group velocity for first four Love modes for an oceanic and a continental earth model, Bull. Seism. Soc. Am., 58, 1407-1499, 1968.

Anderson, Don L., and C. G. Sammis, Partial melting in the upper mantle, Phys. Earth Planet. Int., in press, 1969.

Archambeau, Charles B., Elastodynamic Source Theory, Ph.D. thesis, California Institute of Technology, Pasadena, California, 1964.

Banghar, A., and L. R. Sykes, Focal mechanism of earthquakes in the Indian Ocean and adjacent areas, J. Geophys. Res., 74, 632-649, 1969.

Barazangi, G., and T. Dorman, World seismicity maps compiled from ESSA, Coast and Geodetic Survey, epicenter data 1961-1967, Bull. Seism. Soc. Am., 59, 369-380, 1969.

Bath, M., Seismological Bulletin Uppsala, February 4, 1965.

Bath, M., and H. Benioff, The aftershock sequence of the Kamchatka earthquake of November 4, 1952, Bull., Seism. Soc. Am., 48, 1-15, 1958.

Bath, M., and S. J. Duda, Earthquake volume, fault plane area, seismic energy strain, deformation, and related quantities, Ann. Geofis. Rome, 17, 353-368, 1964.

Benioff, H., Earthquakes and rock creep. Part I: Creep characteristics of rocks and the origin of aftershocks, Bull. Seism. Soc. Am., 41, 31-62, 1951a.

Benioff, H., Global strain accumulation and release as revealed by great earthquakes, Bull. Geol. Soc. Am., 62, 331-338, 1951b.

Benioff, H., Seismic evidence for crustal structure and tectonic activity, Geol. Soc. Am. Spec. Paper, 62, 61-74, 1955a.

Benioff, H., Mechanism and strain characteristics of the White Wolf fault as indicated by the aftershock sequence, California Div. Mines Bull., 212, 199-202, 1955b.

Benioff, H., F. Press, S. Smith, Excitation of the free oscillations of the earth by earthquakes, J. Geophys. Res., 66, 605-619, 1961.

Ben-Menahem, A., Radiation of seismic surface waves from finite moving source, Bull. Seism. Soc. Am., 51, 401-435, 1961.

Ben-Menahem, A., and M. N. Toksoz, Source mechanism from spectra of long period surface waves, J. Geophys. Res., 67, 1943-1955, 1962.

Ben-Menahem, A., and M. N. Toksoz, Source mechanism from spectra of long period seismic surface waves, 3. the Alaskan earthquake of July 10, 1958, Bull. Seism. Soc. Am., 53, 905-919, 1963.

Ben-Menahem, A., and David G. Harkrider, Radiation patterns of seismic surface waves from buried dipolar point sources in a flat stratified earth, J. Geophys. Res., 69, 2605-2620, 1964.

Ben-Menahem, Ari, Observed attenuation and Q-values of seismic surface waves in the upper mantle, J. Geophys. Res., 70,

4641-4651, 1965.

Ben-Menahem, Ari, S. W. Smith, and Ta-Liang Teng, A procedure for source studies from spectrums of long-period seismic body waves, Bull. Seism. Soc. Am., 55, 203-235, 1965.

Ben-Menahem, Ari, H. Jarosch, and M. Roseninan, Large scale processing of seismic data in search of regional and global stress patterns, Bull. Seism. Soc. Am., 58, 1899-1932, 1968.

Berckhemer, H., and K. H. Jacob, Investigation of the dynamical process in earthquake foci by analyzing the pulse shape of body waves, Final Scientific Report, AF61(052)-801, 1968.

Biehler, S., R. L. Kovach, and C. R. Allen, Geophysical framework of northern end of Gulf of California structural province, Am. Assoc. Petroleum Geologists Mem. 3, p. 126-143, 1964.

Bolt, B. A., C. Lomnitz, and T. V. McEvilly, Seismological Evidence of the tectonics of Central and Northern California and the Mendocino escarpment, Bull. Seism. Soc. Am., 58, 1725-1767, 1968.

Brace, W. F., and T. D. Byerlee, Stick-slip as a mechanism for afterquakes, Science, 153, 990-992, 1966.

Bridgman, P. W., Shearing phenomena at high pressures, particularly in inorganic compounds, Proc. Am. Acad. Arts Sci., 71, 387-460, 1937.

Brown, Robert D., and J. D. Vedder, Surface tectonic fractures along

the San Andreas fault, The Parkfield Cholame, California Earthquakes of June-August 1966, U.S. Geol. Surv. Profess. Paper, 579, 2-22, 1967.

Brune, J. N., A. Espinosa, and J. Oliver, Relative excitation of surface waves by earthquakes and underground explosions in the California-Nevada region, J. Geophys. Res., 68, 3501-3513, 1963.

Brune, J. N., and C. R. Allen, A low-stress-drop, low-magnitude earthquake with surface faulting: The Imperial, California, earthquake of March 4, 1966, Bull. Seism. Soc. Am., 57, 501-514, 1967a.

Brune, J. N., and C. R. Allen, A micro-earthquake survey of the San Andreas fault system in southern California, Bull. Seism. Soc. Am., 57, 277-296, 1967b.

Brune, J. N., Chi-Yu King, Excitation of mantle Rayleigh waves of period 100 seconds as a function of magnitude, Bull. Seism. Soc. Am., 57, 1355-1366, 1967.

Brune, J. N., Seismic moment, seismicity and rate of slip along major fault zones, J. Geophys. Res., 73, 777-784, 1968.

Brune, J. N., T. L. Henyey, and R. F. Roy, Heat flow, stress, and rate of slip along the San Andreas fault, J. Geophys. Res. 74, 3821-3827, 1969.

Brune, J.N., and G. R. Engen, Excitation of mantle Love waves and definition of mantle wave magnitude, Bull. Seism. Soc. Am., 59, 923-933, 1969.

Brune, J. N., Tectonic stress and the spectra of seismic shear waves from earthquakes, in press, 1970.

Bullard, E. C., A. E. Maxwell, and R. Revelle, Heat flow through the deep sea floor, Advan. Geophys., 3, 153-181, 1956.

Bullard, E. C., The flow of heat through the floor of the ocean, in The Sea, Vol. 3, ed. by M. N. Hill, Interscience, New York, 1963.

Bullen, K. E., An Introduction to the Theory of Seismology, Cambridge University Press, England, 1963.

Burridge, R., and L. Knopoff, Body force equivalents for seismic dislocations, Bull. Seism. Soc. Am., 54, 1874-1888, 1964.

Burridge, R., and L. Knopoff, Model of theoretical seismicity, Bull. Seism. Soc. Am., 57, 341-372, 1967.

Burridge, R., The numerical solutions of certain integral equations with non-integrable kernels arising in the theory of crack propagation and elastic wave diffraction, Philosophical Trans. Roy. Soc. of London, Math. and Phys. Sci., 265, 353-381, 1969.

Buwalda, J. P., and P. St. Amand, Geologic effects of the Arvin-Tehachapi earthquake, California Div. Mines. Bull, 171, p. 41-56, 1955.

Byerlee, J. D., Frictional characteristics of granite under high confining pressure, J. Geophys. Res., 72, 3639-3648, 1967a.

Byerlee, J. D., Theory of friction based on brittle fracture, J. Appl. Phys., 38, 2928-2934, 1967b.

Byerlee, J. D., and W. F. Brace, Stick-slip, stable sliding, and earthquakes, J. Geophys. Res., 73, 6031-6039, 1968.

Chinnery, M. A., The deformation of the ground around surface faults, Bull. Seismol. Soc. Am., 51, 355-372, 1961.

Chinnery, M. A., The strength of the earth's crust under horizontal shear stress, J. Geophys. Res., 69, 2085-2089, 1964.

Chinnery, M. A., Earthquake magnitude and source parameters, Bull. Seism. Soc. Am., 59, 1969-1982, 1969.

Clark, M. N., A. Grantz, and C. R. Allen, Displacements on the Coyote Creek fault that accompanied and followed the Borrego Mountain earthquake, U. S. Geol. Survey Prof. Paper, in preparation, 1970.

Cluff, L. S., and K. V. Steinbrugge, Creep in the Irvington district, Fremont, California, in tectonic creep in the Hayward fault zone, California, U. S. Geol. Survey Circ. 525, 8-12, 1966.

Davies, D., and D. P. McKenzie, Seismic travel-time residuals and plates, Geophys. J. Roy. Astr. Soc., 18, 51-63, 1969.

Dickenson, William R., Structural relationship of San Andreas fault system, Cholame Valley, and Castel Mountain range, California, Bull. Geol. Soc. Am., 77, 707-721, 1966.

Dibblee, T. W., Jr., Geology of the Imperial Valley region, California, Calif. Div. Mines Bull. 170, ch. 2, p. 21-28, 1954.

Dietz, R. S., Continent and ocean basin evolution by spreading of the sea floor, Nature, 120, 854-857, 1961.

Eaton, Jerry P., Spacial distributions of aftershocks of the June 27, 1966, Parkfield-Cholame earthquake in the San Andreas fault zone (abstract), Proc. Conf. on Geologic Problems of San Andreas Fault System, Stanford Univ. Publ. Geol. Sci., 11, 84, 1968.

Eaton, J. P., M. E. O'Neill, and J. N. Murdoch, Aftershocks of the 1966 Parkfield-Cholame, California, Earthquake: A detailed Study, in press, 1970.

Evison, F. F., Earthquakes and faults, Bull. Seism. Soc. Am, 53, 873-891, 1963.

Furumoto, A. S., Source mechanism study of the Alaskan earthquake and Tsunami of 27 March 1964, Part II: Analyses of Rayleigh wave, Report HIG-65-17 of the Hawaiian Inst. of Geophys., 1965.

Griggs, D. T., and D. W. Baker, The origins of deep-focus earthquakes, in Properties of Matter, p. 11, John Wiley, New York, 1969.

Gutenberg, B., Energy ratio of reflected and refracted seismic waves, Bull. Seism. Soc. Am., 34, 85-101, 1944.

Gutenberg, B., and C. F. Richter, Materials for the study of deep focus earthquakes, Bull. Seism. Soc. Am., 26, 341-390, 1936.

Gutenberg, B., and C. F. Richter, Magnitude and energy of earthquakes, Ann. Geofis., 9, 1-15, 1956.

Hamilton, R. M., Aftershocks of the Borrego Mountain, California, earthquake from April 12 to June 12, 1968, U. S. Geol. Survey Professional Paper, in preparation, 1970.

Harkrider, D. G., Surface waves in multilayered elastic media, 1. Rayleigh and Love waves from buried sources in a multilayered elastic half-space, Bull. Seism. Soc. Am., 54, 627-679, 1964.

Haskell, N. A., Radiation pattern of Rayleigh waves from a fault of arbitrary dip and direction of motion in a homogeneous medium, Bull. Seism. Soc. Am., 53, 619-642, 1963.

Haskell, N. A., Total energy and energy spectral density of elastic wave radiation from propagating faults, Bull. Seism. Soc. Am., 54, 1811-1841, 1964.

Hess, H. H., Petrological Studies: A volume in Honor of A. F. Buddington, A. E. J. Engel et al (Geol. Soc. Amer., 1962).

Hofmann, Renner B., Earthquake engineering programs progress report, Calif. Dept. of Water Resources Bull. 116-4, 1967.

Hofmann, Renner B., Geodometer fault movement investigations in Calif., Calif. Dept. of Water Resources Bull. 116-6, 1968.

Iida, Kumizi, Earthquake energy and earthquake fault, J. Earth Sci., Nagoya University, 7, 98-107, 1959.

Iida, K., Earthquake magnitude, earthquake fault and source dimensions, J. Earthquake Sci., Nagoya Univ., 13, 115-132, 1965.

Isacks, B., J. Oliver, and L. R. Sykes, Seismology and the new global tectonics, J. Geophys. Res., 73, 5855-5899, 1968.

Isacks, B., and Peter Molnar, Mantle earthquake mechanisms and the sinking of the lithosphere, Nature, 223, 121-1124, 1969.

Julian, B. R., and D. L. Anderson, Travel times, apparent velocities and amplitudes of body waves, Bull. Seism. Soc. Am., 58, 339-366, 1968.

Kanamori, Hiroo, Synthesis of long-period surface waves and its application to earthquake source studies-Kurile Island earthquake of October 13, 1963, in preparation, 1970a.

Kanamori, Hiroo, The Alaska earthquake of 1964 - Radiation of long period surface waves and source mechanism, in preparation, 1970b.

Kasahara, K., The nature of seismic origins as inferred from seismological and geodetic observations, Bull. Earthq. Res.

Inst., 35, 473-532, 1957.

Kasahara, K., and A. E. Stevens ed., A symposium on processes in the focal region, Publications of the Dominion Observatory, Ottawa, Canada, 1969.

Keilis-Borok, V. I., On estimation of the displacement in an earthquake source and of source dimensions, Annali Geofisica, 12, 205-214, 1959.

Khattri, K. N., Focal mechanism of the Brazil deep focus earthquake of November 3, 1965, from the amplitude spectra of isolated P-waves, Bull. Seism. Soc. Am., 59, 691-704, 1969.

King, Chi-Yu, Seismic efficiency, J. Geophys. Res., 74, 1702-1703, 1969.

King, Chi-Yu, and L. Knopoff, Stress drop in earthquakes, Bull. Seism. Soc. Am., 58, 1, 249-258, 1968a.

King, Chi-Yu, and L. Knopoff, Model Seismicity: Rupture parameters, stress and energy relations, J. Geophys. Res., 73, 4, 1399-1406, 1968b.

Knopoff, L., Energy release in earthquakes, Geophys. J., 1, 44-52, 1958.

Kovach, R. L., C. R. Allen, and F. Press, Geophysical Investigations in the Colorado delta region, J. Geophys. Res.,67, 2845-2871, 1962.

Le Pichon, X., Sea-floor spreading and continental drift, J. Geophys. Res., 73, 3661-3697, 1968.

Liebermann, Robert C., and Paul W. Pomeroy, Source dimensions of small earthquakes as determined from the size of the aftershock zone, Bull. Seism. Soc. Am., in preparation, 1969.

Maruyama, T., On the force equivalent of dynamic elastic dislocations with reference to the earthquake mechanism, Bull. Earthquake Res. Inst., Tokyo Univ., 41, 467-486, 1963.

Mansinha, L., The velocity of shear fracture, Bull. Seism. Soc. Am., 54, 1, 369-376, 1964.

McEvilly, T. V., W. M. Bakun, K. B. Cassaday, The Parkfield California earthquakes of 1966, Bull. Seism. Soc. Am., 57, 1221-1258, 1967.

Mckenzie, Dan P., and R. L. Parker, The north Pacific: An example of tectonics on a sphere, Nature, 216, 1276, 1967.

McKenzie, D. P., and J. G. Slater, Heat flow inside the Island Arcs of the Northwestern Pacific, J. Geophys. Res., 73, 3173-3179, 1968.

McKenzie, Dan P., Speculations on the consequences and causes of plate motions, Geophys. J., 18, 1-32, 1969.

Meade, B. K., Report on results of triangulation for earth movement study, vicinity of Cholame, Calif., Mem. ESSA, Coast and Geodetic Surv., 3 pp., Washington Science Center, Rockville, Md., 1966.

Miyamura, S., S. Omote, R. Teisseyre, and E. Vesanen, Multiple shocks and earthquake series pattern, Bulletin of the International Institute of Seismology and Earthquake Engineering, 2, 71-92, 1964.

Molnar, Peter and Jack Oliver, Lateral variations of attenuation in the upper mantle and discontinuities in the lithosphere, J. Geophys. Res., 74, 2648-2682, 1969.

Morgan, W. J., Rises, trenches, great faults, and crustal blocks, J. Geophys. Res., 73, 1959-1982, 1968.

Neuber, H., Kerbspannungslehre, Berlin, Springer-Verlag, 161 p., 1937.

Niazi, Mansour, Seismicity of northern California and western Nevada, Bull. Seism. Soc. Am., 54, 845-850, 1964.

Oliver, Jack, and Bryan Isacks, Deep earthquake zones, anomalous structures in the upper mantle, and the lithosphere, J. Geophys. Res., 72, 4259-4275, 1967.

Orowan, E., Mechanism of seismic faulting, in rock deformation, A Symposium, Geol. Soc. Am., Memoir 79, 1960.

Plafker, G., Tectonic deformation associated with the 1964 Alaskan earthquake, Science, 148, 3678, 1675-1687, 1965.

Press, F., A. Ben-Menahem, N. Toksoz, Experimental determination of earthquake fault length and rupture velocity, J. Geophys. Res., 66, 10, 3471-3485, 1961.

Press, F., Seismic wave attenuation in the crust, J. Geophys. Res., 69, 4417-4418, 1964.

Press, F., D. Jackson, Alaskan earthquake, 27 March 1964: Vertical extent of faulting and elastic strain energy release, Science, 147, 867-868, 1965.

Press, F., Displacements, strains and tilts at teleseismic distances, J. Geophys. Res., 70, 2395-2412, 1965.

Press, Frank, Dimensions of the source region for small shallow earthquakes, Proc. of the VESIAC Conf. on the Current Status and Future Progress for Understanding the Source Mechanism of Shallow Seismic Events in the 3 to 5 magnitude range, 1967.

Radbruch, D. H., and B. J. Lennert, Damage to culvert under Memorial Stadium, University of California, Berkeley, in Tectonic Creep in the Hayward Fault zone, California, U. S. Geol. Survey Circ. 525, 3-6, 1966.

Raleigh, C. B., and M. S. Paterson, Experimental deformation of serpentinite and its tectonic implications, J. Geophys. Res., 70, 3965, 3985, 1965.

Randall, John M., The Radiation pattern of the long-period P-wave pulse: A measure of strain at the focus of deep earthquakes, Ph.D. Thesis, University of California, Los Angeles, 1968.

Reid, H. F., The mechanics of the earthquake, volume II of the report of the state earthquake investigation commission on the California earthquake of 1906, Carnegie Institute, Washington, 1910.

Richter, C. F., Elementary Seismology, W. H. Freeman and Co., San Francisco, 1958.

Richter, C. F., J. N. Nordquist, V. Taylor, and C. R. Allen, Local Bulletin of earthquakes in the southern California region, 1967.

Savage, J. C., The stopping phase on seismograms, Bull. Seism. Soc. Am., 55, 1, 47-58, 1965.

Savage, J. C., and L. M. Hastie, Surface deformation associated with dip-slip faulting, J. Geophys. Res., 71, 4897-4904, 1966.

Savage, J. C., A possible explanation of the orientation of fault planes for deep-focus earthquakes (abstract) Annual meeting of the Seismological Society of America, 1969.

Schaffner, H. J., Die Grundlagen und Answerteverfahren zur seismischen Bestimmung von Erdbeben mechanismen, Freiberger Forsch.,63, 1959.

Schaffner, H. J., Tabellen kinematischer Erdbeben hard parameter, Publ. Inst. Angew. Geophys., Freiberg, 1961.

Scholz, C. H., Microfracturing and the inelastic deformation of rock, J. Geophys. Res., 73, 1417-1432, 1968a.

Scholz, C. H., Microfractures, aftershocks, and seismicity, Bull. Seism. Soc. Am., 58, 1117-1130, 1968b.

Scholz, C. H., Mechanism of creep in brittle rock, J. Geophys. Res., 73, 3295-3302, 1968c.

Scholz, C. H., M. Wyss, and S. W. Smith, Seismic and aseismic slip on the San Andreas fault, J. Geophys. Res., 74, 2049-2069, 1969.

Smith, S. W., C. G. Sammis, and W. H. Jackson, Microearthquake source dimensions and energy release, Trans. Am. Geophys. Union, 48, 201, 1967.

Smith, S. W., and Max Wyss, Displacement on the San Andreas fault initiated by the 1966 Parkfield earthquake, Bull. Seism. Soc. Am., 1955-1973, 1968.

Starr, A. T., Slip in a crystal and rupture in a solid due to shear, Proc. Cambridge Phil. Soc., 24, 489-500, 1928.

Stewart, S. W., Preliminary comparison of seismic travel times and inferred crustal structure adjacent to the San Andreas fault in the Diablo and Gabilan ranges of Central California, Proc. Conf. on Geologic Problems of San Andreas Fault System, Stanford Univ. Publ. Geol. Sci., 11, 218-231, 1968.

Stauder, W., and G. A. Bollinger, The S-wave project for focal mechanism studies: Earthquakes of 1962, Bull. Seism. Soc. Am., 54, 2199-2208, 1964.

Stauder, W., and G. A. Bollinger, The S-wave project for focal mechanism studies, earthquakes of 1963, Bull. Seism. Soc. Am., 56, 6, 1363-1371, 1966.

Stauder, W., and G. A. Bollinger, The focal mechanism of the Alaskan earthquake of March 28, 1964 and its aftershock sequence, J. Geophys. Res., 71, 22, 5283-5296, 1966.

Stauder, William, Tensional character of earthquake foci beneath the Aleutian Trench with relation to sea-floor spreading, J. Geophys. Res., 73, 7693-7701, 1968.

Stauder, W., Focal mechanisms for South American earthquakes, in preparation, 1970.

Sykes, L. R., Mechanism of earthquakes and nature of faulting on the mid-oceanic ridges, J. Geophys. Res., 72, 2131-2153, 1967.

Sykes, L. R., Seismological evidence for transform faulting, sea-floor spreading, and continental drift, in History of the Earth's Crust, R. A. Phinney, ed., Princeton University Press 1968.

Tobin, Don G. and L. R. Sykes, Seismicity and tectonics of the northeast Pacific Ocean, J. Geophys. Res., 73, 3821-3845, 1968.

Tocher, D., Earthquake energy and ground breakage, Bull. Seism. Soc. Am., 48, 147-153, 1958.

Tocher, D., Creep rate and related measurements at Vineyard, California, Bull. Seism. Soc. Am., 50, 396-404, 1960.

Trifunac, M. D., and J. N. Brune, Complexity of energy release during the Imperial Valley, California, earthquake of 1940, Bull. Seism. Soc. Am., 60, 137-160, 1970.

Tsai, Yi-Ben, Determination of focal depths of earthquakes in the Mid-oceanic ridges from amplitude spectra of surface waves, Ph.D. thesis, Massachusetts Institute of Technology, 1969.

Tsuboi, C., Earthquake energy, earthquake volume, aftershock area and strength of the earth's crust, J. Phys. Earth, 4, 63-66, 1957.

Ulomov, V. I., and B. Z. Mavashev, Forerunner of a strong tectonic earthquake (abstract), Dokl. Akad. Nauk Moscow USSR, 176, 319-321, 1967.

Usami, T., Seismometrical study of Boso-Oki earthquake of November 26, 1953, Quart. Jour. Seismology, 21, 3, 1-13, 1956.

Vesanen, Ei Jo, Ueber die Typenanalytische Auswertung der Seismogramme, Ann. Acad. Sci. Fenn., A III, 5, 1942.

Vasil'yev, Yu. F., Model of a seismic fault, Iz. Acad. Sci. USSR, Earth Phys., no. 3, 11, (AGU English transl., no. 3, 148), 1968.

Wallace, R. E., and E. F. Roth, Rates and patterns of progressive deformation, The Parkfield-Cholame, California Earthquakes June-August 1966, U. S. Geol. Survey Profess. Paper, 579, 23-40, 1967.

Wallace, R., and R. D. Brown, Offset stream channels along the San Andreas fault in the Southern Coast Ranges, Proceedings of Conference on Geologic Problems of the San Andreas Fault System, Stanford University Publication, California, 1968.

Walsh, J. B., Mechanics of strike-slip faulting with friction, J. Geophys. Res., 73, 761-776, 1968.

Wickens, A. T., and T. H. Hodgson, Computer re-evaluation of earthquake mechanism solutions 1922-1962, Public. Dominion Observatory, Ottawa, V. 33, 1967.

Wu, Francis T., Lower limit of the total energy of earthquakes and partitioning of energy among seismic waves, Ph.D. Thesis, California Institute of Technology, Pasadena, 1966.

Wu, Francis T., Parkfield earthquake of June 27, 1966: Magnitude and source mechanism, Bull. Seism. Soc. Am., 58, 689-711, 1968.

Wyss, Max, and J. N. Brune, The Alaska earthquake of 28 March 1964: A complex multiple rupture, Bull. Seism. Soc. Am., 57, 5, 1017-1025, 1967.

Wyss, Max, and J. N. Brune, Seismic moment, stress, and source dimensions for earthquakes in the California-Nevada Region, J. Geophys. Res., 73, 4681-4694, 1968.